# AUTOGENOUS SELF-HEALING OF ALKALI-ACTIVATED SLAG EXPOSED TO ELEVATED TEMPERATURES

#### **Ahmed Khaled Ahmed**

A Thesis

In the Department

of

Building, Civil and Environmental Engineering

Presented in Partial Fulfillment of the Requirements

For the Degree of

Doctor of Philosophy (Civil Engineering)

Concordia University

Montreal, Quebec, Canada

March 2025

© Ahmed Khaled Ahmed, 2025

# CONCORDIA UNIVERSITY SCHOOL OF GRADUATE STUDIES

	Dr. Mourad Debbabi, Dean of Gina Cody School of Engineer & Computer Science	ing
	Dr. Po-Han Chen, Graduate Program Director	
Approve	l by	
Dr.	Ahmed Soliman	Thesis Supervisor
Dr.	Chunjiang An	Thosis Supomison
	51W0 E1	Examiner
Dr ·	Biao Li	Examiner
Dr.	Mamoun Medraj	LAMIIIIICI
Dr.	Mohamed T. Bassuoni	Examiner
D., .	Mahamad T. Passyoni	External Examine
Dr.	Carol Fung	Chair
Signed by	the final examining committee:	Clair
respect to	originality and quality.	WALLED WILLI
complies	with the regulations of the University and meets the accepted star	ndards with
	DOCTOR OF PHILOSOPHY (Civil Engineering)	
and subm	itted in partial fulfillment of the requirements for the degree of	
Entitled:	Autogenous Self-Healing of Alkali-Activated Slag Exposed to E	levated Temperatures
By:	Ahmed Khaled Ahmed	
11113 13 10	certify that the thesis prepared	

#### **Abstract**

#### Autogenous Self-Healing of Alkali-Activated Slag Exposed to Elevated Temperatures

Ahmed Khaled Ahmed, Ph.D.

#### Concordia University, 2025

The increasing urgency of mitigating climate change has accelerated the shift toward sustainable construction materials with reduced carbon emissions. Alkali-activated materials (AAMs) have emerged as a promising alternative to Portland cement, offering significant CO<sub>2</sub> reduction while maintaining comparable mechanical and durability properties. However, similar to conventional binders, AAMs remain vulnerable to cracking and deterioration under extreme conditions, such as fire exposure. This research aims to develop a low-carbon, high-resilience construction material by enhancing the post-fire autogenous self-healing ability of alkali-activated slag (AAS). The study investigates the self-healing potential of AAS exposed to elevated temperatures (200°C, 400°C, 600°C, and 800°C) under different curing conditions, including water, ambient air, and sodium hydroxide solution. Furthermore, the incorporation of self-healing agents such as crystalline admixtures (CA) will be explored to maximize self-healing efficiency. The experimental program, including compressive strength tests, ultrasonic pulse velocity (UPV), water sorptivity, rapid chloride penetration test (RCPT), scanning electron microscopy (SEM), and X-ray diffraction (XRD) reveals a notable recovery in both mechanical and durability properties after self-healing. By leveraging the inherent reactivity of un-hydrated slag and promoting the crystallization of healing products, this study advances the development of fire-resistant, selfrepairing, and environmentally sustainable construction materials. The findings contribute to a more resilient built environment, ensuring improved structural performance and sustainability.

## **Table of contents**

Chapter 1 : Introduction	1
1.1 General Background and Problem Definition	1
1.2 Research Objectives	2
1.3 Original Contributions	2
1.4 Thesis organization	3
Chapter 2 : Literature review	6
2.1 Introduction	6
2.1.1 Background and general definitions	6
2.1.2 Advantages and disadvantages of AAMs	8
2.1.3 Mechanical properties of AAMs	9
2.2 Elevated temperature exposure	12
2.3 Self-healing of materials	13
2.3.1 Autogenous self-healing	.14
2.3.2 Limitation of autogenous self-healing	.17
2.3.3 Influence of damage-degree on autogenous self-healing	.19
2.3.4 Cracks initiation and propagation	.20
2.3.5 Quantification of autogenous self-healing	.21
2.4 Critical analysis for the factors affecting the extent of self-healing	22
2.4.1 Influence of damage degree on self-healing of concrete	.22
2.4.2 Effect of age and level of damage on the autogenous healing of lime mortars	.22

2.4.3 X-ray computed microtomography of three-dimensional microcracks a	nd self-healing in
engineered cementitious composites	23
2.5 Applications of alkali-activated materials	24
2.5.1 Repair applications	24
2.5.2 Road applications	28
Chapter 3: Methodology and experimental plan	30
3.1 Methodology	30
3.2 Experimental Plan	30
Chapter 4: Effect of activator dosages on autogenous self-healing	35
4.1 Abstract	35
4.2 Introduction	36
4.3 Materials and methods	38
4.3.1 Materials	38
4.3.2 Self-healing study	39
4.3.3 Testing methods	41
4.4 Results and discussion	42
4.4.1 Visual inspection	42
4.4.2 Compressive strength	43
4.4.3 Tensile strength	48
4.4.4 Permeability	53
4.4.5 Absorption and sorptivity	58

4.4.6 Thermogravimetric analysis TGA	61
4.4.7 SEM-EDX	64
4.4.8 XRD	65
4.5 Conclusion	66
Chapter 5: Application of Wet-dry Cycles as post-fire curing so	cheme to Boost Autogenous
Self-healing of Alkali-activated Slag	68
5.1 Abstract	68
5.2 Introduction	68
5.3 Materials and methods	71
5.3.1 Materials	71
5.3.2 Specimens preparation	71
5.3.3 Testing methods	73
5.4 Results and discussion	75
5.4.1 Visual inspection	75
5.4.2 Compressive strength	76
5.4.3 Tensile strength	79
5.4.4 Permeability	80
5.4.5 Absorption and sorptivity	81
5.4.6 XRD	83
5.4.7 Thermogravimetric analysis TGA	84
5.5 Discussion	86

5.6 Conclusion	87
Chapter 6 : Microstructures and Healing Mechanism	89
6.1 Abstract	89
6.2 Introduction	90
6.3 Research Significance	93
6.4 Materials and methods	94
6.4.1 Materials	94
6.4.2 Experimental Design	95
6.4.3 Mixture proportioning	95
6.4.4 Elevated Temperature Exposure	96
6.4.5 Self-healing Study	97
6.4.6 Testing Methods	99
6.5 Results and discussion	101
6.5.1 Visual inspection	.101
6.5.2 Quantification of self-healing using the UPV method	.103
6.5.3 Water Sorptivity	.105
6.5.4 RCPT Analyzes	.110
6.5.5 SEM-EDX	.113
6.5.6 XRD analysis	.114
6.6 Conclusion and Recommendations	116
Chapter 7: Incorporation of Crystalline admixture to boost autogenous self-healing of	fire-

damaged alkali-activated slag	119
7.1 Introduction	120
7.2 Materials and methods	122
7.2.1 Materials	122
7.2.2 Mixture proportioning	123
7.2.3 Elevated Temperature Exposure	124
7.2.4 Self-healing Study	124
7.2.5 Testing Methods	125
7.3 Results and discussion	126
7.3.1 Visual inspection.	126
7.3.2 Compressive strength	128
7.3.3 Tensile strength	129
7.3.4 Water Sorptivity	131
7.3.5 Permeability	133
7.4 Discussion	136
7.5 Conclusion and Recommendations	137
Chapter 8 : Conclusion, Recommendations, and Future Work	139
8.1 Introduction	139
8.2 Summary of Major Findings	139
8.2.1 Effect of Activator Dosage and Post-Fire Water Curing	139
8.2.2 Post-Fire Wet-Dry Curing Scheme	140

8.2.3 Post-Fire Healing Using Alkaline Solution (NaOH)	140
8.2.4 Incorporation of Crystalline Admixture for Post-Fire Healing	140
8.3 Critical Reflections and Contributions	141
8.4 Practical Implications	141
8.5 Limitations of the Study	142
8.6 Recommendations for Future Research	142
8.7 Final Remarks	143
References	143

# **List of Figures**

Fig. 2-1 Geopolymerization of AAM
Fig. 2-2 SiO <sub>2</sub> -Al <sub>2</sub> O <sub>3</sub> -CaO ternary diagram
Fig. 2-3 Heat profile of exposure to elevated temperature
Fig. 2-4 Schematic section for proposed self-healing.
Fig. 2-5 Application of the alkali-activated mortars to a vertical concrete surface. (a) The S mortar
(b) the FA mortar, and (c) the MK mortar
Fig. 2-6 AAMs repair mortars bonded to OPC
Fig. 2-7 Bond strength (AAMs & OPC), measured using Slant Shear Test29
Fig. 3-1 Phases of the dissertation.
Fig. 3-2 Experimental plan
Fig. 4-1 Visual inspection
Fig. 4-2 Compressive strength for damaged specimens at age of 28 days, and post-fire water cured
specimens at age 56 days
Fig. 4-3 Self-healing percentages versus damage and recovery percentages, calculated according
to the AAS compressive strength results
Fig. 4-4 Tensile strength for damaged specimens at age of 28 days, and post-fire water cured
specimens at age 56 days
Fig. 4-5 Self-healing percentages versus damage and recovery percentages, calculated according
to the AAS tensile strength results
Fig. 4-6 Permeability coefficient
Fig. 4-7 Permeability recovery

Fig. 4-8 Sorptivity60
Fig. 4-9 Self-healing versus damage and recovery
Fig. 4-10 Thermogravimetric analysis
Fig. 4-11 SEM analysis65
Fig. 4-12 XRD analysis for (a) reference, (b) after exposure to 600 °C, and (c) after applying water
self-healing66
Fig. 5-1. Crack mapping of the wet-dry self-healed specimens after 600 °C75
Fig. 5-2. Differences in crack closures, (a) water post-fire curing scheme (b) wet-dry post-fire
curing scheme, after deteriorated under 600 °C
Fig. 5-3. Compressive strength of self-healed specimens (air, water, and wet-dry)79
Fig. 5-4. Tensile strength of self-healed specimens (air, water, and wet-dry)
Fig. 5-5. Permeability coefficients of Air, Water, and Wet-dry self-healed specimens
Fig. 5-6. Water absorption (mm <sup>3</sup> /mm <sup>2</sup> ) for Air, Water, and Wet-dry post-fire curing schemes82
Fig. 5-7. Differences in capillary water absorption rates between (a) Water self-healed specimens
(b) Wet-dry self-healed specimens
Fig. 5-8. XRD analysis for the fire-damaged 600 °C specimens, Air, Water, and Wet-dry schemes
84
Fig. 5-9. TGA of the 600 °C fire-damaged specimens; AAS-AC, AAS-WC, and AAS-CC86
Fig. 5-10. Self-healing mechanism under the wet-dry cycles
Fig. 6-1 Flow chart for the experimental program95
Fig. 6-2 Heat profile
Fig. 6-3 Schematic diagram for the self-healing quantification process
Fig. 6-4 Cracks observations for a) NC-AAS sample b) AC-AAS sample after 600 °C102
xi

Fig. 6-5 Cracks observations for a) cracks less than 50 $\mu$ m, b) cracks in range of 50–150 $\mu$ m, c)
cracks more than 150 μm
Fig. 6-6 Comparative analysis between percentage of damage and self-healing percentage at
different exposure temperatures
Fig. 6-7 Capillary absorption after elevated temperatures exposure for (a) AC-AAS specimens (b)
NC-AAS specimens
Fig. 6-8 Water sorptivity (mm/√sec) after elevated temperature exposure for (a) AC-AAS
specimens (b) NC-AAS specimens
Fig. 6-9 Percentage of self-healing versus the remaining percentage to achieve the full recovery.
108
Fig. 6-10 Autogenous self-healing mechanism for AAS
Fig. 6-11 The total charge passed for NC-AAS and AC-AAS specimens at different exposure
temperatures (200 °C-600 °C)
Fig. 6-12 Percentage of damage and self-healing according to RCPT
Fig. 6-13 SEM observation on cracks after self-healing treatment of AAS114
Fig. 6-14 XRD analysis116
Fig. 7-1. Thermal and structural stability of the crystalline admixture
Fig. 7-2. Different crystal formations upon implementation of crystalline admixture
Fig. 7-3. Compressive strength of the control, post-fire water cured (AAS), and specimens with
crystalline admixtures (AAS-CA)
Fig. 7-4. Tensile strength of the control, post-fire water cured (AAS), and specimens with
crystalline admixtures (AAS-CA)
Fig. 7-5. Absorption of (a) control (b) AAS without crystalline admixture (c) AAS with CA 133

admixture	137
Fig. 7-8. Schemetic diagram for self-healing (a) without crystalline admixture (b) u	sing crystalline
Fig. 7-7. Permeability coefficient for control, AAS without CA, and AAS with CA	136
Fig. 7-6. Sorptivity of (a) AAS without crystalline admixture (b) AAS with CA	133

# **List of Tables**

Table 2-1 Correlation between the crack opening and the corresponding local diffusion	19
Table 2-2 Mechanical properties of AAS based on the three different precursors	28
Table 4-1 Chemical properties of GGBFS	38
Table 4-2 Mixtures and curing conditions	40
Table 5-1 Chemical compositions of the used GGBFS	71
Table 5-2 Mix proportioning and the applied post-fire self-healing scheme	72
Table 6-1 Chemical composition of the used GGBFS	94
Table 6-2 Mix proportioning of the studied AAS concrete	96
Table 6-3 Sorptivity coefficient	107
Table 6-4. The chemical composition of the healing material	114
Table 7-1: Chemical composition of the used GGBFS	123
Table 7-2. Mix proportioning and the applied post-fire self-healing scheme	124

#### Nomenclature

AAM Alkali Activated Material

AAS Alkali Activated Slag

AASHTO American Association of State Highway and Transportation Officials

ACI American Concrete Institute

AFm Aluminate-Ferrite-Mono Sulfate

Al Alumina

ASTM American Society for Testing and Materials

Ca Calcium

D Diameter

**E** Strain

Ed Dynamic Modulus Of Elasticity

EDX Energy Dispersive X-Ray

Es Static Modulus Of Elasticity

F Force

FA Fly Ash

g Gravity Acceleration

GU General Use

H Height

Ht Hydrotalcite

Ms Silica Modulus

Na Sodium

°C Celsius Degree

## **Chapter 1: Introduction**

#### 1.1 General Background and Problem Definition

In the era of environmental concerns, more attention is given for adopting sustainable approaches targeting neutral carbon dioxide (CO<sub>2</sub>) emissions by 2050. As cement production is one of the main contributors to global CO<sub>2</sub> emissions, it has become an indispensable necessity to find low-carbon alternative binding systems which can functionally substitute the cement binders. Alkali-activated materials (AAMs) have been successfully introduced as a green and sustainable binders, exhibiting behaviors comparable to conventional cement. These AAMs are susceptible to cracks and deteriorations under the effects of different exposure conditions like conventional ones. Repair, strengthening, and retrofitting are all various means which have been effectively revealed as direct solutions for such damages. However, applicability of these techniques with AAMs is not fully investigated. With the advent of self-healing concept, which reflect the ability of material to heal itself by closing its cracks and restoring its integrity without human intervention, the potential to achieve sustainable smart materials become a fact. Recent research has explored AAMs' ability to autogenously and autonomously self-healed after the damage effects of different mechanical loading mechanisms. However, in fire events, the ability of AAMs to regain its strength and maintain integrity are more critical and represent a knowledge gap. Hence, this research examines AAMs' self-healing ability after being deteriorated due to fire exposure Exploring the associated changes in the material's phases during exposure to fire will provide a fundamental understanding for the AAMs' potential to self-healed.

#### 1.2 Research Objectives

This thesis presents a comprehensive exploration of the autogenous self-healing of alkali activated slag exposed to elevated temperatures. The findings contribute valuable insights into achieving environmentally sustainable construction practices. By overcoming the challenges associated to elevated temperatures exposure, these research outcomes have the potential to revolutionize concrete construction methods, leading to more efficient, eco-friendly, and resilient buildings for a greener future.

This will be achieved through:

- 1- Study the inherent self-healing abilities of alkali-activated slag (AAS) under autogenous conditions, particularly when exposed to elevated temperatures.
- 2- Evaluate how different levels of elevated temperatures impact the self-healing efficiency of AAS, including microstructural changes, mechanical recovery, and durability.
- 3- Identify and characterize the phases or compounds formed during the self-healing process at elevated temperatures, such as any new hydration products or crystalline phases.

#### 1.3 Original Contributions

- 1- Providing the first detailed study of how alkali-activated slag (AAS) can autogenously self-heal when exposed to elevated temperatures, including the specific chemical and physical processes that enable healing in these extreme conditions.
- 2- Discovering and characterizing new hydration or recrystallization products that form during the self-healing process under high temperatures, which may differ from those found in conventional concrete or under normal conditions.

- 3- Establishing a unique understanding of how AAS responds to varying elevated temperatures in terms of its crack-healing capacity, offering insights that could inform the development of thermally resilient materials in construction.
- 4- Demonstrating significant improvements in the durability and mechanical recovery of AAS after exposure to elevated temperatures, potentially outperforming traditional cementitious materials.
- 5- Offering a sustainable alternative to Portland cement in high-temperature environments, due to the environmental benefits of AAS (e.g., lower carbon emissions), while also addressing concerns about performance at elevated temperatures.
- 6- Providing detailed insights into the microstructural changes in AAS during the self-healing process at elevated temperatures, using advanced characterization techniques (e.g., SEM, XRD, or EDX). This contribution could highlight the relationship between microstructure, crack closure, and temperature, adding to the existing body of knowledge on the thermal stability and resilience of alkali-activated materials.

#### 1.4 Thesis organization

This thesis is structured into seven chapters, each addressing a crucial aspect of the research on post-fire autogenous self-healing of alkali-activated slag (AAS).

Chapter 1 introduces the research by providing a general background on the environmental challenges associated with conventional Portland cement and the potential of alkali-activated materials (AAMs) as sustainable alternatives. The chapter outlines the problem definition, research objectives, and the original contributions of this study in the field of self-healing AAMs. Chapter 2 presents a comprehensive literature review on AAMs, including their advantages, disadvantages,

and mechanical properties. The chapter discusses the effect of elevated temperature exposure on AAMs and explores the concept of self-healing, emphasizing autogenous self-healing mechanisms, their limitations, and the influence of damage degree on healing efficiency. Furthermore, critical analyses of past research, including studies on self-healing quantification, X-ray computed microtomography of microcracks, and the effects of age and damage level on self-healing, are discussed. Finally, applications of AAMs in repair and road construction are highlighted. Chapter 3 details the research methodology and experimental plan. It outlines the procedures for investigating the post-fire self-healing capacity of AAS, including specimen preparation, exposure to elevated temperatures, and the evaluation of self-healing through various testing methods. Chapter 4 investigates the effect of activator dosages on the autogenous self-healing behavior of AAS. The chapter presents experimental findings on compressive and tensile strength recovery, permeability reduction, and microstructural evolution through thermogravimetric analysis (TGA), scanning electron microscopy (SEM-EDX), and X-ray diffraction (XRD). The results highlight the role of unhydrated slag particles in promoting self-healing by forming additional hydration products. Chapter 5 examines the application of wet-dry cycles as a post-fire curing scheme to enhance the self-healing efficiency of AAS. This chapter evaluates the effect of alternating wetting and drying conditions on self-healing, particularly in terms of mechanical recovery, crack closure, and improvements in permeability and sorptivity. The findings demonstrate the potential of this curing approach in enhancing the resilience of fire damaged AAS. Chapter 6 focuses on microstructural analysis and the underlying self-healing mechanisms. It investigates the evolution of microstructures after fire exposure and subsequent healing, using advanced techniques such as ultrasonic pulse velocity (UPV), water sorptivity, rapid chloride penetration test (RCPT), SEM-EDX, and XRD analysis. The results provide insight into the transformation of amorphous phases

into crystalline healing products, contributing to the densification of the AAS matrix and improving its durability properties. Chapter 7 explores the incorporation of crystalline admixture as a self-healing agent to enhance the recovery of fire damaged AAS. The effects of crystalline admixture on mechanical performance, permeability, and sorptivity are discussed, along with an analysis of the underlying self-healing mechanisms facilitated by crystalline phase precipitation. The chapter concludes with recommendations for optimizing the use of crystalline admixture in self-healing AAM applications. Finally, the thesis concludes with a comprehensive list of references, documenting the studies that have informed this research.

### **Chapter 2:** Literature review

#### 2.1 Introduction

#### 2.1.1 Background and general definitions

Cement production is one of the major sources of greenhouse gas emissions. Hence, it becomes an indispensable priority to find other effective and friendly alternatives with less carbon dioxide (CO<sub>2</sub>) footprints [1]. Therefore, AAMs or geopolymer materials were introduced as promising innovative materials presenting more advanced sustainability, with lower energy requirements for production than OPC [2–4]. AAMs are cement-free materials which is formed through the geopolymerization of by-product waste materials rich in aluminosilicate, using alkaline activator solutions, to produce aluminosilicate gel. This gel will have binding characteristics. In more details, aluminosilicate raw material is dissolved in the high alkaline solution producing (AlO<sub>4</sub>) and (SiO<sub>4</sub>) tetrahedra, both will be sharing oxygen atom to form monomer. Resultant monomers will interact to form oligomer which subsequently undergo a polycondensation reaction to form 3-D network structure representing the binder gel [5] as illustrated in Fig. 2-1.

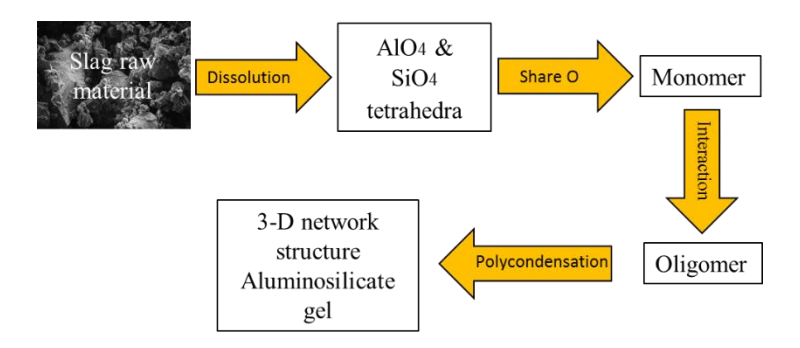


Fig. 2-1 Geopolymerization of AAM

Depending on the chemical components of used raw materials, different types of AAMs with

different chemical reaction mechanisms, formed hydration products, and mechanical properties are produced. AAMs precursors were classified into three categories according to the percentage of calcium concentration content: calcium-free (i.e., FA type F), low calcium content (i.e., Metakaolin (MK)), and calcium-rich (i.e., slag) [6]. As shown in Fig. 2-2, aluminosilicate precursors (e.g., slag, MK, and FA) which can be used in AAMS, were indicated according to silicate oxide (SiO<sub>2</sub>)-aluminium oxide (Al<sub>2</sub>O<sub>3</sub>)- calcium oxide (CaO) ternary composition, while a comparison between those materials with limestone and OPC were also illustrated. Furthermore, alternative alkali activated precursors, rich in aluminosilicate, such as Rice Husk Ash (RHA), red mud, and heated coal gangue have been proposed and incorporated due to the increasing demand for the conventional precursors [7]. Hydration products of Calcium-free and low-calcium precursors are mainly zeolite-like (e.g., analcite (N-A-S-H), sodalite) gels. Hydration products of calcium-rich precursors are mainly calcium aluminum silicate hydrates (C-A-S-H) gels with a low (Ca/Si) ratio [6].

Moreover, chemical compositions of alkaline activator solutions have a substantial effect on the hydration process and subsequently the generation of hydration products. Alkali activators were classified into six categories; caustic alkali (MOH), silicate (M<sub>2</sub>O.nSiO<sub>2</sub>), aluminate (M<sub>2</sub>O.nAl<sub>2</sub>O<sub>3</sub>), aluminosilicate (M<sub>2</sub>O.Al<sub>2</sub>O<sub>3</sub>.2–6SiO<sub>2</sub>), non-silicate weak acid salt (M<sub>2</sub>CO<sub>3</sub>, M<sub>2</sub>SO<sub>3</sub>), non-silicate strong acid salt (M<sub>2</sub>SO<sub>4</sub>) [8,9]. However, several researches focused on the use of sodium hydroxide (NaOH), sodium silicate (Na<sub>2</sub>SiO<sub>3</sub>), sodium sulfate (Na<sub>2</sub>SO<sub>4</sub>), and sodium carbonate (Na<sub>2</sub>CO<sub>3</sub>) as alkaline activator for AAMs production due to their conventient availability. Few researches utilized a combinatin of NaOH and Na<sub>2</sub>SiO<sub>3</sub> in a certain percentages according to the concentration of sodium oxide (Na<sub>2</sub>O%), and water glass ratio or silica modulus (Ms) (mass ratio of SiO<sub>2</sub> to Na<sub>2</sub>O) for better activation effects (i.e., strength development,

mechanical properties). Conversely, with respect to the fact that some alkali activators, such as NaOH, and Na<sub>2</sub>SiO<sub>3</sub> induce high CO<sub>2</sub> emissions during production process, green alkaline activator (e.g., Na<sub>2</sub>SO<sub>4</sub>, Na<sub>2</sub>CO<sub>3</sub>, lime, and sodium aluminate) were also recommended for environmental sustainbility.

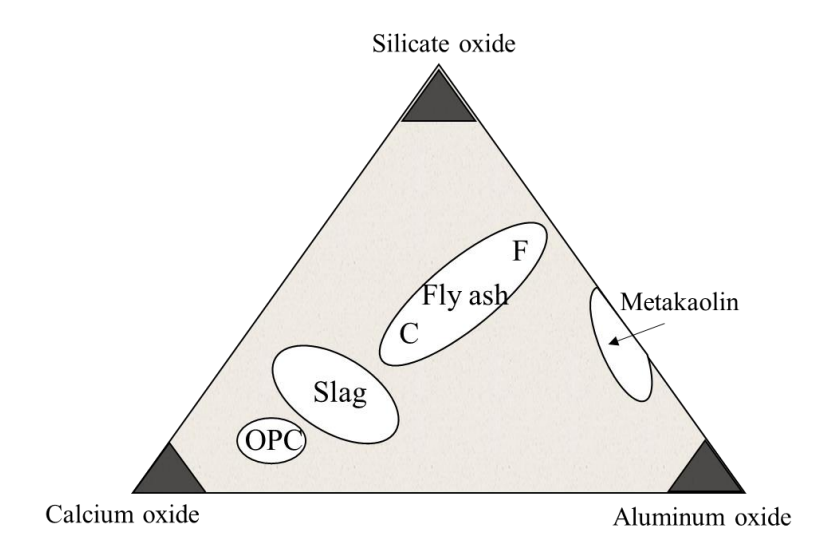


Fig. 2-2 SiO<sub>2</sub>-Al<sub>2</sub>O<sub>3</sub>-CaO ternary diagram

#### 2.1.2 Advantages and disadvantages of AAMs

The severe environmental impact of OPC production were the primary motivation for researchers to find other alternative materials. In addition, AAMs have superior properties, such as high strength, high durability and high resistance to elevated temperature, water, and corrosion [10]. Utilizing AAMs in civil engineering ranges from being used as coating and membrane materials up to be used for emergency repairing, for transportation and nuclear waste disposal [2,11–15]. Despite the advantageous mechanical properties and durability of AAMs; corrosiveness of the alkaline activator solutions used in manufacturing of AAMs has detrimental consequences, which eventually limited their in-situ applications. Also, unlike OPC materials, intensive and proper

cautions have to be followed in handling, mixing and manufacturing of those binding materials to avoid serious respiratory and burning incidents. Therefore, researchers proposed a safer manufacturing method to compensate the intrinsic setbacks of AAMs production. Instead of preparing the alkaline activator solution separately before mixing with the aluminosilicate precursors (Two-part AAMs), a solid dry activator is mixed with precursors, then "just add water" to initiate the geopolymerization reaction. This innovative technique is known as (One-part AAMs). Moreover, one-part AAMs exhibited superior mechanical properties and durability compared to that of the conventional two-part AAMs [16].

Two-part alkali-activated slag (AAS) is preferred over one-part AAS due to its superior reactivity, strength, and durability. In two-part AAS, the liquid alkali activator (e.g., sodium hydroxide or sodium silicate) is dissolved in water before mixing with slag, ensuring better dissolution of slag particles, faster reaction kinetics, and enhanced gel formation (C-(A)-S-H), leading to higher mechanical strength and durability. In contrast, one-part AAS relies on solid activators that dissolve in situ when water is added, resulting in slower activation, longer setting times, and often lower strength. Additionally, two-part AAS offers greater control over the activator dosage, improving workability and allowing for precise mix design adjustments. While one-part AAS is more user-friendly and sustainable, it generally suffers from reduced performance, making two-part AAS the preferred choice for high-performance applications requiring resilience, such as fire-resistant and self-healing materials [17].

#### 2.1.3 Mechanical properties of AAMs

Implementation of supplementary cementitious materials (e.g., GGBFS, FA, SF) as a partial replacement of OPC, have been revealed to improve the mechanical properties, rheology,

full cement replacement with pozzolanic cementitious materials in producing cement-free concrete must be demonstrated. Research was carried out to determine the structural and non-structural characteristics of AAMs. Mechanical properties, including compressive strength, tensile strength, elastic modulus, Poisson's ratio, and stress-strain behavior, were intensively investigated. Compressive strength of AAMs concrete varied based on several factors (e.g., the type of raw materials, the type and dosage of alkaline activator solutions, and the curing regimes, etc.) [18]. Slag-based alkali-activated concrete (AASC) is characterized by relatively high early strength and high strength development rate, whereas a 60 MPa compressive strength can be achieved after 1day, and more than 100 MPa can be recorded after 1-year [19]. Advanced mechanical properties of AASC can be attributed to the fast hydration reaction's rate occurred at elevated pHs. Also, the homogeneity of the dense interfacial transition zone (ITZ) whereas the strength variances between the matrix and ITZ is relatively minimal [20]. The early mechanical characteristics in AASC under heat curing schemes (65°C - 70°C) are better than those in room temperatures (26°C). However, mechanical strengths of the ambient cured samples were found slightly better than heat cured [18]. The compressive strength of AASC cured in elevated temperature (65°C - 70°C) were slightly reduced. This can be attributed to the inhomogeneity of microstructure formed in the elevated temperature curing. The rate of hydration reaction is faster than the diffusion rate leading to the settling of hydration products near the slag grains inducing interstitial spaces liable to dense precipitations forming a barrier to the ion diffusion [21]. Incorporating silica spices into the alkaline activator solution by mixing NaOH with Na<sub>2</sub>SiO<sub>3</sub>, aims to promoting the mechanical properties of AASC. Presence of silicate spices into the matrix generates a more porous hydration products around the slag particles, enhancing the diffusion of the newly formed gels to fill the interstitial

durability, and sustainability of OPC concrete [18]. Subsequently, investigating the influence of

spaces between particles, significantly improving the mechanical strength [22].

On contrary, FA-based Alkali-Activated Concrete (AAFC) has relatively low early strength, and heat curing is required to improve its early strength [23]. Due to the high activation energy for FA [24], the mechanical properties of AAFC in the ambient curing conditions (28 days at 22°C) are lower than that in the heat curing (48 hours at 50°C) [25–27].

The engineering characteristics for AASCs, AAFCs, and OPC concrete, including tensile strength, Poisson ratio, modulus of elasticity, and stress-strain relationship, were investigated by [28]. It can be revealed that tensile strengths of both AASCs, and AAFCs are significantly higher than that for the OPC concrete with similar compressive strength. Poisson's ratio for AASC and AAFC is about two-thirds that typical of OPC concrete with excellent repeatability. Young's modulus of elasticity varies linearly with compressive strength for AAFC, while the modulus remains relatively constant for AASC over the entire compressive strengths used in this study (20 MPa- 60 MPa). They attributed this conclusion to the assumption of the significant influences of microstructure, composition, and degree of hydration on the modulus of elasticity rather than the compressive strength. AAFC exhibits similar stress-strain behaviour to OPC, marked by imperfect linear elasticity followed by post-peak strain softening, but with a more rapid stress decline due to the decrease in toughness in AAFC. Conversely, AASC due to the inherent brittleness and prevalence of microstructures, exhibits highly brittle behaviour marked by near-perfect linear elasticity followed by sudden and total failure [28].

To validate AAMs in different construction applications, bond strength between steel reinforcement in comparison to OPC concrete should be addressed. Most of researchers have revealed that the bond strength between AAMs and steel reinforcement are better than OPC. This can be attributed to the more homogeneity of AAM microstructures than OPC. Morphological

studies demonstrated that ITZ between aggregate and binder matrix is denser and more homogenous in AAMs. There are no significant variances between the micro-hardness of ITZ and the alkali-activated matrix. Therefore, the stronger the ITZ is shown up into concrete, the more splitting tensile strength, and the more advanced bond strengths with steel reinforcement [18].

#### 2.2 Elevated temperature exposure

The effect of elevated temperature exposure on the mechanical properties and microstructures composition of AAMs has been investigated. Rovnaník et al. studied the microstructural changes of GGBFS after exposed to elevated temperatures (200°C - 1200°C) for 1h. Partial decomposition and dehydration of the microstructure C-A-S-H was observed up to 575°C. The principle microstructural change and mechanical strength reduction were exhibited under exposure from (600°C to 800°C) due to the complete decomposition of microstructures. Nevertheless, new significant phases start to crystalize, enhancing the mechanical properties, morphology, and pore distribution from 800°C up to 1200°C. Akermanite was revealed as the dominant crystal formed into the matrix [29].

The compressive and tensile strength of AAS declines as temperature increases. At 200°C, the reduction in strength is relatively low, but by 600°C, a significant drop is observed due to the decomposition of hydration products and the formation of interconnected cracks. Durability is also affected, with increased permeability and sorptivity making the material more susceptible to further degradation.

Specimens were subjected to various elevated temperatures starting from 200 °C up to 800 °C. An electrical heating furnace was used, where the specimens were heated up at an increasing rate of 5-10 °C/min, according to the standard ASTM E831, until reaching the targeted temperature, which

was maintained for 1h, followed by naturally cooling down at ambient temperature inside the furnace [46], as shown in **Fig.** 2-3. To ensure that the specimen core reached the targeted temperature, the temperature at the center of a dummy specimen was monitored using a thermocouple type K. Specimen's temperature, along with the oven temperature, was continuously monitored and recorded using a data acquisition system.

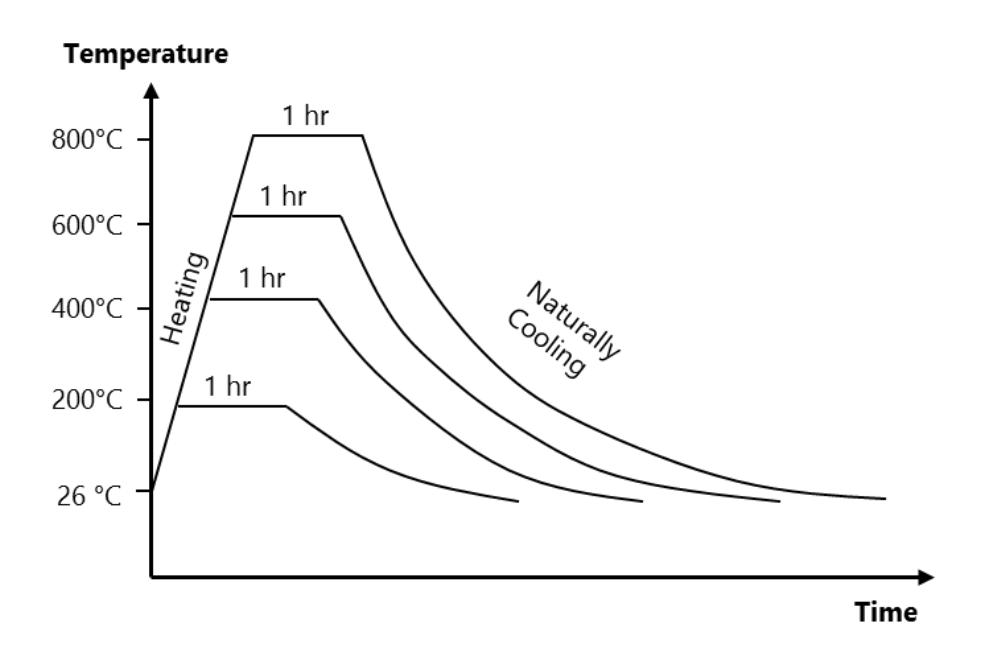


Fig. 2-3 Heat profile of exposure to elevated temperature

#### 2.3 Self-healing of materials

Self-healing of materials can be defined as the capability of the material to repair itself by closing cracks and overcoming internal defects. There are two types of self-healing; autogenous self-healing, in which the natural mode of the ongoing chemical reactions into the matrix (i.e., hydration, carbonation, crystallization, etc.) heals the cracks without any manual interference. For example, the continuous hydration of the non-hydrated particles into the binding matrix, will form a binding hydration product, enhancing the mechanical properties and durability of the defected

concrete. Moreover, in cement-based concrete and calcium-rich AAS where Ca<sup>+2</sup> is present into the matrix, in addition to the ongoing hydration process, autogenic self-healing products might also be formed due to the crystallization of calcium carbonate (CaCO<sub>3</sub>), which supports bridging the cracks, preventing aggressive materials from penetrating into the concrete matrix through cracked sections. On the other hand, calcium-free AAS have no free calcium ions to form calcite precipitations CaCO<sub>3</sub>. However, the un-hydrated particles into the calcium-free binding system can form a hydration product that will enhance the AAS gaining more strength and improving its sustainability. Secondly, autonomous self-healing, in which the cracks induced inside the concrete will be plugged using engineered materials embedded into the mixture during casting. Hollow fibers, nanomaterials, encapsulation, mineral admixture, coating, shape-memory materials, and bacteria are all different autonomic self-healing approaches aiming to enhance the mechanical properties and durability of concrete in different applications [30].

#### 2.3.1 Autogenous self-healing

Several research was conducted to investigate the potential of autogenous self-healing, exposure schemes to trigger the healing, and parameters affecting the extent of self-healing. Autogenous healing was revealed as an inherent feature of both cementitious and alkali-activated binding materials with a promising characteristic to mitigate the damage of concrete infrastructures [31]. Most researchers utilized water as a triggering agent, namely in cement-based and calcium-rich AAMs, to form autogenic healing products by initiating the rehydration reaction of the un-hydrated particles and enhancing the ions diffusion to promote the alkali-precipitations into the matrix [32–34]. However, calcium-free AAMs exhibited mechanical and durability recovery by producing a hydration product N-A-S-H through autogenous healing using high alkalinity solutions (i.e.,

#### NaOH) [35].

Incorporating heat curing in self-healing triggering regimes has its impact on the fast progress of autogenic healing. Reinhardt et al. [36] investigated the effect of elevated temperature treatment scheme (80°C) on the autogenous healing and permeability of the High- Performance Concrete (HPC). Water flow rate penetrating through the samples under a pressure hydraulic gradient equal to 1 MPa/m was measured to identify the autogenous healing. To investigate the effect of heat curing, they allocated the whole load cell in a big environmental chamber to simulate the elevated temperature. Subsequently, they revealed that the smaller the cracks induced, the more the self-healing was effective. Moreover, they deduced that cracks of widths  $\leq$  0.10 mm would be entirely and smoothly closed by self-healing. Also, increasing the temperature from 20 °C to 80 °C during self-healing will result in a faster healing process [37].

Despite heat curing treatment schemes have an influential impact on self-healing. However, the age of tested specimens is also one of the key factors controlling the extent of self-healing. Ali et al. [38] investigated the potential of self-healing in geopolymer concrete based on the availability of the non-hydrated particles embedded within the formed hydration products after the geopolymerization process. They cast 12 beams with dimensions of 25mm×25mm×145mm, then after heat curing under 40°C, 60°C, and 90°C; specimens were pre-cracked using a three-point loading test to a crack mouth opening displacement of 0.3 mm at ages 10, 24 and 52 days. Subsequently, all cracked specimens were subjected to a treatment regime under a healing temperature of 90°C for 48 hours to be reloaded at ages 14, 28 and 56 days. Eventually, it was revealed that the unreacted particles in the geopolymer-healed specimens had undergone into a geopolymerization reaction, enhancing the load capacity. Moreover, the load capacity development rate due to autogenous healing depends on the age at which the samples were tested. The 14-day

samples exhibited much more increment in the load capacity than 28-days and 56-days. This can be attributed to the density of the non-hydrated particles, which exist intensively at the 14-day age rather than at other ages. Consequently, the rate of hydration process was greater under healing at the earlier age influencing the rate of improvement in recovery strength [38].

Furthermore, type of precursors was also revealed as one of the primary parameters affecting the autogenous self-healing and the formed healing products into the matrix or on the surface of the tested specimens. Ulugöl et al. [39] investigated the effect of incorporating construction and demolition waste (CDW) materials (waste red clay brick, roof tile, hollow brick, concrete rubble, and glass) as a 100% substitutional precursor to the self-healing capability of engineered geopolymer concrete. After exposing specimens to wet and dry cycles (water at temperature 23 ± 2 °C for 24 hours, then drying at room temperature for 24 hours) as a post-crack curing regime, they revealed that self-healing in the CDW-based concrete has the same configuration as the conventional OPC. They recognized that the calcite precipitation and the formation of CaCO<sub>3</sub> was the principal self-healing agent in the healed cracks. Moreover, the continuing geopolymerization of the un-hydrated particles was detected at the end of the healing period, as well [39].

On the other hand, autonomous self-healing refers to a material's inherent ability to repair damage without external intervention, often through specially engineered mechanisms embedded within its matrix. In cementitious materials, this process typically involves encapsulated healing agents, bacterial activation, or the integration of crystalline admixtures that react with environmental stimuli such as moisture or CO<sub>2</sub>. When cracks form, these healing agents are released or activated, leading to the precipitation of secondary hydration products, calcium carbonate formation, or polymerization reactions that seal the cracks and restore structural integrity. Unlike autogenous self-healing, which relies on unreacted components within the matrix, autonomous self-healing

systems are designed to function even in severely damaged environments with minimal residual reactivity. This approach significantly enhances the longevity, durability, and resilience of concrete structures, making it particularly useful in infrastructure exposed to harsh conditions, elevated temperatures, or repeated mechanical loading [30].

#### 2.3.2 Limitation of autogenous self-healing

For the cement-based concrete, the study [40] reported that the amount of the un-hydrated particles into the concrete matrix is not the main factor in self-healing process, however, permeability and pores interconnectivity can be introduced as the key factors controlling the extent of self-healing. As shown in **Fig.** 2-4, calcite precipitations which are more likely to form at the crack entrance, will increase the concentration of ions inside the crack. Subsequently, when the supersaturation state is reached, more hydration products (i.e., calcium silicate hydrate (C-S-H), calcium hydroxide (C-H), and ettringite) will be formed inside the crack. However, permeability of solidified binder matrix and pore interconnectivity have a substantial effect on the delivery of calcium and silicate ions from the matrix into the crack. Therefore, more hydration products are potentially formed, reducing the crack widths, and enhancing the mechanical properties and durability. However, supply of calcium into the matrix will be affected by two phenomena which may cut off the water access to the un-hydrated particles:

- When the prolonged hydration densifies the microstructure, the anhydrous cement may be surrounded by an impermeable water binder matrix.
- The hydration reaction developing on the anhydrous cement freshly exposed to water may result in the rapid formation of an impermeable membrane built of ettringite, Portlandite,

and CSH. Access to other phases which can provide Ca ions, especially including Portlandite, will be affected as well.

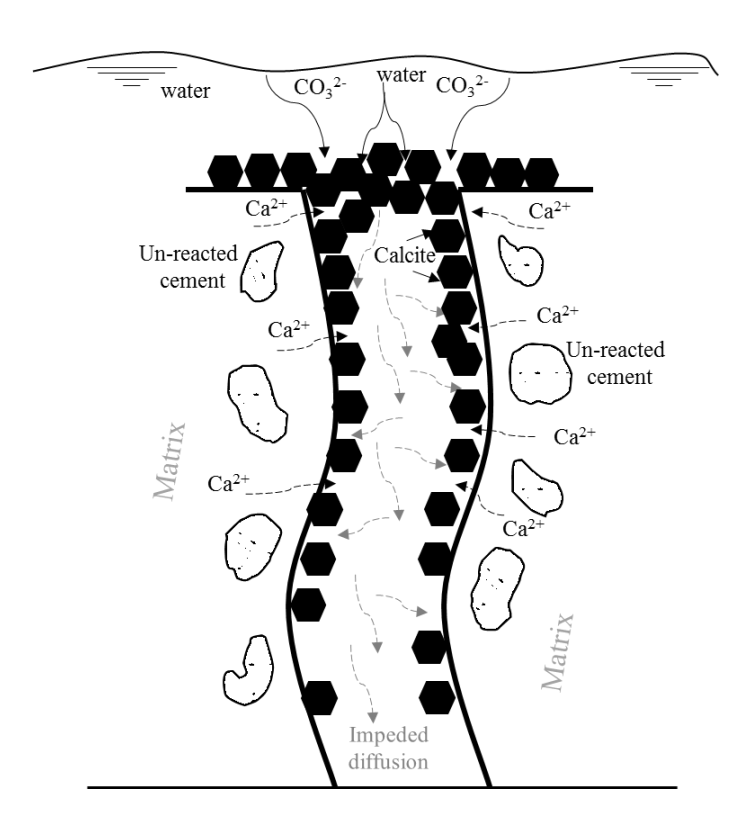


Fig. 2-4 Schematic section for proposed self-healing.

Subsequently, the ions diffusion mechanism, which is essential to promote self-healing into cracks, should be addressed. Crack opening has been revealed that it has a significant influence on the local diffusion into the matrix. Ismail et al. [41] investigated the mechanical critical crack opening, where no stresses are transferred between the fracture surfaces (i.e., crack surfaces are separate from each other). They deduced that the local diffusion inside the inert material was highly reduced when the crack opening was less than 53 µm. This can be attributed to the mechanical interaction between the crack surfaces, which impedes local diffusion [41]. For more advanced findings, they investigated the relationship between the crack opening and the local diffusion [42]. As shown in

Table 2-1, the mechanical critical crack opening was experimentally estimated to be less than 30 μm.

Table 2-1 Correlation between the crack opening and the corresponding local diffusion.

Crack opening	Effect on diffusion
Greater than 200 µm	The crack opening is not a limiting factor that will affect the diffusion
80-100 μm	The diffusion still occurs but at a slower rate. Experimentally, the reduction in diffusion can be two times.
60 μm or more	The self-healing impedes the diffusion regardless of the mortar age (28days or two years)
Less than 60 μm	The self-healing impedes the diffusion based on the mortar age.  @28days: more self-healing- less diffusion.  @2 years: less self-healing – greater diffusion.
Less than 30 μm	No diffusion

Thus, different sizes of microcracks into the matrix along with the permeability and pores' interconnectivity have been inserted and characterized in few scientific research as the term "level of damage". It also has been revealed that there is a correlation between the level of damage and the self-healing extent [35].

#### 2.3.3 Influence of damage-degree on autogenous self-healing

Investigation of the correlation between degree of damage and the autogenous self-healing was a source of much debate and scientific conflict. This study [35] investigated the correlation between degree of damage and self-healing level by investigating the permeability recovery of damaged FA-based geopolymer slurries after exposure to autogenous healing scheme. Using freeze-thaw

cycles, micro-cracks were induced into the specimens at the age of 7-days, then immersed into NaOH solution for extra 21 days for the self-healing purposes. They used the pressure transmission test (PTT) to measure the permeability into three levels (i.e., before damage, after damage, after healing). The random nature of microcracks induced into the matrix by the thermal shock exhibited different level of damage (i.e., size of microcracks), although the initial permeability of the tested samples was similar. They concluded that the level of permeability restoration representing the healing level is reversely proportional with the initial level of damage. The more the permeability at the damage level, the less the permeability recovery is obtained after healing.

#### 2.3.4 Cracks initiation and propagation

Concrete is a composite material consisting mainly of three phases (i.e., aggregate dispersed in the binder paste matrix and interfacial transition zone). Under the uniaxial compression loading, the deformation of concrete can be exhibited in terms of micro-cracks initiation and propagation up to macrocracks, closing of cracks under the act of rearrangement of matrix particles, and the matrix deformation, which can be thoroughly considered as elastic linear. According to fracture mechanics, there are three stages of concrete cracking

#### 1- Crack initiation:

Despite there are some discontinuities into fresh concrete due to compaction; however, initial micro-cracks will be mainly induced due to the differences in the elastic modulus between the aggregate and the surrounding paste matrix, which induce strain and stress concentrations, initiating micro-cracks in the interfacial transition zone.

#### 2- Stable crack propagation:

The cracks initiated in stage 1 begin to propagate. Within stage two, the cracking will multiply and propagate stably viz, when the loading stops and the stress level remains constant, the cracks propagation will cease.

#### 3- Unstable crack propagation:

The released strain energy will be enough to make the cracks self-propagate till failure. Furthermore, the crack propagation will continue, and failure will occur whether the stress level increases or not. This stage is much more likely to happen when the applied load reaches 70-90 % of the ultimate load.

Although numerous studies have discussed the fracture properties of cement-based concrete, however, very limited studies concerned with the fracture properties of AAS. The inherent brittleness and homogeneity of the alkali-activated binder matrix with its ITZ, have a significant impact on the AAS fracture properties including the fracture energy which can be defined as the energy absorbed by the material to induce a unit area of surface cracks. It has been revealed that the fracture energy exhibited by AAS is lower than that in OPC concrete [18].

#### 2.3.5 Quantification of autogenous self-healing

Despite the investigation of transport properties and mechanical characteristics were introduced as evidence for the potential of self-healing. However, researchers utilized advanced tests (e.g., scan electron microscopy SEM, x-ray diffraction XRD, and energy-dispersive x-ray spectroscopy EDX) to present an intrinsic indication of the healing products formed due to either crystalline precipitation or continuous hydration of un-hydrated particles.

## 2.4 Critical analysis for the factors affecting the extent of self-healing

## 2.4.1 Influence of damage degree on self-healing of concrete

Up to the peak loading, this study [42] have tested different types of concrete, normal and high strength, at different ages to investigate the correlation between the degree of damage and autogenous healing using a non-destructive UPV test. The velocity of UPV inside concrete is directly proportional to the intensity of microstructure and reversely with microcracks and macrocracks. Consequently, according to the velocity of UPV and its dependency on the intensity of microstructures, microcracks and macrocracks, they deduced the self-healing ratio and the degree of damage according to the following **Equations 1 and 2**:

$$Self-healing\ ratio\ = \frac{compressive\ strength\ after\ healing-compressive\ strength\ at\ loading}{compressive\ strength\ at\ loading} \eqno(1)$$

$$Degree of damage = 1 - \frac{UPV \ after \ peak \ loading}{UPV \ before \ peak \ loading}$$
 (2)

They revealed a damage threshold that discriminates two scenarios to represent the significant effect of damage degree on autogenous healing; before this threshold, the self-healing ratio increases with the evolution of damage degree. Contrarily, the self-healing ratio decreases with the increasing degree of damage after the aforementioned threshold. They estimated the damage degree threshold as 0.6-0.7 for normal concrete and 0.4 for high-strength concrete.

The critical limitation in this study is that they healed the deteriorated concrete when the samples exceeded beyond the peak point. Accordingly, regarding a practical point of view, that would be unacceptable to start the treatment processes after the disastrous failure of concrete. So, it would be better to monitor the behavior (stress-strain) using condition assessment of concrete, then start treatment once there are performance deficiencies.

#### 2.4.2 Effect of age and level of damage on the autogenous healing of lime mortars

Nardi et al. [43] investigated self-healing of hydraulic lime mortars and its dependency on the age

of the tested samples and the level of damage induced in lime mortars under two loading schemes (pre-peak 70% of the compressive strength and 90% post-peak). Compressive strength, UPV, SEM, and XRD were utilized to show the healing degree at different ages with respect to various levels of damage.

They have deduced that autogenous healing in mortar samples is dependent on the level of damage, as the pre-peak 70% damage schemes exhibited a higher healing behavior than the post-peak 90% scheme. Moreover, UPV results showed that the lower level of damage 70% performs very similar to the undamaged specimens before and after healing.

The variances in velocities of UPV of undamaged samples and 70% loading scheme samples were almost null. This can be considered as a substantial limitation as the pre-peak 70% load would not be representative to a level of damage because the velocity of UPV had not been changed. This simply indicates the non-existence of significant microcracks inside mortar samples after loading equal to 70% of the compressive strength. Subsequently, investigation of diverse percentages of loading, higher than 70% and up to failure, will be more convenient for both configuration of representative level of damage and precise correlation between autogenous healing and level of damage.

# 2.4.3 X-ray computed microtomography of three-dimensional microcracks and selfhealing in engineered cementitious composites

Fan et al. [44] have revealed that the extent of self-healing in cementitious materials also depends on the crack width and depth. Precise microcracks volumetric characterization prior to and after treatment had significantly affected the direct quantification of self-healing. Subsequently, for quantitative characterization of autogenous healing and evolution of micro-cracks propagation, 3D

x-ray computed microtomography  $\mu$ CT was used. Using four-point loading flexural test, they experimentally investigated an engineered cementitious composite ECC beam with dimensions  $300 \times 76 \times 12$  mm. The specimen was loaded up to failure, then two small cubes with dimensions of  $10 \times 10 \times 10$  mm, representing different crack patterns (width and depth), were cut from the cracked beam.

After that, self-healing was triggered using a different number of wet/dry cycles (1, 5, and 10), submerging in water at a temperature of  $20 \pm 1$  °C for 24 hours, then drying at room temperature for 24 hours.

Eventually, they revealed that samples with small cracks (depth and width) had adopted fast and robust self-healing rather than other larger cracks' samples, which exhibited a low percentage of healed crack volume.

However, one of the limitations of this experiment is that two samples with specific crack geometries are not enough to figure out the influence of variation in cracks' widths and depths on autogenous healing. Therefore, a diverse pattern of cracks with different widths and depths must be addressed. Accordingly, investigating the stress-strain behavior of loaded samples; load capacity (stress), versus gradually increasing cracks' widths, depths, and numbers representing deformation (strain), will inevitably expose fair cracks variation to be simply correlated to autogenous healing.

#### 2.5 Applications of alkali-activated materials

#### 2.5.1 Repair applications

Kramar et al. [45] investigated the suitability of AAMs for concrete repair using different precursors (GGBFS, FA, and MK). For the experimental program involved in this study, repair mortars must meet the requisites of the EN 1504 series before being used in practice. As a result

of this experiment, slag mortar was unsuitable for repair applications as it delaminated from the substrate during testing procedures. On the other hand, fly ash and metakaolin precursors exhibited good mechanical properties and adhesion. The bond strength of the fly ash and metakaolin mortars ranged from 1.8 to 2.3 N/mm<sup>2</sup> and thus met the criteria of non-structural and structural repair mortars according to the criteria of EN 1504.

Despite the capillary absorption was too high in all three mixtures to be used in the structural repair according to the criteria of EN 1504-3. However, metakaolin and fly ash mixtures still have the potential to be used for non-structural repair works. Nevertheless, the problem of efflorescence was assessed in all three mixtures.

On vertical surfaces, difficulties were met when applying the FA and MK mortars. As shown in **Fig.** 2-5, these two mortars tended to sag down the surface. On the other hand, the S mortar was easier to apply as it was stiffer than the other two precursors. That can be attributed to the flowability and the setting time properties of the three tested mortars; flowability of S mortars decreases in a short time, unlike the two other mortars, FA, and MK.

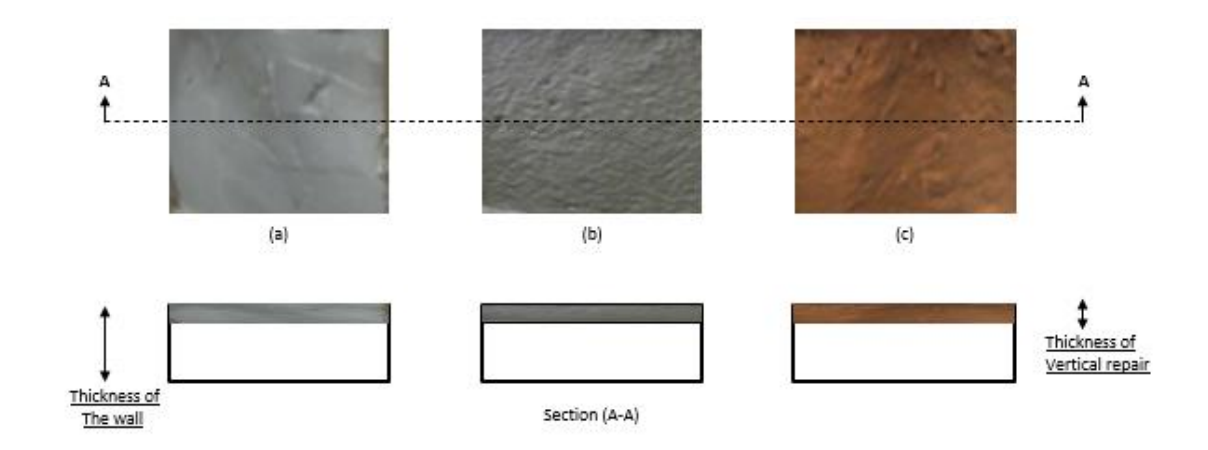


Fig. 2-5 Application of the alkali-activated mortars to a vertical concrete surface. (a) The S

#### mortar, (b) the FA mortar, and (c) the MK mortar.

Fresh properties for the three mixtures, flowability, air content, Bulk density, and setting time, were carried out. Results were illustrated as follows; after 10 min, the flow value was the highest for the S mortar (180 mm), whereas the lowest value was obtained for the FA mortar (152 mm). The high flowability of S mortar could be attributed to the low percentage of water glass present in the mixture, whereas soluble silica dissolved in the water glass has a vital role in improving the viscous properties, and flowability of AAMs depends mainly on the viscosity of the binder matrix [46]. On the other hand, the flowability of S mortar after 30 minutes decreased remarkably (from 180 to 159 mm), however the flow value in the two other mixtures, FA and Metakaolin, remained relatively constant. Deb et al. [47] deduced that flowability decreased when using ground granulated blast furnace slag as a precursor due to the angular shape of the slag particles and the accelerated reaction of calcium from slag.

The bulk densities in the three mortars ranged from 2187 to 2248 kg/m³. There were no specified differences between the three investigated AAMs for the air content value. The air content ranges from 4.1 % to 5.2%, where this percentage might be generally from 3 %to 10% in cement-based mortars. Initial and final setting times were significantly different in the three alkali-activated mortars. Whereas the initial setting time of the FA mortar had the most extended value of 2515 min, then MK mortar came next with 450 min, and S mortar was relatively the shortest with a value equal to 60 min. Similarly, the final setting time of the FA mortar was the longest with an estimated time of 2910 min, followed by the MK mortar with 505 min, and the S mortar was also the shortest with a setting time equal to 90 min. In general, using fly ash in AAMs decreases the rate of hydration reaction with low heat of hydration which results eventually in a significant long setting

time with low early strength, whereas the setting time decreases significantly with a higher percentage of slag content [46,48,49].

Compressive, Flexural, Bond strengths, Bulk density, and Modulus of elasticity were also illustrated in **Table** 2-2. After seven days, the three alkali-activated mortars' compressive strength ranged from 13.8–67.6 N/mm2. The FA mortar had the lowest compressive strength; then, the S mortar achieved higher strength; eventually, the MK mortar attained the highest compressive strength. After 56 days, there were no remarkable differences between the MK and FA mortars, whereas the S mortar achieved the lowest compressive strength. FA achieved the slowest rate in compressive strength development, as the compressive strength increased from 13.8 N/mm2 to 76.5 N/mm2 in 7 days and 56 days, respectively. This slow strength gaining can be attributed to the low hydration reaction rate with low hydration heat and low early strength of fly ash.

On the other hand, MK achieved the most rapid rate of compressive strength development, as the compressive strength increased from 67.6 N/mm2 to 71.5 N/mm2 in 7 days and 56 days, respectively. MK's high specific surface area resulting in high reactivity is the main reason for the quick gain of compressive strength. Generally, the compressive strength of the three investigated mortars was approximately within a close range (60.0–76.5) N/mm2 after 56 days [45].

Regarding flexural strength, after seven days, the tested mortars ranged from 3.1–8.8 N/mm2, being lowest in the case of using the FA precursor and highest in the case of the MK mortars. Eventually, the S mortar reached the highest flexural strength among the three mortars after 56 days (14.4 N/mm2), whereas the MK mortar (9.7 N/mm2) achieved a value close to the FA mortar (8.5 N/mm2). The amount of the precursor could be the factor that affected the flexural strength as the aggregate to solid binder ratio was approximately the same for the three tested mortars.

For the bond strength, as shown in **Table** 2-2, it was not applicable to determine the value of bond

strength in both vertical and horizontal surfaces in the case of using S mortars, as it delaminated before running the test, whereas the bond strength of the FA and MK mortars, had the range from 1.8 to 2.3 N/mm<sup>2</sup>.

Table 2-2 Mechanical properties of AAS based on the three different precursors.

Mechanical properties	7days	28 days	56 days	
Compressive strength (N/mm²)				
Metakaolin	67.6	71.2	71.5	
Slag	32.4	52.2	61.0	
Fly ash	13.8	51.1	76.5	
Flexural strength (N/mm <sup>2</sup> )				
Metakaolin	8.8	7.3	9.7	
Slag	6.5	11.4	14.4	
Fly ash	3.1	5.5	8.5	
Bond strength (N/mm <sup>2</sup> )	Metakaolin Slag		Fly ash	
Vertical surface	2	N/A	2.3	
Horizontal surface	2	N/A	1.8	

## 2.5.2 Road applications

High early strength is one of the most important properties of any repair material. Abideng et al. evaluated the performance of AAMs, in road repair applications, based on the early strength characteristics. They used the metakaolin as a precursor, mixed with parawood ash (rubberwood ash) or oil palm ash as a binder agent, as shown in **Fig.** 2-6. The experimental work was performed

based on the hot mixes process with variant heat curing times (1, 2 and 4 hours). As a result, high early strength, low drying shrinkage, high compressive strengths, and significant bond strength enhancement were considerably observed [50]. **Fig.** 2-7 indicated that the percentage of metakaolin replacement with ashes would have a remarkable effect on the bond strength. Moreover, the greater the heat curing time, the higher the bond strength along the repair surface.

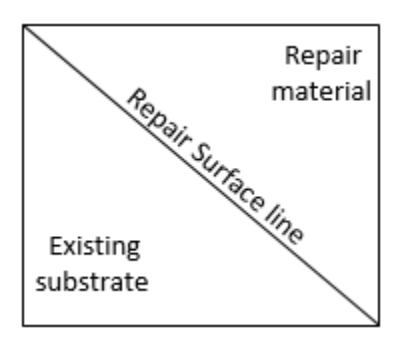


Fig. 2-6 AAMs repair mortars bonded to OPC

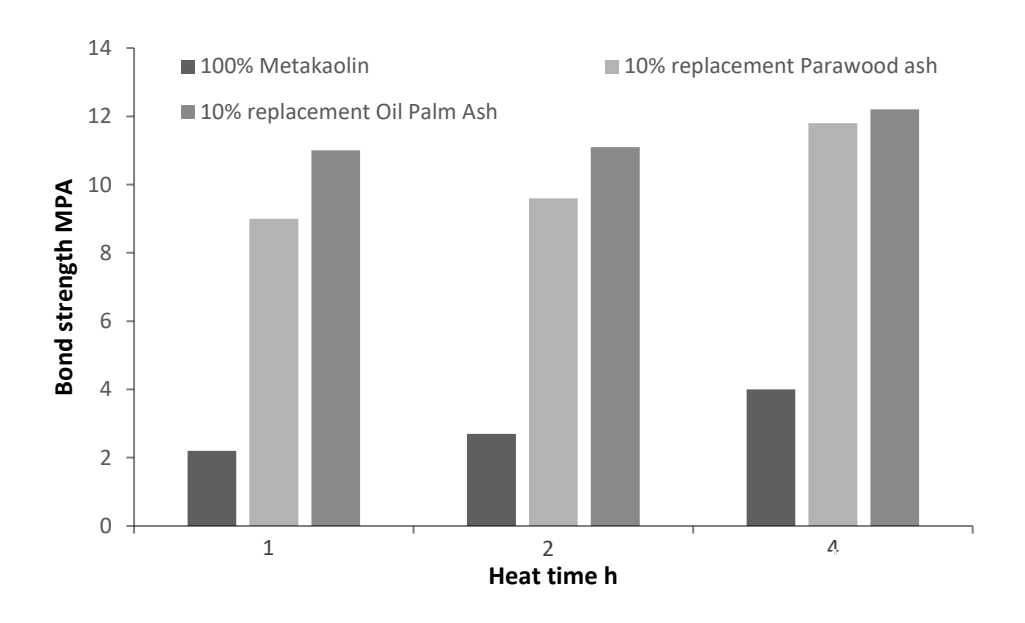


Fig. 2-7 Bond strength (AAMs & OPC), measured using Slant Shear Test.

# **Chapter 3:** Methodology and experimental plan

## 3.1 Methodology

As stated in the literature, microstructural alterations of AAS pastes have been studied after being exposed to elevated temperatures (200–1200°C) for 1h. At 575°C, a partial decomposition and dehydration of the microstructure C-A-S-H was observed. Whereas the main microstructural changes and mechanical strength reduction were exhibited under the exposure range of 600°C – 800°C, which were mainly attributed to the complete decomposition of AAS microstructures, exhibiting serious degradations and deteriorations into the matrix. While new phases start to crystallize at temperatures above 800°C, where Akermanite was identified as the dominant formed crystal, enhancing the mechanical properties, morphology, and pore distribution into the matrix. Conversely, different amorphous phases were revealed to be existing significantly into the matrix, prior to the critical exposure temperature (i.e., 800°C). Subsequently, the main concept of this research is to investigate the crystallization ability of these amorphous phases under the effects of self-healing. Potential chemical reactions (e.g., further hydration reactions of the un-hydrated slag particles, carbonation of alkalis ions into the AAS matrix) will be triggered to form self-healing products, closing the cracks as well as improving the mechanical performance of this fire damaged AAS.

#### 3.2 Experimental Plan

AAS samples will be exposed to different elevated temperatures (i.e., 200°C, 400°C, 600°C, and 800°C). Autogenous self-healing will be triggered as shown in the following tasks. To quantify the extent of self-healing, Microscopical inspection, compressive strength, ultrasonic pulse velocity (UPV), water sorptivity, rapid chloride penetration test (RCPT), scanning electron microscope

(SEM), and X-ray diffraction (XRD), 3D X-ray microtomography (μCT), will be conducted. The experimental plan for this dissertation is illustrated in **Fig.** 3-1.

**Research Phase #1:** "Investigate the potential of self-healing of AAS after being deteriorated under severe elevated temperatures exposure".

Through this phase, AAS self-healing potential will be investigated by applying post-fire curing, using two different mediums (i.e., water, and sodium hydroxide solution), separately. Water would enhance the ions diffusion into the matrix, promoting the formation of self-healing products (e.g., microstructures, alkalis precipitations, other crystals). The sodium hydroxide solution, in addition to the similar role of water, would highly improve the self-healing extent due to its ability to target the un-hydrated slag particles existing into the matrix forming more hydration products. This phase will take approximately nine months.

**Research Phase #2:** "Investigate the synergetic effect of the alkali-activator dosage and the post-fire curing schemes on the AAS self-healing".

According to results of task #1, which reveal the potential of AAS self-healing after fire exposure, further self-healing triggering will be encouraged by investigating the synergetic effect of the alkali-activator dosage coupled with the applied self-healing schemes. To elaborate, different activator dosage, i.e., upon the silica modulus, and percentage of sodium oxide, as well as different post-fire curing schemes i.e., ambient curing, Water curing, solution curing, heat curing, and drywet cycles, will be conducted to specify their effects on improving the performance of fire-damaged AAS specimens. The preliminary results of this phase have revealed significant variances in the mechanical recovery of the self-healed specimens upon the involved parameters. This phase will take approximately fourteen months.

**Research Phase #3:** "Incorporation of agents to promote the self-healing ability of AAS after fire

## exposure".

In this phase, four autogenous self-healing agents' categories, stated in the literature, will be incorporated into the AAS mixture, to investigate their effect on the recovery behavior of the fire damaged AAS composites. Mineral admixture (i.e., crystalline admixture, bentonite minerals); Fibers (i.e., polyethylene, PVA, polypropylene); nanofillers (i.e., nano SiO<sub>2</sub>, multi-walled carbon nanotubes MWCNT); curing agents (i.e., light weight aggregate, superabsorbent polymer) will separately be considered as the autogenous self-healing agents to improve the AAS self-healing performance after exposure to severe elevated temperatures.

# **Experimental work program**

#### Phase 1

# Preliminary study

Investigate the selfhealing potential of alkali-activated slag after being deteriorated under severe elevated temperatures. Mix design and self-healing scheme were selected from the literature based on the AAS self-healing ability under mechanical loading failure mechanisms.

#### Phase 2

# Characterization

Characterization of the optimum mix design. Three different activator dosage were selected because of conjugated high AAS residual properties after elevated temperature exposure. Moreover, Five self-healing schemes were determined based on their abilities to trigger AAS self-healing.

#### Phase 3

# Agents

Incorporation of autogenous self-healing agents in the optimum AAS mix design resulted from Phase No.2.

Fig. 3-1 Phases of the dissertation

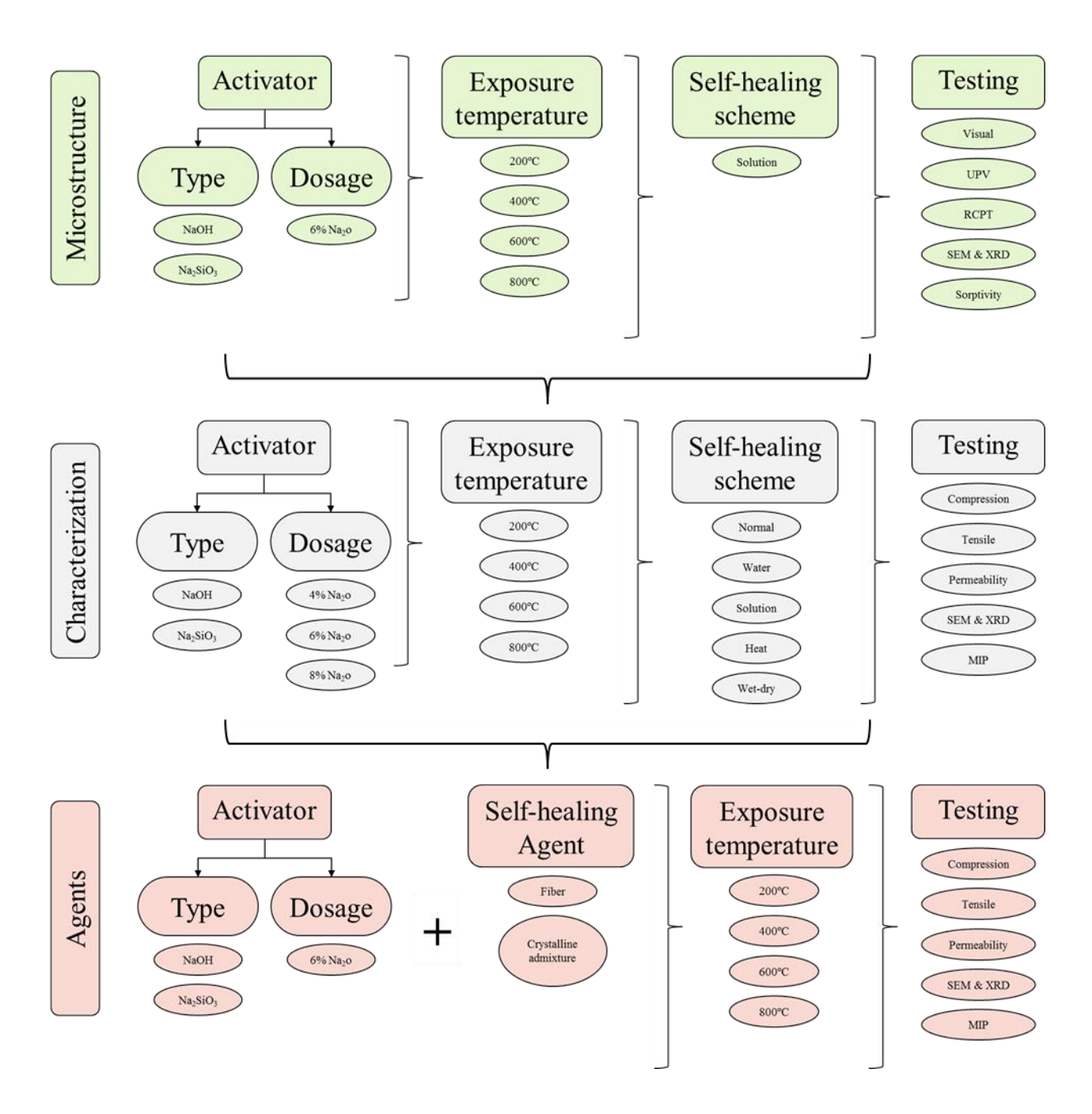


Fig. 3-2 Experimental plan

# **Chapter 4:** Effect of activator dosages on autogenous self-healing

#### 4.1 Abstract

Alkali-activated slag (AAS) is a potential alternative binder for ordinary portland cement (OPC) with a lower carbon footprint. Despite its higher mechanical and durability performances than OPC, AAS are susceptible to severe microstructural decompositions when it exposed to elevated temperatures. Nevertheless, post-fire self-healing of AAS was revealed as an inherent property densifying the matrix microstructures, restoring its mechanical strengths, and extending its durability. This paper examines the influence of activator dosages on the post-fire self-healing of AAS matrix. A mixed solution of sodium hydroxide and sodium silicate was adopted as the activator in this study. Different dosages reflecting various level of activations (i.e. low, medium, and high) were selected according to the silicate modulus (M<sub>s</sub>) and sodium oxide percentage (Na<sub>2</sub>O%). Results showed that mixtures with low activation dosage exhibited the lowest post-fire damage percentages and highest self-healing ability. Calcite precipitations were able to close surface cracks up to 250 µm. This precipitation improves the matrix durability by preventing aggressive substances to ingress. Moreover, mixtures with high activation dosage were able to acquire the highest mechanical recovery, approximately 20% of the compressive strength with respect to fire-damaged specimens. The higher ions concentrations of the high activation dosage were effectively diffused to initiate the hydration reaction of existing un-hydrated slag particles, increasing the microstructures intensity. These findings emphasize that different dosages of alkaliactivated slag could be effectively utilized to produce fire-resistant construction materials with enhanced resilience. The specific dosage can be tailored for different applications depending on the desired outcome, whether focused on durability or mechanical recovery.

#### 4.2 Introduction

AAS is adopted as a promising approach alternative to OPC, with less carbon dioxide contribution [51–53]. AAS is a 3-D network structure, chemically produced through a geopolymerization process. The high alkalinity solution (i.e. activator) dissolves the aluminosilicate precursor [54], then under a polycondensation reaction, the alkali-activated gel (e.g. calcium-aluminum-silicate-hydrate C-A-S-H) which possesses a high binding characteristic is intrinsically produced [55]. Furthermore, it was widely reported that this AAS products exhibit mechanical behaviors similar to that obtained from OPC [56–59].

Nevertheless, exposing AAS to elevated temperatures has a severely impact on its microstructures and subsequently its mechanical strength [60]. Rovnaník et al. [29] stated that a dehydration and partial microstructural decomposition occurred progressively into the matrix exposed to temperatures 200 °C to 600 °C. However, different amorphous phases were clearly detected as they are intensively existing into the matrix. At 800 °C, a complete decomposition of the AAS main hydration product (i.e. C-A-S-H) was reported [29], where most of the previously detected amorphous phases disappeared and new crystallized phases developed [29].

Self-healing was emphasized as an inherent property of AAS [61]. It was revealed that un-hydrated slag particles of the original matrix have the capability to undergo into a further geopolymerization reaction (dissolution and polycondensation) to produce more hydration products promoting the crack closure [62]. Furthermore, calcium cations existing into the AAS matrix, are able to react with the carbon dioxide (CO<sub>2</sub>) to form calcium carbonate (CaCO<sub>3</sub>) precipitations, sealing the cracks [63]. For instance, Nguyễn *et al.* [33] investigated the mechanical recovery and the microstructural morphology of self-healed AAS specimens under the effect of post-damage water immersion. It was reported that treated specimens exhibited about 41% mechanical recovery relative to the

reference AAS samples. This was attributed to the development of microstructure and formation of C-(N)-A-S-H upon exposure to water self-healing. Furthermore, calcite precipitations were also identified as the dominant self-healing products.

Alkaline activator type was disclosed as a key factor influencing the mechanical behavior and longterm durability of AAS [64]. Sodium silicate (Na<sub>2</sub>SiO<sub>3</sub>) solution was characterized as the most effective activator [65]. However, combination of sodium hydroxide and sodium silicate was the most commonly used activator [64]. This combination is designed according to silicate modulus  $(M_s = SiO_2/Na_2O)$ , and sodium oxide content as a percentage of the binder precursor  $(Na_2O\%)$  [66] and referred to as the activator dosage. The activator dosage plays a pivotal role in determination of the mechanical strength. Aydin et al. [64] revealed that AAS compressive strength is directly proportional with the M<sub>s</sub> ratio and Na<sub>2</sub>O%. At age of 90-d and Ms=1.2, AAS compressive strength increased from 87.2 MPa to 94.8 MPa when the sodium oxide content increased from 6% to 8%. Moreover, the compressive strength increased up to 99.0 MPa when the silicate modulus increased from 1.2 to 1.6 at the 8% of Na<sub>2</sub>O. Moreover, Abubakr et al. [67] classified the activator dosages into three categories: low activation level with M<sub>s</sub> ratio of 1.00 and Na<sub>2</sub>O% of 4%, medium activation level with M<sub>s</sub> ratio of 1.25 and Na<sub>2</sub>O% of 6%, and high activation levels with M<sub>s</sub> ratio of 1.50 and Na<sub>2</sub>O% of 8%. The variations in the activator dosages have a crucial influence on the hydration rection development, intensity of hydration products and un-hydrated particles. Therefore, the current study investigated the potential of targeting these un-reacted slag particles as a self-healing approach to furtherly improve the mechanical properties and durability of AAS after fire exposure. Moreover, the distinct self-healing performances due to the variation of the intensity of the un-hydrated particles was investigated to figure out the effect of the activator concentration dosages on the extent of self-healing.

#### 4.3 Materials and methods

#### 4.3.1 Materials

A ground granulated blast furnace slag (GGBFS) with a specific gravity of  $2.92 \text{ g/cm}^3$ , Blaine fineness of 515 m²/kg, and an average particle size of 15 µm was used as the main precursor to produce the AAS for the three mixes. The chemical composition of GGBFS is shown in **Table** 4-1. A mix of sodium hydroxide (NaOH) solution and sodium silicate (Na<sub>2</sub>SiO<sub>3</sub>) solution was used as the alkali activator. Sodium hydroxide pellets with 99.9% purity were dissolved in water, and then the solution was left for 24-h at room temperature to cool down. A commercial sodium silicate solution (28.8% of SiO<sub>2</sub>, 9.01% of Na<sub>2</sub>O, 62.2% of H<sub>2</sub>O) was mixed with NaOH solution to produce the desired activators with silicate modulus ( $M_S = SiO_2/Na_2O$ ) of 1.00, 1.25, and 1.50 and Na<sub>2</sub>O of 4% 6%, and 8% by mass of the binder, respectively. Riverside sand with a fineness modulus of 2.70, a specific gravity of 2.61, and water absorption of 2.73% was used as fine aggregates.

Table 4-1 Chemical properties of GGBFS

Constituents	SiO <sub>2</sub>	Al <sub>2</sub> O <sub>3</sub>	CaO	MgO	K <sub>2</sub> O	Na <sub>2</sub> O	Fe <sub>2</sub> O <sub>3</sub>	SO <sub>3</sub>
Percentage %	36.1	10.4	37.1	13.3	0.40	0.42	0.67	1.61

Based on a previous study [67], a mortar mixture with a binder content of  $400 \text{ kg/m}^3$ , a water-to-binder (w/b) ratio of 0.44 (including water from the activator) was selected. Following the mixing sequence [67], dry fine aggregate and GGBFS were initially mixed for 1 min; then, the activator solution was added and mixed for 3 additional minutes. Cube specimens with a dimension of  $50\times50\times50$  mm, dog bones samples, and cylinders  $100\times200$ mm were cast and sealed using plastic

sheets [31]. After 24-h, all specimens were demolded and stored in sealed bags at the laboratory ambient temperature ( $23 \pm 1$  °C) until the day of testing. For microstructure and mineralogical analyses, paste samples were prepared under identical conditions to those in mortar specimens (i.e. curing, exposure temperatures, and self-healing procedure).

#### 4.3.2 Self-healing study

At 28 days, specimens were subjected to various elevated temperatures starting from 200 °C up to 800 °C. Specimens were heated in an electrical heating furnace up to the desired temperature at an increasing rate of 5-10 °C/min, according to the standard ASTM E831, until reaching the targeted temperature, which was maintained for 1h, followed by naturally cooling down to ambient temperature inside the furnace. To ensure that the specimen core reached the targeted temperature, the temperature at the center of a dummy specimen was monitored using a thermocouple type K. Specimen's temperature, along with the oven temperature, was continuously monitored and recorded using a data acquisition system.

After the elevated temperature exposure, specimens of each mixture were divided into two groups: post-fire air-cured (AC-AAS) and post-fire water-cured (WC-AAS) as shown in **Table** 4-2. For 28 days, AC-AAS specimens were kept at uncontrolled ambient temperature  $(23 \pm 1 \,^{\circ}\text{C})$  in the lab, while WC-AAS specimens were immersed in the conditioning scheme (i.e. water). This scheme was applied to trigger the un-hydrated particles to react with the existing activator ions by improving the diffusion into the matrix through inducing saturation condition. Then, all groups' specimens were tested to quantify the effect of the applied post-fire curing schemes on the extent of self-healing.

Table 4-2 Mixtures and curing conditions

Mix.	Activator		Exposed to	Post-fire curing	
	Na <sub>2</sub> O%	$M_{\rm s}$	temperature	Air	Water
AAS-1-4	4.0	1.0	_	_	
AAS-1.25-6	6.0	1.25	_	_	
AAS-1.5-8	8.0	1.50	_	_	
WCAAS-1-4	4.0	1.0	_		_
WCAAS-1.25-6	6.0	1.25	_		_
WCAAS-1.5-8	8.0	1.50	_		

In order to quantify the autogenous self-healing, the percentage of damage was initially assessed relative to the reference specimens (i.e. not exposed to fire) to reveal the residual properties of AAS specimens after elevated temperature deteriorations using Eq. 3 [48]. Subsequently, following the implementation of post-fire self-healing schemes, the percentage of self-healing was evaluated based on the differences between the damages before and after the post-fire curing [49], as shown in Eq. 4. Furthermore, the recovery percentage of the post-fire cured specimens was determined by comparing them to the reference specimens Eq. 5. The quantification methodology will rely on compressive strength, tensile strength, permeability, and sorptivity, to investigate the effect of activator dosage on the extent of AAS self-healing.

$$Damage \% = \frac{After elevated temperature exposure - Reference}{Reference} \times 100$$
 Eq. 3

$$Self - healing \% = \frac{After self healing - After elevated temperatures exposure}{Reference} \times 100$$
 Eq. 4

Recovery 
$$\% = \frac{After self healing - Reference}{Reference} \times 100$$
 Eq. 5

#### 4.3.3 Testing methods

Post-fire cured specimens were observed using a Motic 40x optical microscope, to provide an initial assessment of its surface cracks closure. Cube samples 50 × 50 × 50 mm were cast to determine compressive strength of AAS mortars according to ASTM C109/109 M standards. Moreover, dog-bone shaped briquettes with dimensions 75 mm in length, 25 mm in thickness, and 625 mm<sup>2</sup> cross-section area at the mid-length were cast, to evaluate the direct tensile strength according to AASHTO T132. Water penetration through cracked specimens was measured before and after healing. The RILEM Test Method II.4 (Measurement of Water Absorption under Low Pressure) was adopted to estimate the water permeability coefficient, k (cm/s) based on Eq. 6.

$$K = \frac{a \times L}{A \times t} \ln \frac{h_1}{h_2}$$
 Eq.6

Where, a=cross-sectional area of the pipe (cm<sup>2</sup>); L=specimen thickness (cm); A=cross-sectional area subjected to flow (cm<sup>2</sup>); t=time (s);  $h_1$ =initial water head (cm);  $h_2$ =water head (cm).

Water sorptivity test was performed according to the ASTM C1585 standard on triplicate cylindrical specimens with a diameter of 100 mm and a thickness of 50 mm. This test aimed to investigate the changes in AAS capillary pores, which control the ingress of water initiation into the matrix [31]. The capillary absorption (*I*) and the sorptivity index (*Si*) were calculated and considered to assess the rate at which water permeates. This provides insights into the influence of post-fire curing on the water ingress behavior of AAS materials. In order to further characterize and determine the content of various hydration products in the tested mixtures, small chunks were ground and sieved on sieve No. 200 for thermogravimetric analysis (TGA). Powder samples (approximately, 20 to 40 mg) were prepared and submerged in acetone to stop the hydration reaction and remove free water, then heated up to 1000°C at a rate of 5 °C/min [68]. This helped

exploring the variations of hydration products of the post-fire cured AAS due to its initial activation level. A scanning electron microscope and energy dispersive x-ray tests (SEM-EDX) were performed to examine the microstructures using Phenom ProX Scanning Electron Microscope (SEM) with EDX capability [69]. The X-ray diffraction (XRD) was performed using a Bruker D8 advance diffractometer (CuK $\alpha$  radiation, 1.5406 Å) with an imaging plate detector to collect data in a range of  $2\theta$ =  $10^{\circ}$ – $70^{\circ}$ . Morphological and microstructural compositions of post-fire cured specimens were examined to determine the formed self-healing products (e.g., hydration products, crystals, etc.) [70,71]. The obtained XRD patterns were compared to understand any variations in crystallographic phases. The identification of new crystal phases, alterations in existing phases, or the restoration of initial phases in the self-healed samples could indicate the activation of the applied self-healing scheme within the AAS materials.

#### 4.4 Results and discussion

#### 4.4.1 Visual inspection

Surface cracks were examined for post-fire cured specimens of different dosages (i.e. 4%, 6%, and 8%) using an optical microscope. Variated white precipitations were formed on the crack surfaces (**Fig.** 4-1) dependent on the initial activation dosage. Low activation mixture (Na<sub>2</sub>O%= 4% and  $M_s$ = 1.0) exhibited a complete crack closure up to 250 µm, where it was limited to approximately 50 µm in both medium (Na<sub>2</sub>O%= 6% and  $M_s$ = 1.25) and high (Na<sub>2</sub>O%= 8% and  $M_s$ = 1.50) activation mixtures. The calcium-rich matrix of the low activation mixture was able to diffuse more calcium ions Ca<sup>2+</sup> [71–73]. This calcium ions reacted with carbonate ions CO<sub>3</sub><sup>2-</sup> generated from the decomposition of the weak carbonic acid (H<sub>2</sub>CO<sub>3</sub>) which was presented into the conditioning water due to the absorption of atmospheric CO<sub>2</sub> [74]. Subsequently, more calcite precipitations

CaCO<sub>3</sub> were intensively formed, close to the cracks' openings enhancing the crack closure and self-healing extent of the low activation mixture [31].

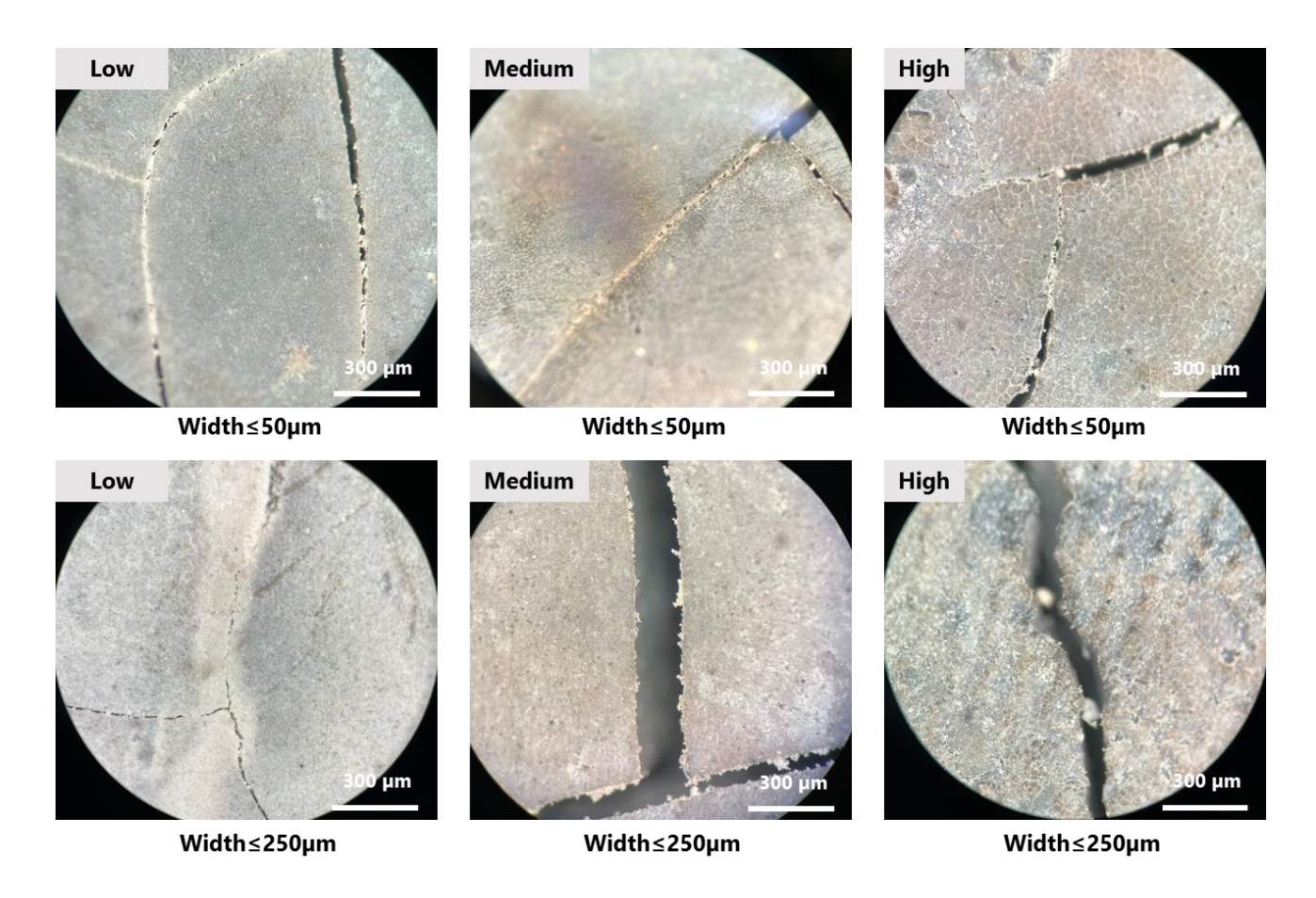


Fig. 4-1 Visual inspection

## 4.4.2 Compressive strength

**Fig.** 4-2 showed the compressive strengths of AAS mixtures specimens (i.e. 4%, 6%, and 8%) after exposed to elevated temperatures 200 °C to 800 °C, as well as its values after applying water post-fire curing scheme. When the activator dosage increased from 4% up to 8%, the compressive strength increased subsequently from 54.0 up to 80.0 MPa. This can be attributed to the more dissolution subjected to the slag particles, leading to more intensive microstructures [67]. However,

when exposed to elevated temperatures, the three mixtures exhibited different behaviors. At temperature 200 °C, WCAAS-1-4 showed a 25% increment of its reference specimen's compressive strength, which can be attributed to heat activation of un-hydrated slag particles, forming denser hydration products with lower Ca/Si ratios, contributing to the higher strength [75]. Then, a decreasing trend was observed from 400 °C up to 800 °C. This is ascribed to the partial decomposition of AAS microstructures between 400 °C and 600 °C leading to a little strength reduction [29]. At 800 °C, a steep compression reduction occurred due to the full decomposition of microstructures [29]. However, WCAAS-1.25-6 exhibited a quite different behavior due to its denser microstructures rather than WCAAS-1-4. This would initiate more cracks under the dehydration effects especially at temperature 200 °C. Then, it gradually adopted a performance similar to WCAAS-1-4 at temperatures 400 °C to 800 °C. Conversely, WCAAS-1.5-8 showed a significant reduction in compressive strength at temperature 200 °C. This can be ascribed to its highest microstructures' intensity with a finer pore size distribution. This less porous mixture experienced greater damages due to the impacts of the increasing vapor pressure [68]. Moreover, WCAAS-1.5-8 showed severer damages than WCAAS-1-4 and WCAAS-1.25-6 at temperatures 400 °C to 800 °C due to its increased microstructural decompositions.

After applying water post-fire curing, compressive strength exhibited different behavior according to the original activator dosage. WCAAS-1-4 showed very limited compressive strength improvements for temperatures 200 °C to 800 °C. While WCAAS-1.25-6 exhibited enhanced compressive strengths compared to its fire-damaged specimens under the effect of being subjected to post-fire water curing. For instance, the WCAAS-1.25-6 compressive strength increased to 66.0 MPa and to 50.0 MPa compared to 53.0 and 39.0 MPa of fire-damaged AAS-1.25-6, for exposure temperatures 400 °C and 600 °C, respectively. For WCAAS-1.5-8, it showed a compressive

strength of 54.0 and 42.0 MPa compared to 38.0 and 29.0 MPa of its fire-damaged specimens for exposure temperatures 400 °C and 600 °C, respectively. This can be attributed to the higher activator concentrations, subsequently increase the cations diffusion under the effects of the applied post-fire water curing scheme. These high-intensity cations promote the initiation of the further geopolymerization reaction, densifying the matrix microstructures.

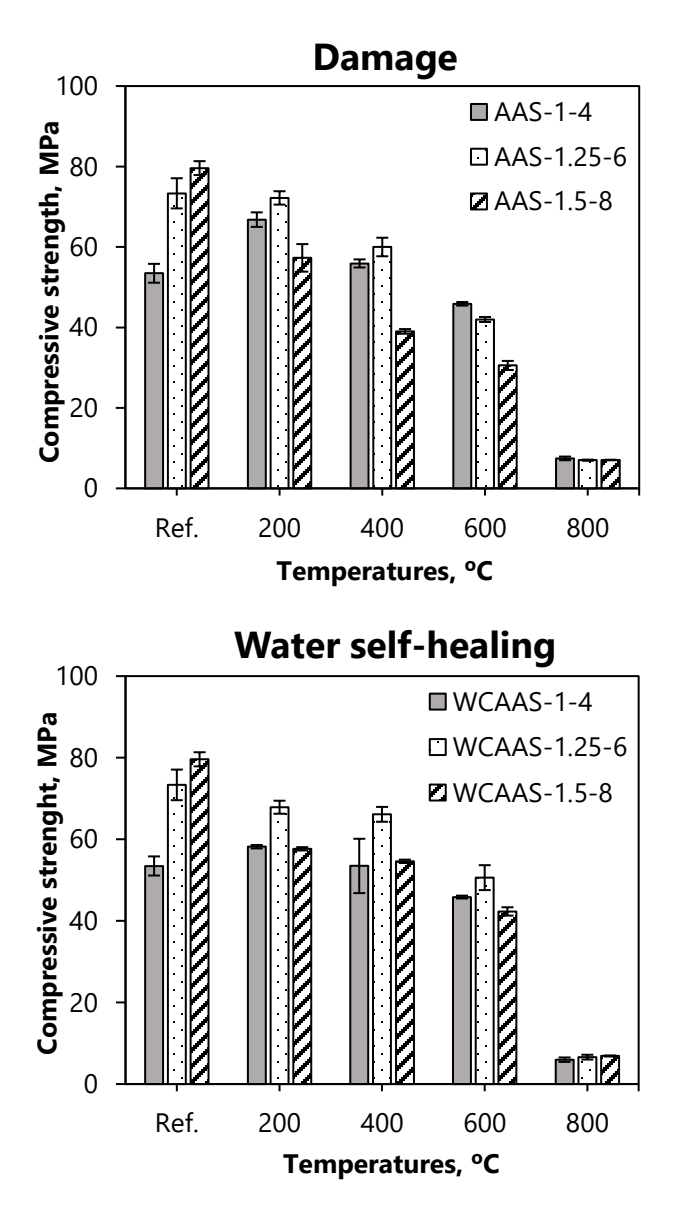
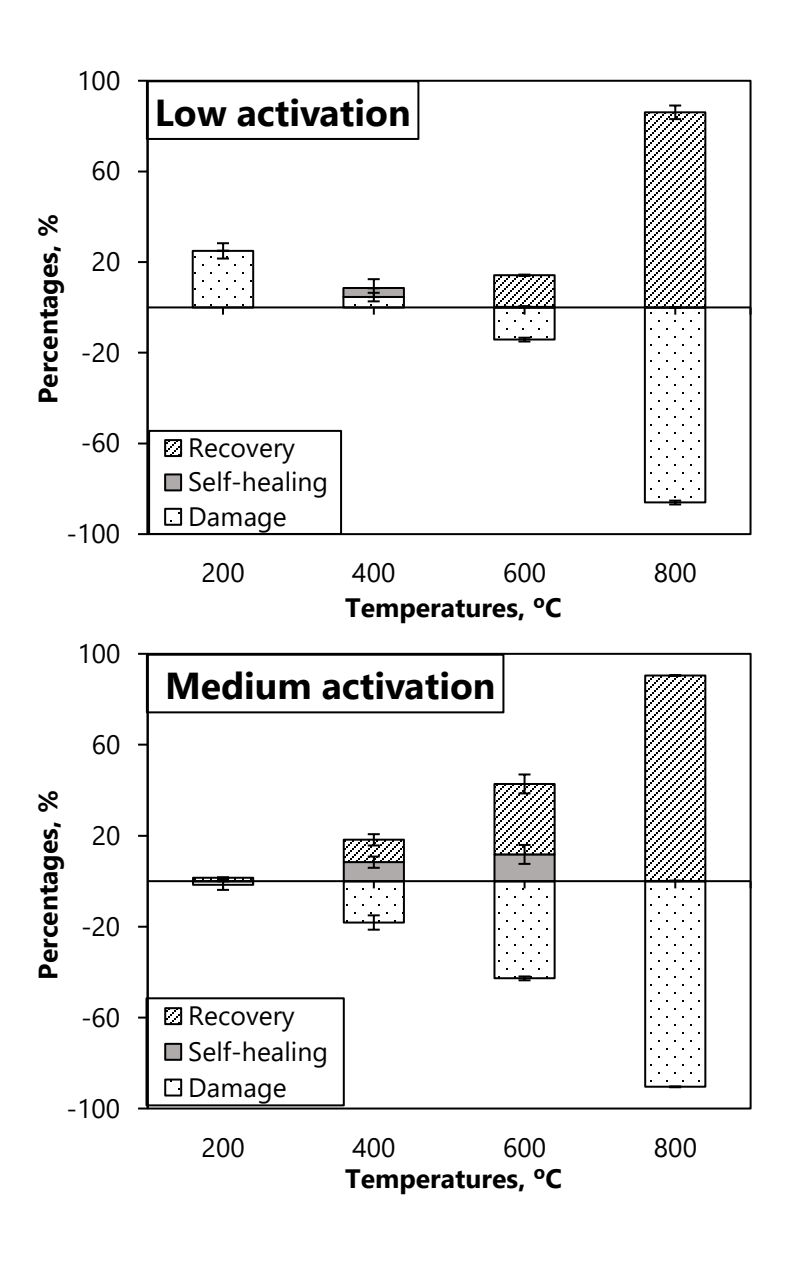
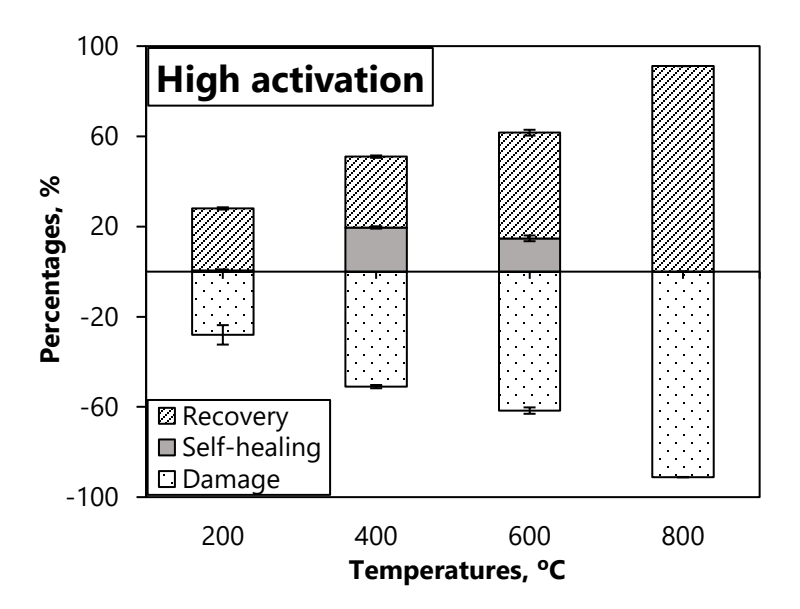


Fig. 4-2 Compressive strength for damaged specimens at age of 28 days, and post-fire water

#### cured specimens at age 56 days

Damage, self-healing, and full recovery percentages were evaluated according to the compressive strength results of AAS as described in Eq. 1, Eq. 2, and Eq. 3, respectively. As shown in Fig. 4-3, while AAS-1-4 showed the lowest damage percentages ranging from 0% at 200 °C to 20% at 600 °C. This calculated damage percentage increased subsequently when the activator dosage increased from 4% to 6% and 8%. For instance, at dosage 6%, the damage percentage increased from 1.60% at temperature 200 °C to 42.80% at temperature 600 °C. Additionally, at dosage 8%, the damage percentage increased from 28% at temperature 200 °C to 61.6% at temperature 600 °C. Similarly, self-healing percentages exhibited an increasing trend accompanied to the increasing activator dosage from 4% to 6% and 8%. Whereas the 4% mix showed very limited self-healing characteristics, this self-healing percentage increased notably in the 6% AAS activator dosage to be 8.4% and 11.8% at temperatures 400 °C and 600 °C, respectively. Furthermore, it increased in WCAAS-1.5-8 to achieve 19.6% and 14.8% at temperatures 400 °C and 600 °C, respectively. This can be attributed to the cations' greater intensity, existing in the higher activator concentrations. These ions supported the geopolymerization reactions (dissolution and polycondensation) of the un-hydrated slag particles. Under the applied water post-fire curing scheme, a microstructural densification was increased when the activator dosages increased for example, from 4% to 6% and 8%, respectively. In conclusion, the compressive strength results revealed that the low activation of AAS would exhibit the lowest damage in the AAS matrix. Moreover, although the high activation mixture assured the maximum self-healing percentages at different exposure temperatures, the medium activation thoroughly maintained the highest compressive performance at different levels i.e. after elevated temperatures exposure, and after applying the water curing.



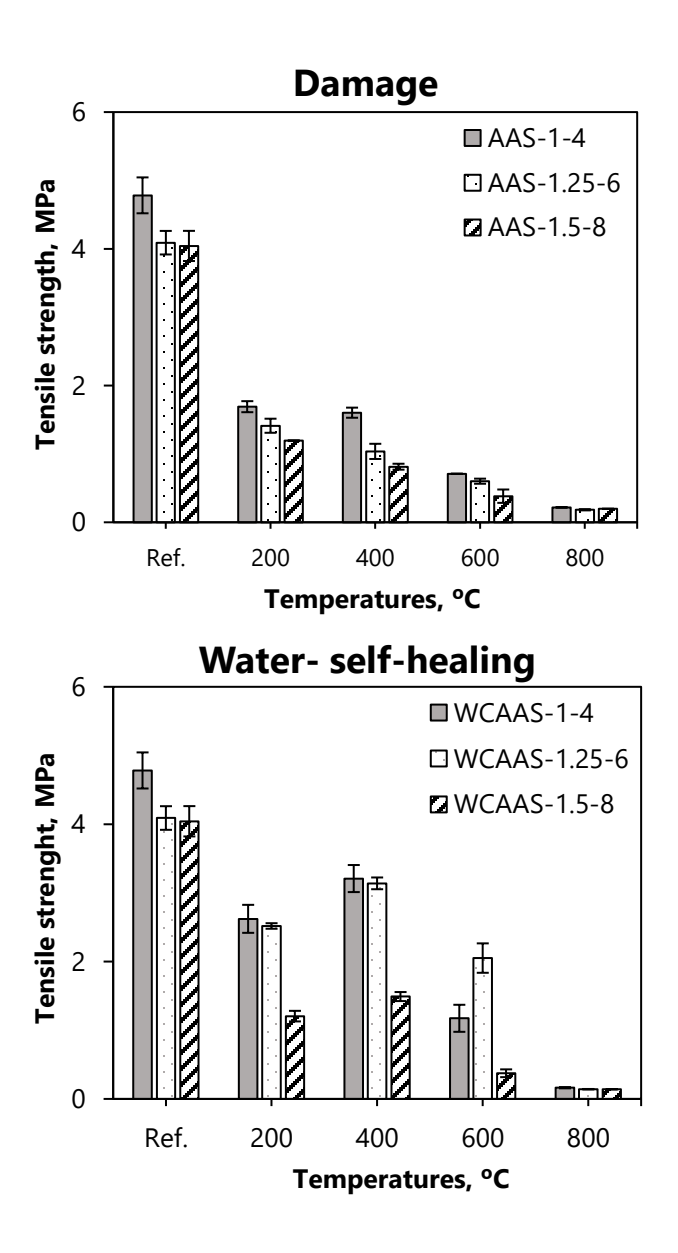


**Fig. 4-3** Self-healing percentages versus damage and recovery percentages, calculated according to the AAS compressive strength results

#### 4.4.3 Tensile strength

AAS has an entirely different behavior under tensile stresses than that of compressive stresses. The tensile strengths for the different activator dosages' AAS specimens versus exposure temperatures (i.e. 200 °C to 800 °C), in addition to its values under the effect of post-fire water curing, were illustrated as shown in **Fig.** 4-4. Due to its high brittleness characteristics, AAS-1.5-8 had the lowest tensile strengths prior to elevated temperatures exposure. Furthermore, after exposure to elevated temperatures from 200 °C to 800 °C, AAS-1.5-8 also showed a limited tensile behavior. This can be attributed to its low porous matrix with finer pore structures. Subsequently, this high activator dosage mixture was more severely affected after exposure to elevated temperatures due to non-released vapor pressure [72]. This pressure will induce internal stresses, increasing the cracks propagation. Besides, due to its high-density microstructure, more hydration products will be vulnerable at high temperatures to further decompositions, resulting in a weaker microstructure.

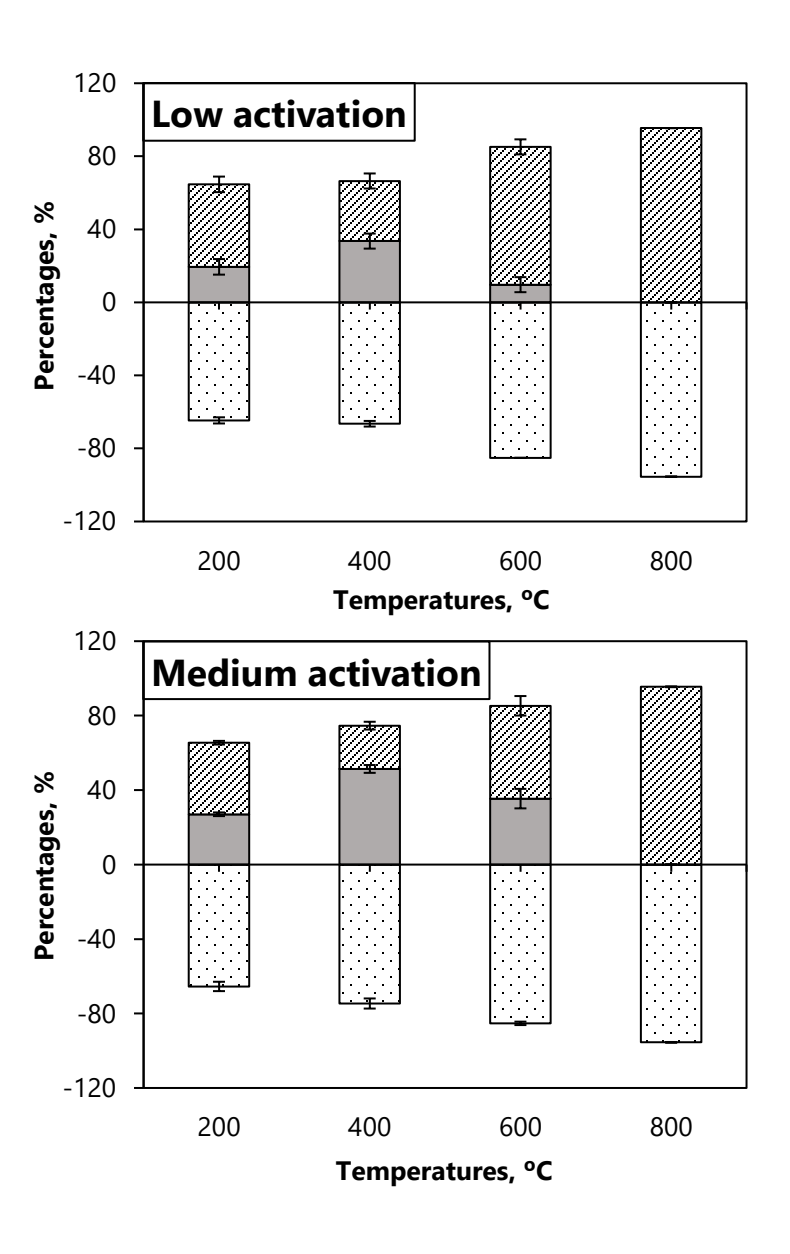
After applying water post-fire curing, variant tensile improvements compared to the fire-damaged specimens were revealed. For example, WCAAS-1-4 exhibited an enhanced tensile strength of 2.62, 3.21, and 1.17 MPa, compared to its fire-damaged specimens 1.69, 1.60, and 0.71 MPa, at temperatures 200 °C, 400 °C, and 600 °C, respectively. Also, the tensile strengths of WCAAS-1.25-6 was increased to 2.52, 3.14, and 2.05 MPa, compared to fire-damaged specimens 1.40, 1.04, and 0.60 MPa, at exposure temperature 200 °C, 400 °C, and 600 °C, respectively. This improvement for WCAAS-1-4 or WCAAS-1.25-6, might be attributed to the formation of the surface self-healing products (i.e. calcite precipitations as confirmed by following XRD), bridging the cracks and enhancing the tensile performances. Conversely, WCAAS-1.5-8 showed the lowest post-fire cured tensile behavior due to the limited formation of calcium carbonate CaCO<sub>3</sub> precipitations. About 52%, 55%, and 68% tensile strength reduction were observed in WCAAS-1.5-8 lower than that in WCAAS-1-4 at temperatures 200 °C and 400 °C, and 600 °C, respectively.



**Fig. 4-4** Tensile strength for damaged specimens at age of 28 days, and post-fire water cured specimens at age 56 days

Similar to compression strength analysis, tensile results were furtherly studied to determine the damage, self-healing, and full recovery percentages and its correlation with the original activator concentrations of AAS, as shown in **Fig.** 4-5. Subsequently, it was revealed that the damage percentages increased when a higher activator dosage was implemented. For instance, at

temperatures 200 °C, 400 °C, 600 °C, and 800 °C, damage percentage increased from 66%, 68%, 85%, and 93% to 67%, 74%, 87%, and 95%, and to 70%, 79%, 90%, and 98%, when the activator concentration increased from 4% to 6%, and 8%, respectively. Moreover, the self-healing percentages were also dependent on the activator dosage. For example, WCAAS-1-4 exhibited self-healing percentages of 19.5%, 33.6%, 9.7%, and 0%, compared to 27%, 51.4%, 35.4%, and 0%, of WCAAS-1.25-6 and 1.1%, 16.7%, 0.6%, and 0%, of WCAAS-1.5-8, at temperatures 200 °C to 800 °C, respectively. It was revealed that higher activator concentration has its impact on the intensity of the diffused calcium ions, released from the un-hydrated particles. These calcium ions are crucial to initiate the carbonation processes, producing the calcite precipitations.



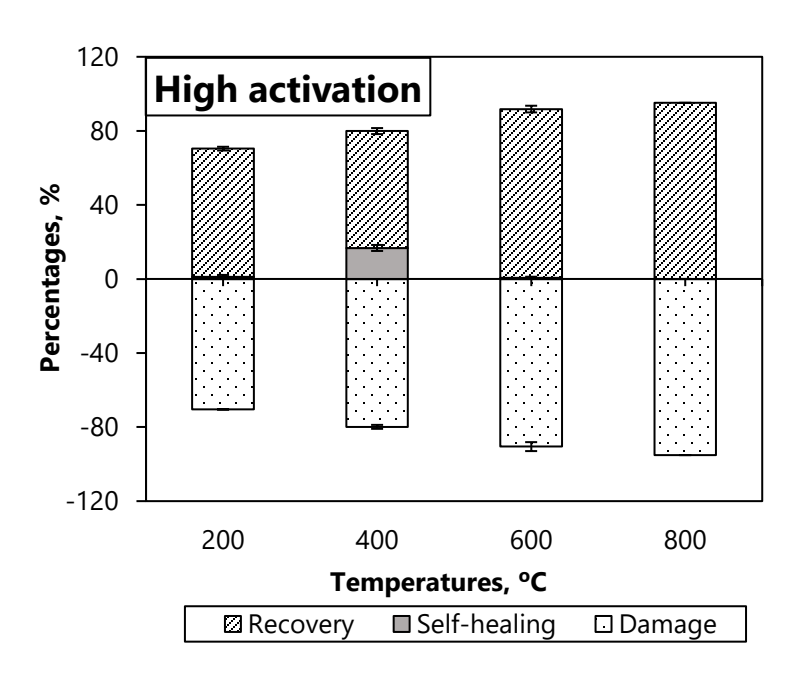


**Fig. 4-5** Self-healing percentages versus damage and recovery percentages, calculated according to the AAS tensile strength results

## 4.4.4 Permeability

**Fig.** 4-6. showed the permeability coefficient of different activator dosages specimens i.e. 4%, 6%, and 8% at age 28-d before and after exposure to elevated temperature (i.e. 200 °C to 800 °C). For reference specimens (i.e. before exposure to temperatures), water permeability was reversely proportional with the original activator dosage. Therefore, Permeability coefficient decreased from 13.9×10<sup>-5</sup> to 11.4×10<sup>-5</sup> and 9.37×10<sup>-5</sup> cm/sec, when the activator dosage increased from 4% to 6% and 8%, respectively. The higher concentrations of AAS activator increased the microstructures' density to produce a less porous matrix. Consequently, this finer pore structures led to a reduction in water permeability. After exposure to elevated temperatures, different behaviors were exhibited by the activator dosage-based specimens. For example, permeability coefficients of the AAS-1-4

specimens reduced to 8.0×10<sup>-5</sup> and 8.8×10<sup>-5</sup> cm/sec, compared to its reference samples (i.e. 13.9×10<sup>-5</sup> cm/sec) at temperatures 200 °C and 400 °C, respectively. This can be attributed to the new formed hydration products due to heat implementation. Subsequently, water permeability was impeded under the effect of the enhanced pore structure of this denser microstructure matrix [72]. Then, permeability coefficient increased to 60.5×10<sup>-5</sup> and 833.3×10<sup>-5</sup> cm/sec, at temperatures 600 °C and 800 °C due to partial or complete microstructural decompositions. For AAS-1.25-6, permeability degradation commenced at temperature 200 °C (i.e. 14.0×10<sup>-5</sup> cm/sec compared to its reference 11.4×10<sup>-5</sup> cm/sec), due to the increased internal vapor pressure of the less porous matrix. Then, permeability coefficient continued increasing to 14.7×10<sup>-5</sup>, 63.1×10<sup>-5</sup>, and 1195.6×10<sup>-5</sup> cm/sec, at temperatures 400 °C, 600 °C, and 800 °C, respectively. Also, compared to its reference, AAS-1.5-8 exhibited higher permeability coefficients 48.1×10<sup>-5</sup>, 61.1×10<sup>-5</sup>, 143.9×10<sup>-5</sup>, and 1664.6×10<sup>-5</sup> cm/sec, at temperatures 200 °C, 400 °C, 600 °C, and 800 °C, respectively.

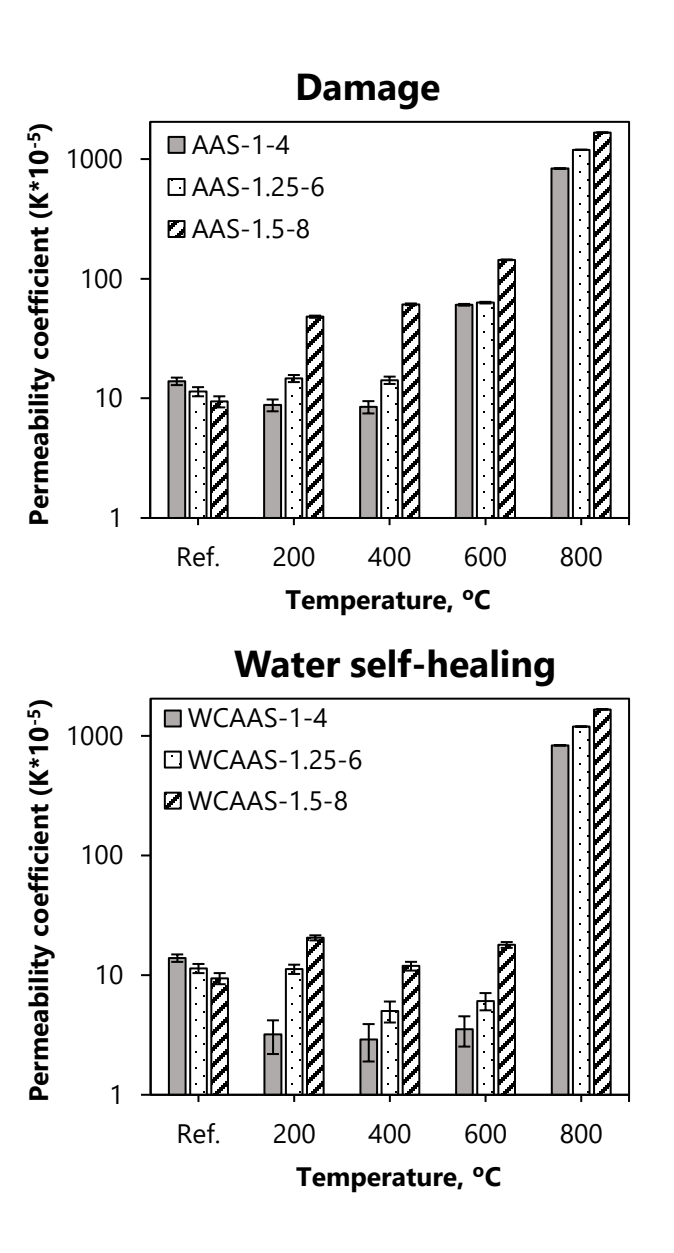
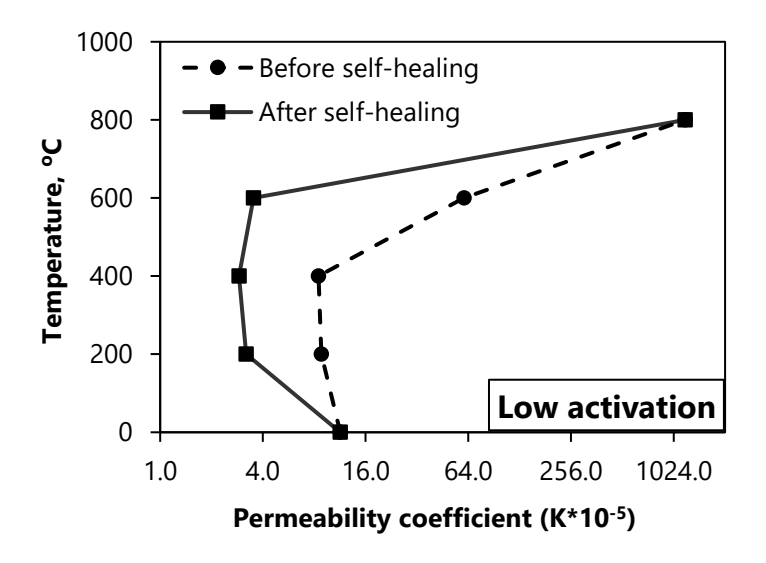


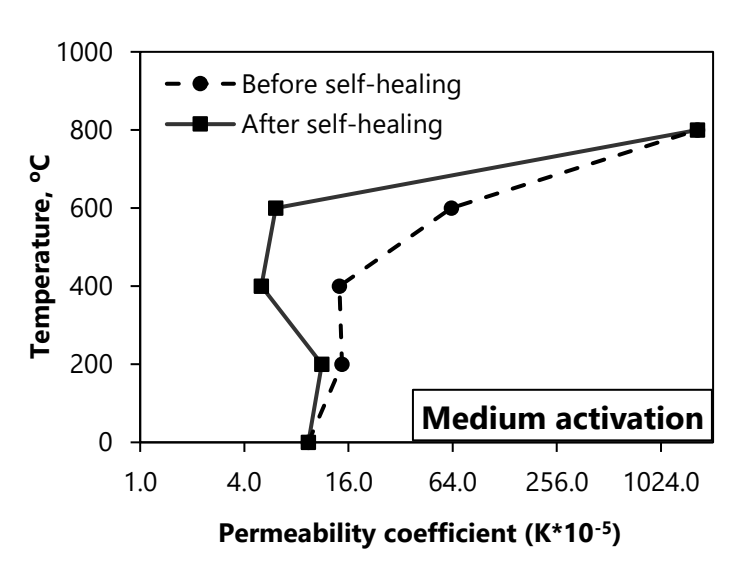
Fig. 4-6 Permeability coefficient

After applying post-fire water curing, all specimens showed a significant reduction in water permeability. WCAAS-1-4 exhibited 63%, 65%, and 94% permeability coefficients' reductions, compared to AAS-1-4 specimens, at temperatures 200 °C, 400 °C, and 600 °C, respectively. Where WCAAS-1.25-6 showed permeability coefficients 23%, 64%, and 90% lower than its fire-damaged specimens, at temperatures 200 °C,400 °C, and 600 °C, respectively. For WCAAS-1.5-8, 57%,

80%, and 87% reductions of permeability coefficients compared to its fire-damaged specimens, were revealed upon the conducted water self-healing scheme.

Fig. 4-7. illustrates the differences between the water permeability coefficients before and after applying the post-fire water curing for the three different activation dosages i.e. 4%, 6%, and 8%. After exposure to elevated temperatures, more stress concentrations exacerbating the crack propagations due to limited stress release, were observed at higher activation dosages. Also, due to the higher intensity of the hydration products into the higher concentrations' mixtures, more microstructural decompositions were progressively exhibited. Thus, permeability coefficients increased in average (i.e. summation of the increment percentages at the studied temperatures divided by the number of tested specimens) by 46% and 400% in AAS-1.25-6 and AAS-1.5-8, compared to AAS-1-4. While after applying the water post-fire curing scheme, calcite precipitations, with the crack sealing effects, hindered the water permeability into the treated specimens. Furthermore, when more self-healing products were formed, more enhanced water permeability were recorded. Therefore, permeability coefficients decreased in average by 56% and 80% in WCAAS-1.25-6 and WCAAS-1-4, compared to WCAAS-1.5-8.





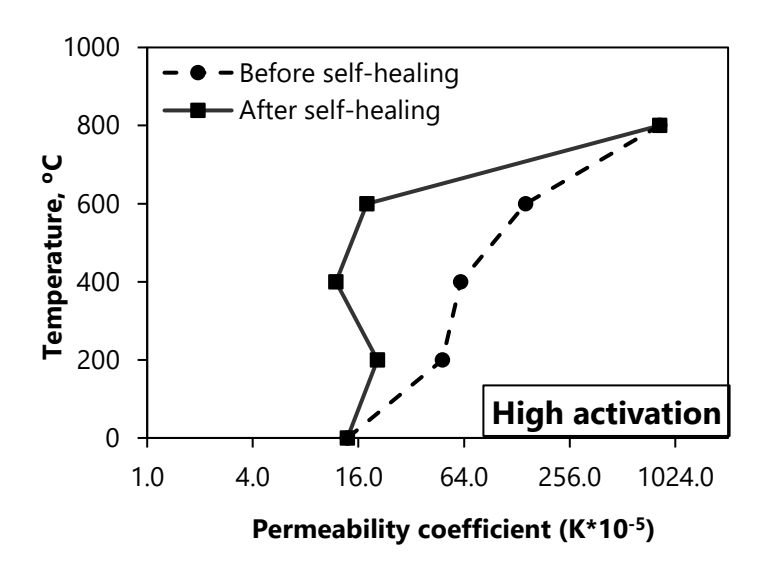
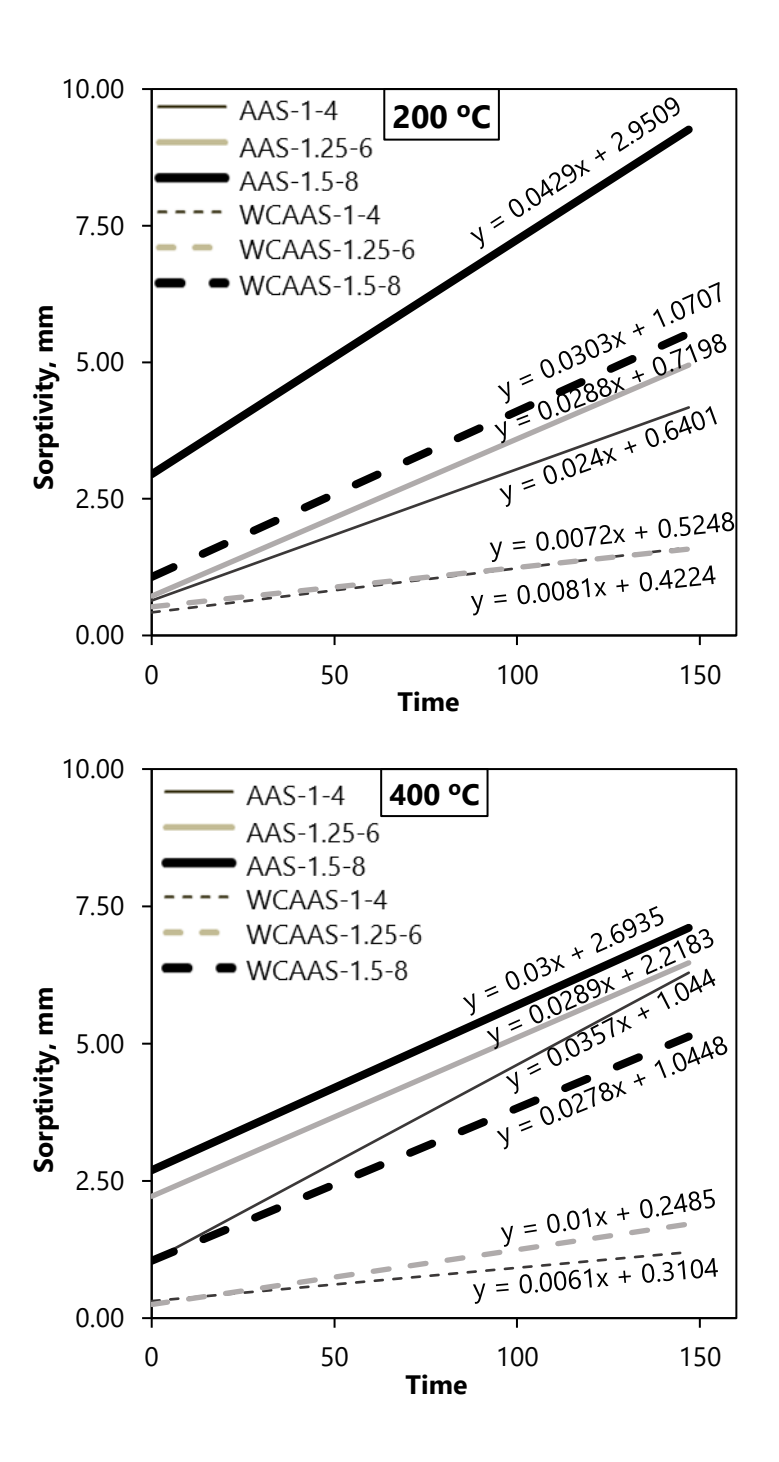


Fig. 4-7 Permeability recovery

## 4.4.5 Absorption and sorptivity

Water sorptivity index for both WC-AAS and AC-AAS specimens were depicted in accordance with the activator dosages 4%, 6%, and 8% at exposure temperatures from 200 °C to 600 °C. Water sorptivity index can be estimated using the initial absorption (for the first 6 hrs.) according to the ASTM C1585 standard, as shown in **Fig.** 4-8. This study was limited to exposure temperatures 200°C to 600°C, as the high instant absorption of the WC-AAS and AC-AAS specimens exposed to 800 °C exposure made it difficult to evaluate their sorptivity index. Distinct reductions in water sorptivity index were revealed in WC-AAS specimens rather than AC-AAS specimens. For example, water sorptivity index decreased from 1.58×10<sup>-2</sup> and 9.88×10<sup>-2</sup> mm/sec in the AC-AAS to 0.44×10<sup>-2</sup> and 3.70×10<sup>-2</sup> mm/sec in the WC-AAS for exposure temperature 200 °C and 600 °C, respectively. Moreover, sorptivity index reductions for exposure temperatures 300 °C, 400 °C, 500 °C, 600 °C, were listed as shown in **Fig.** 4-9.



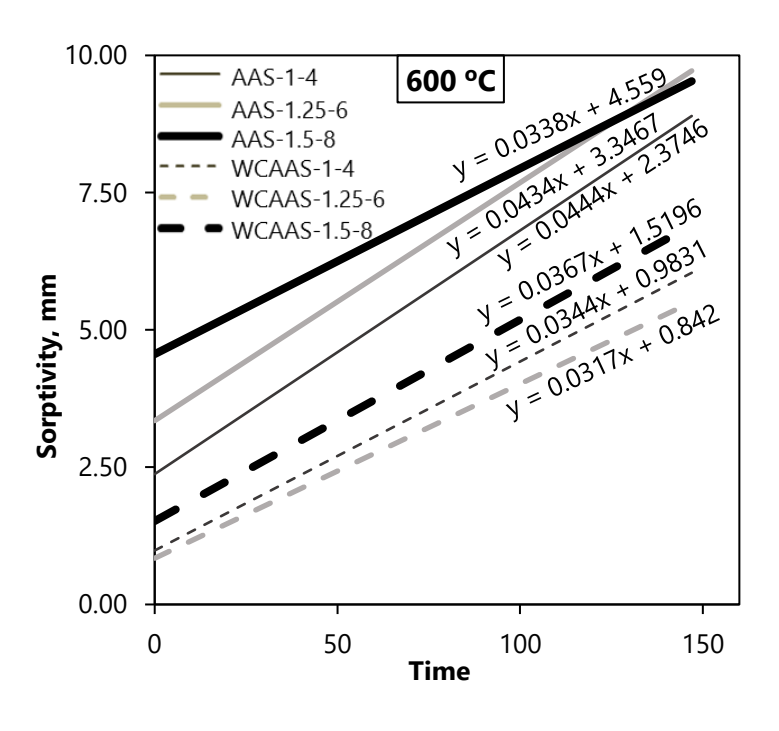


Fig. 4-8 Sorptivity

Interestingly, the self-healing percentage obtained from water absorption test was higher than that from other tests. **Fig.** 4-9 illustrates the anticipated reasons advocating the mechanism of autogenous self-healing. Specimens submerged into the post-fire water curing scheme experienced a dual effect: calcium ions would diffuse from the matrix to the crack and further hydration of unreacted slag. However, as the carbonization reaction is faster than the hydration reaction [71], calcite precipitation will impede the penetrability of the solution into the matrix [51]. CaCO<sub>3</sub> tends to become concentrated at the crack mouths to obstruct the diffusion of ions into the deeper regions of the cracks. This is one of the primary factors causing the lack of a dense matrix and reducing the mechanical recovery. The chemical reaction between calcium ions Ca<sup>2+</sup> (leakage from C-A-S-H) and carbonate ions CO<sub>3</sub><sup>2-</sup>, produced calcium carbonate CaCO<sub>3</sub> in the form of calcite that precipitates at the crack mouth [51].

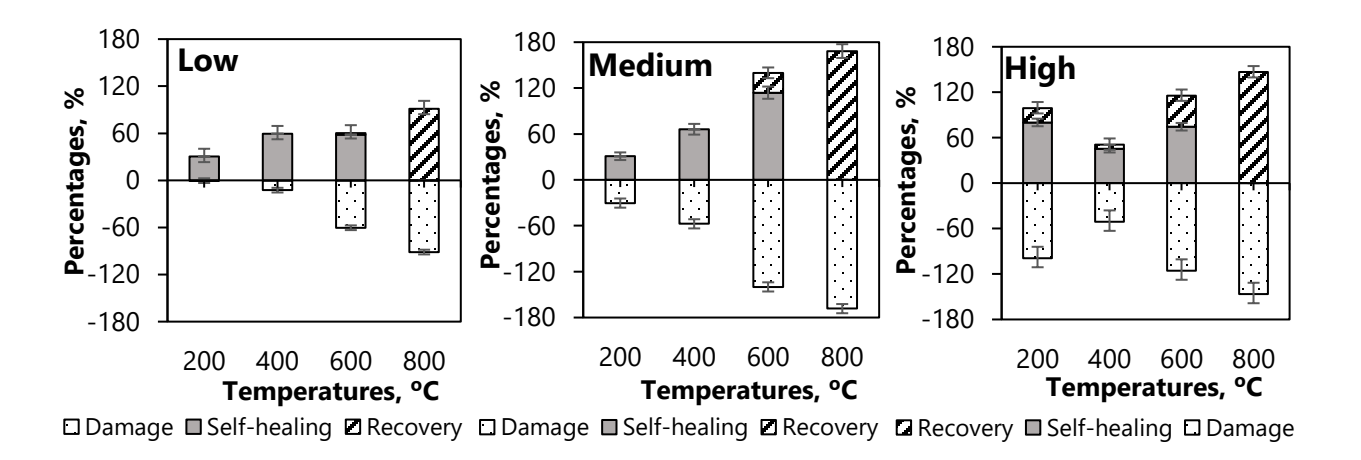
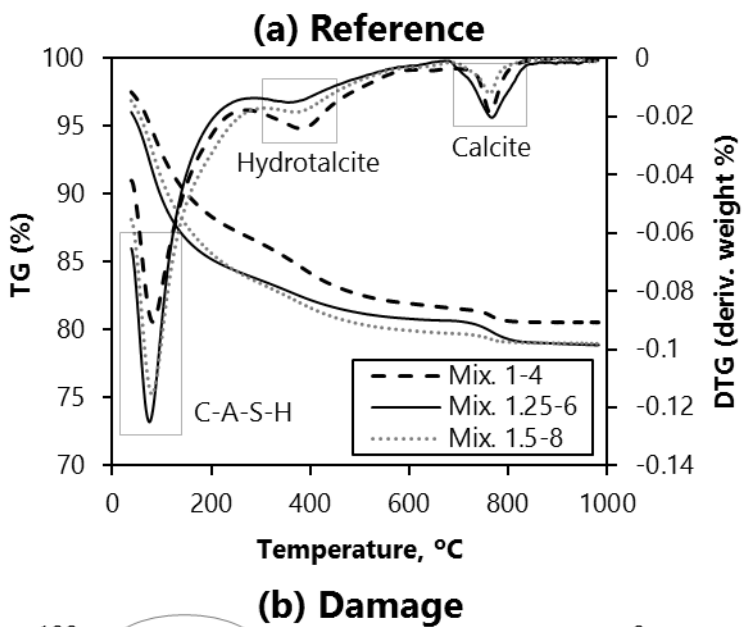


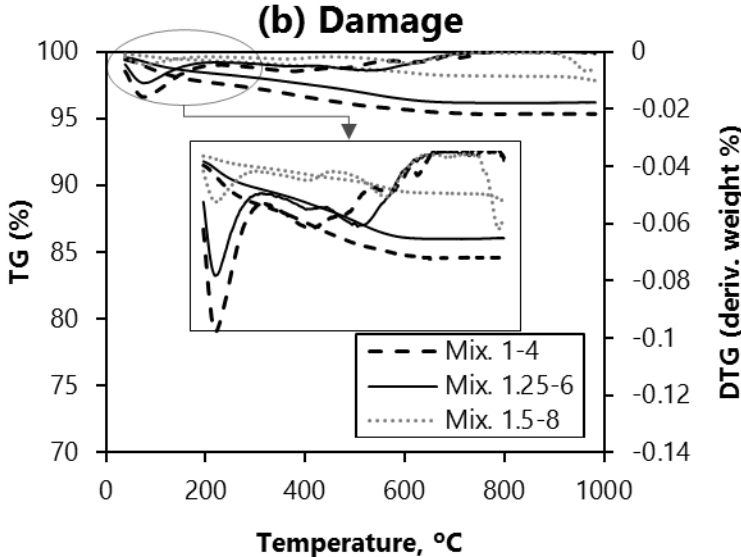
Fig. 4-9 Self-healing versus damage and recovery

## 4.4.6 Thermogravimetric analysis TGA

Thermogravimetric analysis (TGA) was performed to provide a quantitative characterization of different compositions of AAS at different conditions (i.e. reference, fire-damage, post-fire curing). Under the effects of each condition, three mixtures incorporating the studied dosages i.e. 4%, 6%, and 8%, were analyzed to evaluate the conjugated alteration and evolution of its hydration products. As it showed high self-healing performances, the WC-AAS at exposure temperature 600 °C were selected to be analyzed. As shown in Fig. 4-10, The TGA curves were plotted for the reference mixtures AAS-1-4, AAS-1.25-6, and AAS-1.5-8, where the presence of C-A-S-H and hydrotalcite for all tested samples was confirmed, in consistence with previous studies [76,77]. In general, the weight loss in the range from 40°C to 105°C is ascribed mainly to the evaporable water, hence all measurements started from 105°C. From 105°C to 215°C, the weight loss is mostly due to the loss of bound water in C-A-S-H, and from 215°C to 400°C, is the result for the release of bound water from hydrotalcite [76]. For various AAS mixtures, the bound water content was calculated from the TGA data and expressed as total weight loss between 105°C and 1000°C [22,78]. Results showed that mixture AAS-1.5-8 exhibited around 26% weight loss compared to 19% and 25% for

mixtures AAS-1-4 and AAS-1.25-6, respectively. This indicates higher progress in hydration and formation of various products as activator concentration increased. Increasing activator Na<sub>2</sub>O% dosage resulted in a rich amount of hydroxide (OH) species in the aqueous phase, increasing the precursor dissolution rate [67]. Hence, more dissolute species such as Al and Si were available to form different phases of hydration products. Moreover, as shown in Fig. 4-10, TGA results showed that specimens exposed to 600 °C had a certain amount of hydration products already decomposed. For instance, the total weight loss for the fire-damaged specimens AAS-1-4, AAS-1.25-6, and AAS-1.5-8 was around 4%, 3%, and 1%, respectively. All post-fire cured specimens exhibited variant recovery through the newly formed hydration product (C-A-S-H). This densifying microstructural formation might support the enhancement of the AAS structural performance. Moreover, the weight loss percentages of the self-healed specimens reflecting the amount of the post-curing generated hydration products, were significantly complied with the compressive strength results. Whereas the specimen WCAAS-1.25-6 has the highest formation of self-healing products (C-A-S-H) 18%, followed by the specimen WCAAS-1-4 by a percentage of 11%, while the WCAAS-1.5-8 has the lowest overall self-healing performance by a percentage of 8%.





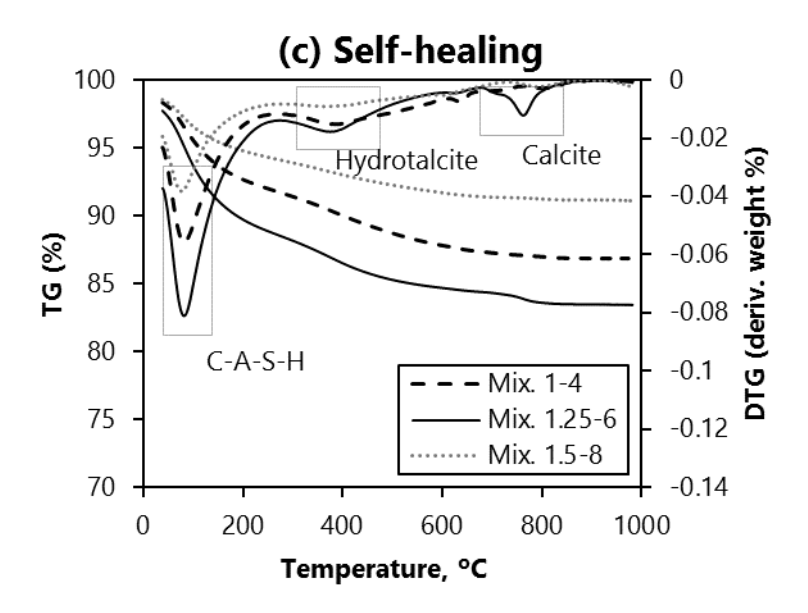


Fig. 4-10 Thermogravimetric analysis

## **4.4.7 SEM-EDX**

The 600 °C WCAAS-1-4 specimen was selected for microstructural analyses (SEM-EDX), as it showed high intensity of surface self-healing products according to the conducted optical microscope analysis. **Fig.** 4-11 depicts a typical image of self-healing products formed within surface cracks. The self-healing product had crystals of various shapes such as trigonal, cubical, and rectangular. It was revealed that the healing product was primarily composed of calcium, along with some carbon and oxygen, confirming the formation of CaCO<sub>3</sub> as a healing product.

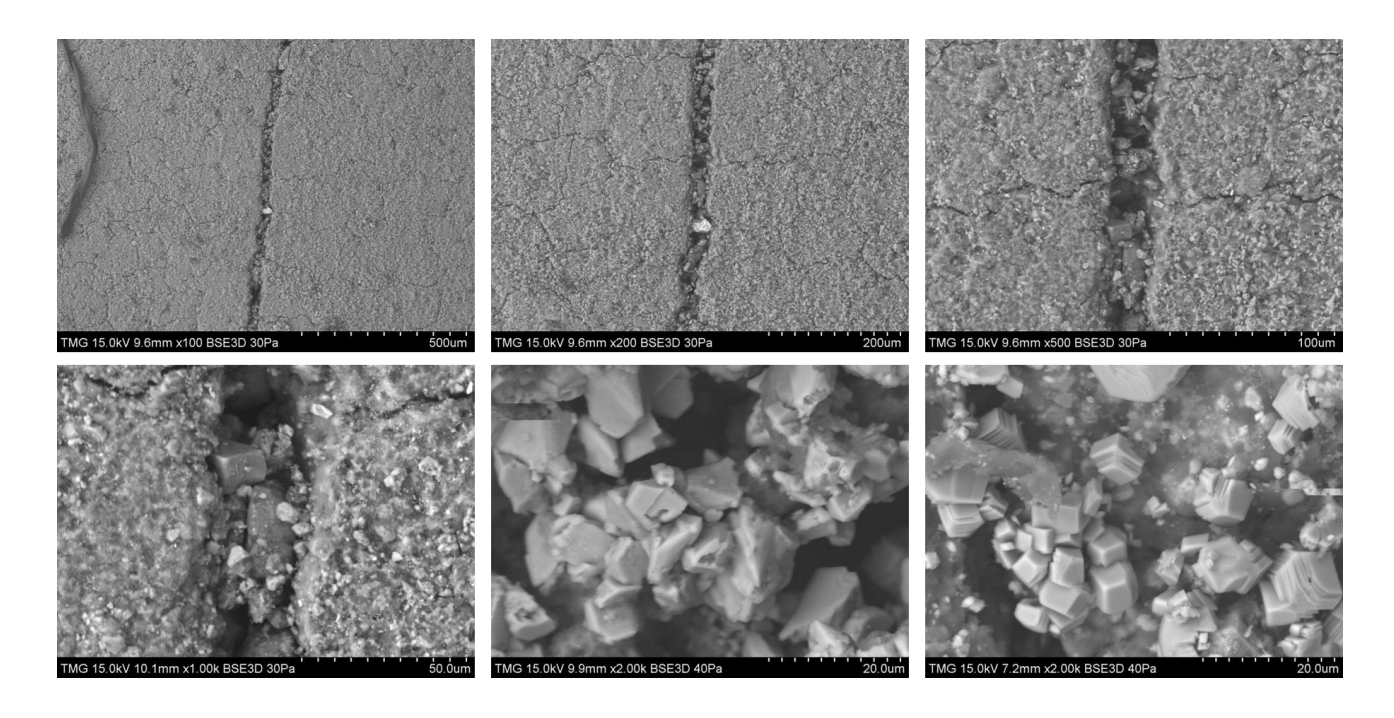


Fig. 4-11 SEM analysis

### 4.4.8 XRD

The XRD test was conducted to evaluate the self-healing potential by analyzing AAS specimens' crystalline structure and phase composition [71]. Three separate sets of samples were examined: the reference, the 600 °C fire-damaged, and the 600 °C WC-AAS. The 600 °C WC-AAS specimen was selected as it has exhibited significant recovery in compression, tensile, sorptivity, and permeability tests. From each mixture, three sets of samples were examined: the reference, the 600 °C fire-damaged, and the 600 °C WC-AAS. The 600 °C WC-AAS specimen was selected as it has exhibited significant recovery. The XRD patterns obtained from these distinct sample sets were compared to understand any variations in crystallographic phases. The identification of new crystal phases, alterations in existing phases, or the restoration of initial phases in the self-healed samples could indicate the activation of the applied self-healing scheme within the AAS materials. As illustrated in Fig. 4-12, for reference specimens (i.e. before the exposure), the main peak around

30.20 is attributed to the hydration product C-A-S-H and carbonate species due to the alkalis' carbonation in the AAS matrix [69]. Then, after being exposed to elevated temperatures (i.e. 600 °C), the main peak decreased due to the decomposition of the microstructure C-A-S-H and calcite decomposition, which started at a temperature of 400 °C [69]. However, after applying the self-healing scheme, further hydration altered the phase composition of the product significantly as the intensity of the main diffraction peak increased. This peak might be attributed to the superimposition of the diffuse peaks of the C-A-S-H gel and the strongest diffraction peak of the CaCO<sub>3</sub> crystal [96]. These self-healing products would enhance the mechanical behavior of the AAS through the formation of C-A-S-H, and its durability by sealing the surface cracks due to calcite precipitations.

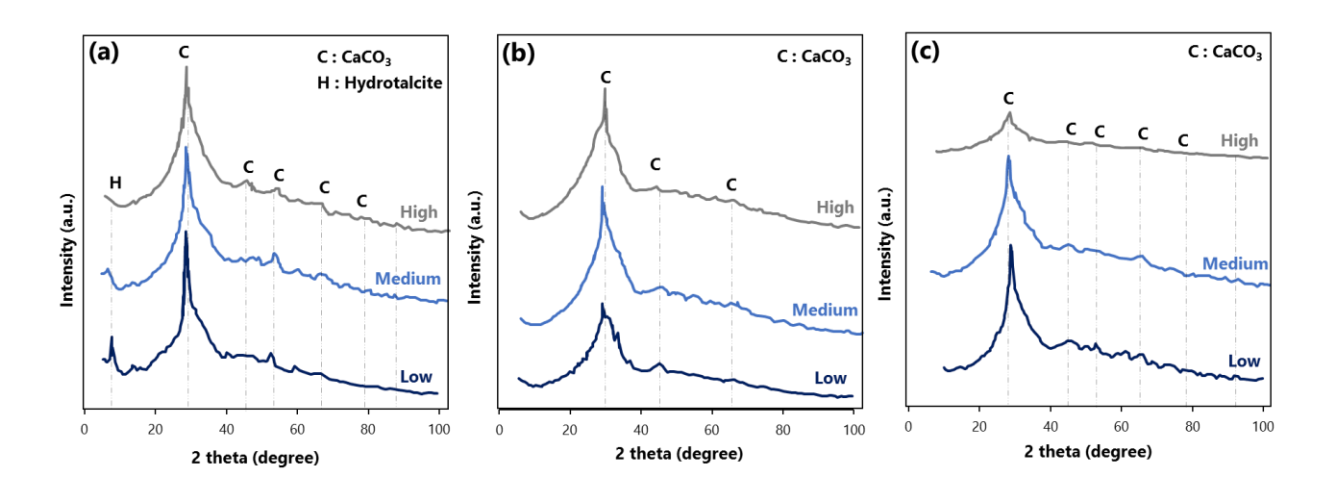


Fig. 4-12 XRD analysis for (a) reference, (b) after exposure to 600 °C, and (c) after applying water self-healing

#### 4.5 Conclusion

The effect of activator dosage implemented to dissolute the chemical compositions of slag to

initiate the geopolymerization reaction, was revealed as a key factor controlling the extent of postfire self-healing. Subsequently, the following conclusion can be drawn:-

- 1- Water post-fire curing was revealed as an effective mechanism to enhance the AAS self-healing abilities through formation of hydration products, as well as calcium carbonate precipitations.
- 2- Specimen WCAAS-1.5-8 exhibited the highest calculated self-healing percentages due to its intensive ions concentrations which support the formation of hydration products, followed by WCAAS-1.25-6 and WCAAS-1-4, respectively.
- 3- Specimen WCAAS-1-4 exhibited more calcite precipitations due to its higher calcium ions diffusion.
- 4- Although specimens WCAAS-1.5-8 and WCAAS-1-4 showed significant post-fire self-healing through different mechanisms, however, WCAAS-1.25-6 maintained the highest overall self-healing performance.

# Chapter 5: Application of Wet-dry Cycles as post-fire curing scheme to Boost Autogenous Self-healing of Alkali-activated Slag

#### 5.1 Abstract

Autogenous self-healing in alkali activated slag materials is an inherent property, which can support the mechanical performance's restoration and improve its durability and sustainability. The prolonged chemical activation of the un-hydrated particles into the matrix and the formation of the crack-sealing products are the main approaches of this self-healing characteristic. These microstructural densifications and crack closures were found that they hinder the extent of autogenous self-healing. Thus, this paper investigated the potential of improving self-healing abilities through implementation of different external self-healing conditioning scheme. The adopted wet-dry post-damage curing scheme exhibited further mechanical and durability enhancement. A percentage of approximately 30% recovery of the compressive strength was revealed upon the conducted wet-dry cycles. Although calcium carbonate was revealed as the primary self-healing product, however, a newly formed hydration product of N-C-S-H was intensively detected under the effects of the implemented dry phase.

#### 5.2 Introduction

The increasing demand for sustainable construction materials has led to the growing use of alkaliactivated slag (AAS) as an eco-friendly alternative to traditional Portland cement [77,79–82]. Not only the AAS reduces the carbon footprint of construction but also exhibits superior mechanical properties and chemical resistance [83–86].

One of the critical challenges for any construction material is its ability to withstand extreme conditions, such as fire exposure [21,87]. Fire-induced damage can severely compromise the

structural integrity of materials, leading to the formation of cracks, degradation of mechanical properties, and potential long-term durability issues [88]. It was reported that AAS exhibited a progressively dehydration and partial microstructural decomposition at temperatures 200 °C to 600 °C. While, at 800 °C, a complete decomposition of the AAS main hydration product (i.e. C-A-S-H) was occurred [29]. To address these challenges, the concept of autogenous self-healing has emerged as a promising solution, particularly in the case of AAS where different amorphous phases were clearly detected as they are intensively existing into the matrix up to temperature 600 °C [89]. Autogenous self-healing refers to the material's intrinsic ability to heal cracks and micro-damages without external intervention, primarily through the hydration of unreacted particles or the formation of new crystalline phases [90,91]. In alkali-activated slag materials, this self-healing process is triggered when water comes into contact with the unreacted slag particles, leading to the reformation of binding phases such as (C-A-S-H) gels [62]. Also, the precipitating of calcite (CaCO<sub>3</sub>) crystals produced by a calcination process of calcium ions Ca<sup>2+</sup> existing into the AAS matrix [63]. These mechanisms not only close cracks but also help restore some of the lost mechanical strength [74,92].

Post-fire treatment becomes crucial for mitigating the damage effects caused by the extreme exposure to elevated temperatures [93]. It was revealed that AAS has a self-healing capability in response to the fire-induced deteriorations. In this study [89], upon exposure to a post-fire self-healing scheme (i.e. sodium hydroxide solution), AAS demonstrated an approximately 40% recovery in permeability, where calcium carbonate crystalline phases were detected as the predominant self-healing product. Moreover, microstructural densification was observed following the formation of the hydration product C-A-S-H.

One such approach is the use of a wet-dry scheme, where the material undergoes alternating cycles

of wetting and drying [94]. This treatment not only introduces water, which is essential for the selfhealing process, but also replicates natural environmental conditions that the material would face in real-world applications [95]. The cyclical nature of wet-dry treatment has been shown to enhance the healing process by promoting the rehydration of unreacted particles and encouraging the deposition of healing products in cracks and pores [96]. For example, Yang et al. [94] investigates the self-healing capabilities of Engineered Cementitious Composites (ECC) under cyclic wetting and drying conditions, focusing on their recovery in mechanical properties and crack-sealing behavior. The study showed that ECC specimens can recover up to 76% of their initial mechanical strengths. The research also highlights that tight crack widths (below 50 µm) are crucial for effective self-healing, driven primarily by calcium carbonate crystallization within the cracks. In this study, autogenous self-healing capabilities of fire-damaged AAS subjected to a post-fire wet-dry regime should be addressed. The aim is to determine how effectively this treatment can restore the material's structural integrity by healing cracks and mitigating the effects of thermal damage. Specifically, the role of wet-dry cycles in promoting healing and the resulting impact on mechanical properties, microstructural changes, and durability performance, was investigated. Understanding these mechanisms could provide valuable insights for improving the resilience of alkali-activated slag materials in post-fire recovery scenarios and extend their applicability in fireprone environments. Furthermore, this research contributes to the broader field of sustainable construction by offering a potential strategy to enhance the long-term durability and functionality of AAS in real-world applications.

#### 5.3 Materials and methods

#### 5.3.1 Materials

A ground granulated blast furnace slag (GGBFS) with a specific gravity of  $2.92 \text{ g/cm}^3$ , a Blaine fineness of  $515 \text{ m}^2/\text{kg}$ , and an average particle size of 15 µm, was implemented as the sole precursor in this study. The GGBFS was sourced from Lafarge, located in Canada. This material conforms to the ASTM C989 [97] ensuring its quality and consistency for the intended applications. Its chemical composition is shown in **Table** 5-1. A mix of sodium hydroxide (NaOH) solution and sodium silicate (Na<sub>2</sub>SiO<sub>3</sub>) solution was used as the alkali activator. Sodium hydroxide pellets with 99.9% purity were dissolved in water (i.e. 7M), and then the solution was left for 24-h at room temperature to cool down. A commercial sodium silicate solution (28.8% of SiO<sub>2</sub>, 9.01% of Na<sub>2</sub>O, 62.2% of H<sub>2</sub>O) was then mixed with NaOH solution to produce the desired activator with silicate modulus (M<sub>S</sub> = SiO<sub>2</sub>/Na<sub>2</sub>O) of 1.0, and Na<sub>2</sub>O of 4 *wt*.% of the binder. Riverside sand with a fineness modulus of 2.70, a specific gravity of 2.61, and water absorption of 2.73% was used as fine aggregates, meeting the ASTM C778 for standard sand [98]. It was provided by a local producer, ensuring the material's uniformity and suitability for use in mixtures casting.

**Table 5-1** Chemical compositions of the used GGBFS

Constituents	SiO <sub>2</sub>	Al <sub>2</sub> O <sub>3</sub>	CaO	MgO	K <sub>2</sub> O	Na <sub>2</sub> O	Fe <sub>2</sub> O <sub>3</sub>	SO <sub>3</sub>
Percentage %	36.1	10.4	37.1	13.3	0.40	0.42	0.67	1.61

## **5.3.2 Specimens preparation**

For the mixtures proportioning along with the applied post-fire self-healing schemes, **Table** 5-2 was presented where a binder content of  $400 \text{ kg/m}^3$ , a water-to-binder (w/b) ratio of 0.44 (including

water from the activator) was selected and remained constant for the three studied mixtures. Nevertheless, the post-fire self-healing schemes were applied separately to figure out the distinct influence of each post-exposure conditioning treatment on the extent of autogenous self-healing (i.e. Air, Water, and Wet-dry cycles). Following the mixing sequence [67], GGBFS was dry mixed with fine aggregate for 1 min; then, the activator solution was added and mixed for 3 additional minutes. Cube specimens with a dimension of  $50 \times 50 \times 50$  mm, dog bones samples, and cylinders  $100 \times 200$ mm were cast and sealed using plastic sheets [31]. After 24-h, all specimens were demolded and stored in sealed bags at the laboratory ambient temperature (23 ± 1 °C) until the deteriorating day (i.e. crack initiation using elevated temperatures).

**Table 5-2** Mix proportioning and the applied post-fire self-healing scheme

Samples	Ms	Dosage Constituents' weights, kg/m <sup>3</sup>						Post-exposure curing
	1015	Na <sub>2</sub> O%	Binder	Sand	NaOH	Na <sub>2</sub> SiO <sub>3</sub>	Water*	scheme
AAS-AC	1.0	4%	540	1485	19	75	191	Air
AAS-WC	1.0	4%	540	1485	19	75	191	Water
AAS-CC	1.0	4%	540	1485	19	75	191	Wet-dry cycles

At the age of 28 days, specimens were subjected to elevated temperatures 200, 400, 600, and 800 °C, separately. Following the study [89], Specimens were heated in an electrical heating furnace up to the desired temperature at an increasing rate of 5-10 °C/min, according to the standard ASTM E831, until reaching the targeted temperature, which was maintained for 1h, followed by naturally cooling down to ambient temperature inside the furnace.

To evaluate the variances in self-healing related to different post-fire curing schemes, fire deteriorated specimens were divided into three groups: post-fire air-cured (AAS-AC), post-fire

water-cured (AAS-WC), and wet-dry post-fire cured specimens (AAS-CC), as shown in **Table** 5-2. For additional 28 days after being damaged under elevated temperatures exposure, AAS-AC specimens were kept at uncontrolled ambient temperature  $(23 \pm 1 \, ^{\circ}\text{C})$  in the lab, while AAS-WC specimens were immersed in the conditioning scheme (i.e. water). This scheme was applied to trigger the un-hydrated particles to react with the existing activator ions by improving the diffusion into the matrix through inducing saturation condition. While wet-dry cycles were carried out by immerse the AAS-CC specimens in water for 24h, then dried into an oven for the subsequent 24h, at a temperature of 65 °C. This adopted cycle was repeated until the day of testing. Eventually, at the age of 56 days, all groups' specimens were examined under the following tests to reveal the effect of applying different post-fire conditioning schemes on the extent of autogenous self-healing of AAS.

### **5.3.3 Testing methods**

Autogenously self-healed specimens were observed using a Motic 40x optical microscope, to provide an initial assessment of its surface cracks closure [89]. Cube samples 50 × 50 × 50 mm were cast to determine compressive strength of AAS mortars according to ASTM C109/109 M standards. Moreover, dog-bone shaped briquettes with dimensions 75 mm in length, 25 mm in thickness, and 625 mm<sup>2</sup> cross-section area at the mid-length were cast, to evaluate the direct tensile strength according to AASHTO T132. Water penetration through the self-healed specimens of each mixture was measured using The RILEM Test Method II.4 (Measurement of Water Absorption under Low Pressure) by calculating the water permeability coefficient, k (cm/s) according to Eq. 7.

$$K = \frac{a \times L}{4 \times t} \ln \frac{h_1}{h_2}$$
 Eq.7

Where, a=cross-sectional area of the pipe (cm<sup>2</sup>); L=specimen thickness (cm); A=cross-sectional area subjected to flow (cm<sup>2</sup>); t=time (s);  $h_1$ =initial water head (cm);  $h_2$ =water head (cm).

Water sorptivity test was performed according to the ASTM C1585 standard on triplicate cylindrical specimens with a diameter of 100 mm and a thickness of 50 mm. This test aimed to investigate the changes in AAS capillary pores, which control the ingress of water initiation into the matrix [31]. The capillary absorption (I) and the sorptivity index  $(S_I)$  were calculated and considered to assess the rate at which water permeates. This provides insights into the distinct influences of the applied post-fire curing schemes on the water ingress behavior into the self-healed AAS mixtures. In order to further characterize and determine the content of various hydration products in the tested mixtures, small chunks were ground and sieved on sieve No. 200 for thermogravimetric analysis (TGA). Powder samples (approximately, 20 to 40 mg) were prepared and submerged in acetone to stop the hydration reaction and remove free water, then heated up to 1000°C at a rate of 5 °C/min [68]. This helped exploring the variations of hydration products of the self-healed AAS under the effect of different post-fire schemes. The X-ray diffraction (XRD) was performed using a Bruker D8 advance diffractometer (CuKα radiation, 1.5406 Å) with an imaging plate detector to collect data in a range of  $2\theta = 10^{\circ}-90^{\circ}$ . Morphological and microstructural compositions of the self-healed specimens were examined to determine the formed self-healing products (e.g., hydration products, crystals, etc.) [70,71]. The obtained XRD patterns were compared to understand any variations in crystallographic phases. The identification of new crystal phases, alterations in existing phases, or the restoration of initial phases in the self-healed samples could indicate the activation of the applied self-healing scheme within the AAS materials.

#### 5.4 Results and discussion

## 5.4.1 Visual inspection

Upon completion of self-healing conditioning phases (i.e. age of 56 days), the 600 °C fire-damaged self-healed specimens were examined under an optical microscope. Specimen exposed to wet-dry post-fire cycles, exhibited intensive white precipitations, expanded over the specimen surfaces, and concentrated on the crack mouth openings (**Fig.** 5-1). The shown crack mapping displayed a complete crack closure for cracks with initial widths up to approximately 250 μm. During wet-dry cycle, the implemented water immersion phase supported the ions diffusion into the matrix, ensuring ions delivery from the matrix (high cations concentrations) to the cracks (lower cations concentrations) [99]. Meanwhile, the subsequent dry phase led to more white precipitations due to the enhanced chemical reaction of the highly diffused Ca<sup>2+</sup> calcium ions with atmospheric CO<sub>2</sub> to furtherly promote the formation of white calcium carbonate crystals [100].

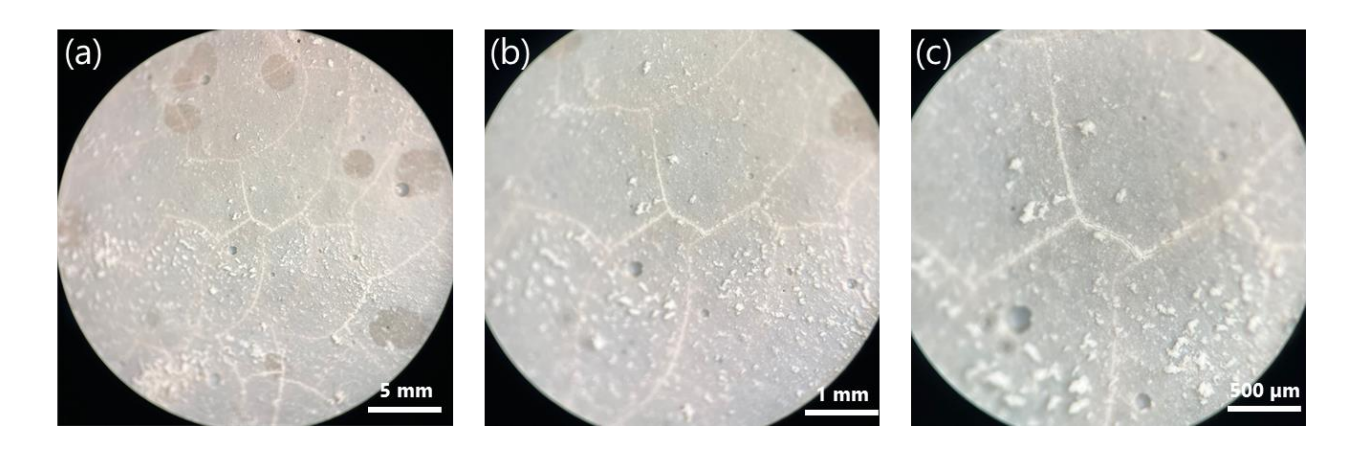
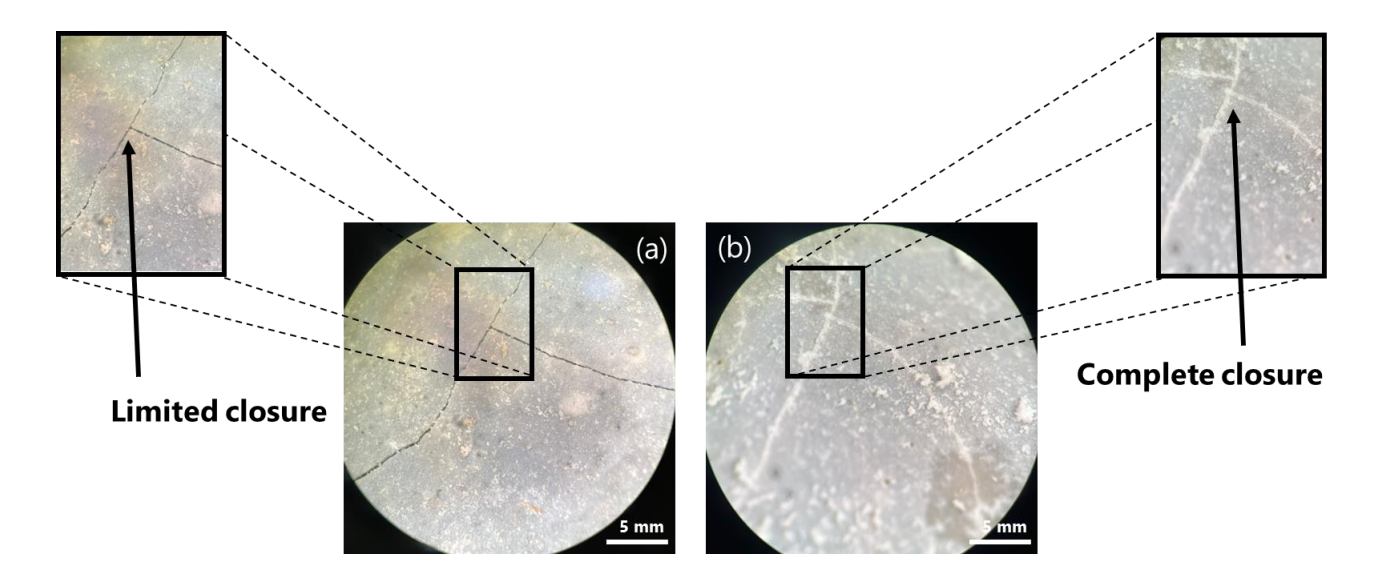


Fig. 5-1. Crack mapping of the wet-dry self-healed specimens after 600 °C

Conversely, specimens which were subjected to ambient air post-fire scheme, remained unchanged without any remarkable alteration of the crack widths [89]. However, the water post-fire cured specimens exhibited a slightly improved crack closure, nevertheless, limited when compared to the

AAS-CC. **Fig.** 5-2 illustrated the differences between AAS-WC and AAS-CC where separate self-healing procedures were applied after an identical exposure temperature of 600 °C. For the shown highlighted crack widths of 200 µm, AAS-CC exhibited a complete closure, surpassing the AAS-WC specimens which showed a limited closure. This observation advocated the implementation of wet-dry cycles to improve the self-healing ability of fire-damaged AAS.



**Fig. 5-2.** Differences in crack closures, (a) water post-fire curing scheme (b) wet-dry post-fire curing scheme, after deteriorated under 600 °C

## **5.4.2** Compressive strength

The normal, water and wet-dry post-fire curing schemes were investigated under compressive strength testing to figure out their different influences on the extent of autogenous self-healing and the conjugated mechanical performances. **Fig.** 5-3 showed the compressive strength versus the exposure temperatures. While the samples subjected to wet-dry post-fire scheme exhibited the highest compressive strength at temperatures 200 °C to 800 °C, water curing showed also higher performance than normal curing. For instance, at exposure temperature of 400 °C, wet-dry cured

samples reached up to approximately 70 MPa compressive strength, whereas normal and water cured samples had 54 and 57 MPa, respectively. Similarly, at temperatures 600 °C and 800 °C, wetdry specimens showed the highest values among the two other schemes 52 and 10 MPa, respectively.

For normal and water cured samples, compressive strength results were reversely proportioned with the exposure temperatures. Compressive strength values slightly declined when the exposure temperature increased from 200 °C to 400 °C which can be attributed to the non-significant damage exhibited into the matrix due to the bounded water leakage. This low damage hindered the water curing scheme to penetrate deeper into the matrix to initiate the self-healing. At temperature 600 °C, although a steep declination was observed for both normal and water cured samples, however, the effect of water conditioning scheme was more obvious and created higher mechanical performance than that in the normal curing. This was ascribed to the more deteriorations induced into the matrix due to the decomposition of the hydration products into the matrix. This deterioration allowed more water penetration during self-healing conditioning, densifying the AAS microstructures.

On the other hand, wet-dry specimens showed a significant increment in the compressive strength when exposure temperature increased from 200 °C to 400 °C. While the wet cycles improved the ions diffusion into the matrix, the dry cycles supported the acceleration the geopolymerization reaction into the AAS matrix. This increased the intensity of the hydration products, developing higher mechanical performance. At temperature 600 °C, although the generation of newly formed hydration products was effectively continuing, however, the microstructural decomposition-based damage overweighed the ability of autogenous self-healing to achieve the full recovery of the AAS matrix. This notably reduced the compressive strength results at temperature 600 °C lower than

400 °C.

The main reaction product of wet-dry cured AAS is Na-substituted C–S–H with low Ca/Si ratios, which contribute to the higher strength. This can be attributed to the formation of a finer pore size distribution, denser and compact structure of matrix, increase of hydrated parts of slag grains, and stronger aggregate matrix interface due to the lower Ca/Si ratio of C–S–H. Also, the incorporation of high silica modulus Ms into the original matrix affected this Ca/Si ratio as this ratio also decreases with the increasing Ms values, contributing to the higher strength of the wet-dry post-fire cured AAS mortars. This might be due to; the transformation of porous and poorly packed structure to a denser and compact structure by increasing of Ms. Also, Ca/Si ratio of C–S–H decreased with the higher values of Ms, and the porosity decreased with the increasing Ms values. These alterations lead to formation of a more durable matrix [75].

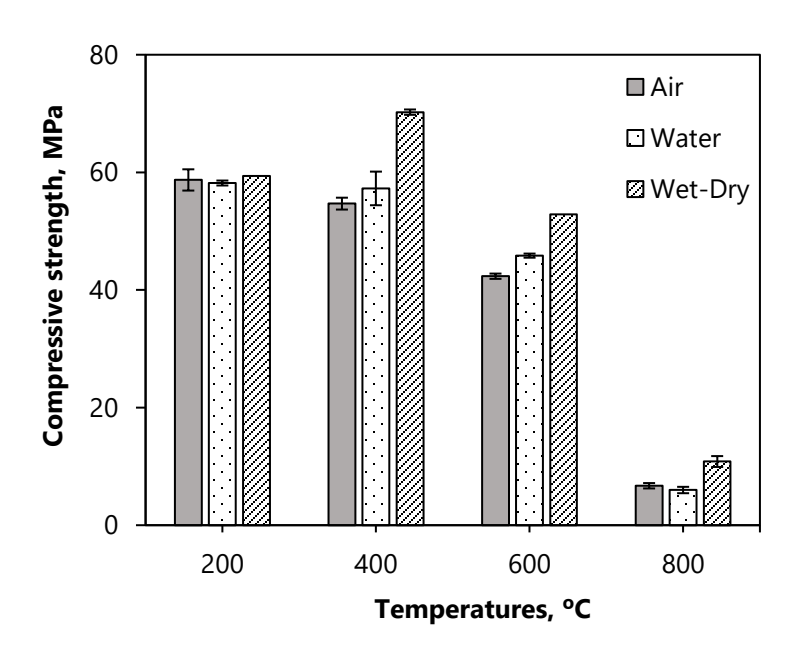


Fig. 5-3. Compressive strength of self-healed specimens (air, water, and wet-dry)

## **5.4.3** Tensile strength

The tensile strength results from the investigation into the autogenous self-healing of alkaliactivated slag under varying curing conditions; air curing, water curing, and wet-dry curing, provide valuable insights into the material's performance and potential applications. Three distinct sets of samples were tested as shown in **Fig.** 5-4, to evaluate how each curing method influences the self-healing capabilities of the alkali-activated slag. Among the curing methods analyzed, the wet-dry curing approach yielded the most promising results in terms of tensile strength. Interestingly, the tensile strength values of the wet-dry cured specimens were lower than those of the water-cured specimens. This observation suggests that while water curing typically promotes the hydration process, the wet-dry curing regime encourages a unique mechanism of autogenous healing that enhances the material's structural integrity.

The underlying reason for the superior performance of the wet-dry curing method lies in the increased formation of denser hydration products (i.e. NCSH) within the matrix. The alternating exposure to wet and dry conditions facilitates a more pronounced and efficient development of these hydration products, leading to improved bonding and cohesion within the material. However, it is essential to note that this denser formation may also contribute to increased brittleness in the wet-dry cured samples. The brittleness can be attributed to the reduced porosity and the high degree of hydration, which, while enhancing strength, can compromise the material's ability to accommodate stress and deformation. This might explain the lower tensile strength of specimens exposed to wet-dry self-healing than that subjected to water-curing.

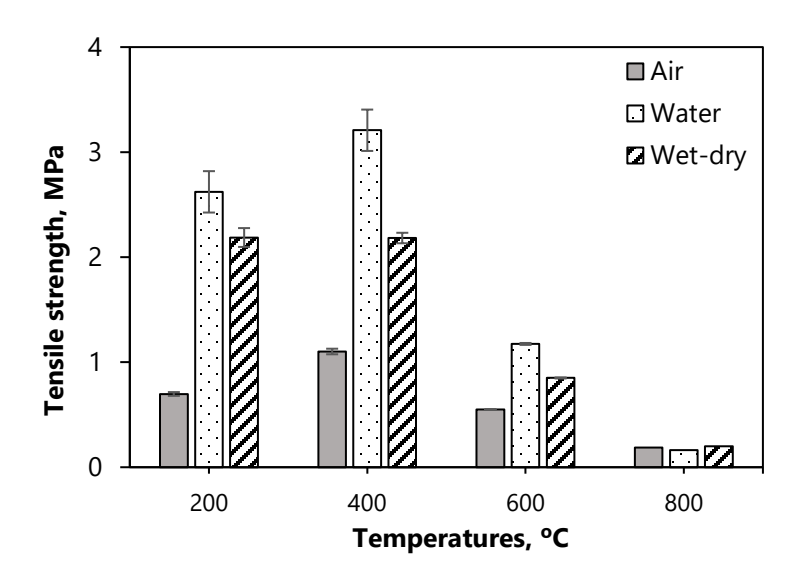


Fig. 5-4. Tensile strength of self-healed specimens (air, water, and wet-dry)

## **5.4.4 Permeability**

Permeability coefficient was calculated for triplicate specimens of each group (i.e. AAS-AC, AAS-WC, and AAS-CC) at different temperatures 200 °C to 800 °C. As shown in Fig. 5-5, specimens subjected to wet-dry self-healing scheme exhibited the lowest water permeability at all studied temperatures. At temperature 200 °C, the permeability coefficient of AAS-CC showed a reduction of approximately 67% of its counterpart AAS-AC specimen. Under the effect of wet-dry cycles, AAS-CC permeability was impeded by the newly formed self-healing products whether in the shape of microstructural densification or calcite precipitations [89]. Moreover, this permeability recovery was dependent to the damage inducing temperatures [35,101]. At temperature 600 °C, AAS-CC permeability was enhanced by approximately 88% of its counterpart AAS-AC. When deteriorating temperatures elevated from 200 °C to 600 °C, the pore connectivity into the matrix was amplified because of the exacerbated crack propagations related to the gradually increased dehydrations and microstructural decompositions [29]. This porous matrix promoted the diffusion

through which the ions were able to undergo into a chemical reaction to form more self-healing products [99]. Also, this wet-dry self-healed specimens revealed permeability performances better than water self-healed specimens AAS-WC. Permeability coefficient of AAS-CC decreased by approximately 5%, 13%, 18%, and 7%, lower than water post-fire cured specimens, at temperatures 200 °C, 400 °C, 600 °C, 800 °C, respectively. The inclusion of dry phase accelerated the geopolymerization reaction, generating a denser hydration product of Na-substituted C–S–H with low Ca/Si ratios, and finer pore size distribution [75].

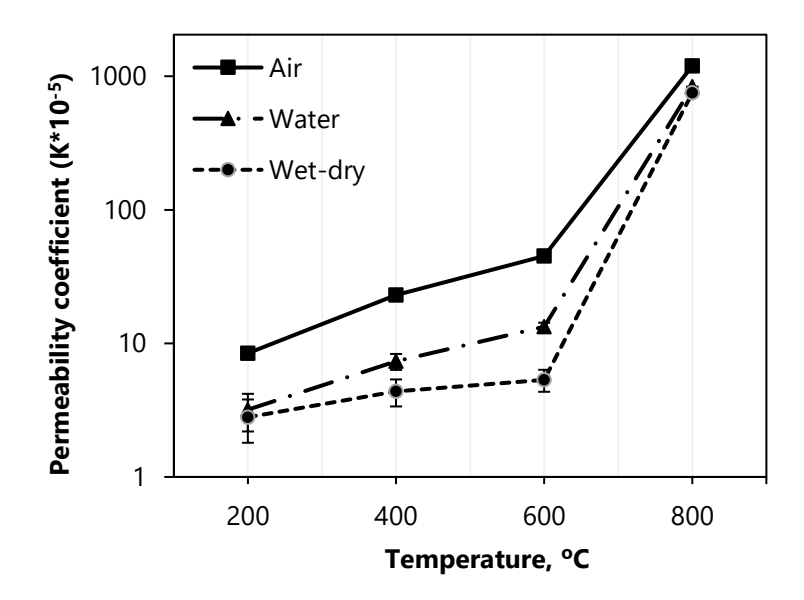


Fig. 5-5. Permeability coefficients of Air, Water, and Wet-dry self-healed specimens

## 5.4.5 Absorption and sorptivity

The capillary water absorption was measured on triplicate specimens of each self-healing conditioning scheme (i.e. air, water, and wet-dry). At temperatures 200 °C to 800 °C, specimens exposed to post-fire wet-dry cycles showed the lowest water absorption compared to the air-cured and water-cured specimens. For example, as shown in **Fig.** 5-6, the capillary absorption of AAS-CC decreased by 23%, 25%, 44%, and 27%, with respect to the corresponding AAS-AC specimens

at temperatures 200 °C, 400 °C, 600 °C, and 800 °C, respectively. This can be attributed to the cyclical nature of the wet-dry treatment, enhancing the self-healing process by promoting the rehydration of unreacted particles into the matrix in addition to encouraging a further precipitating of calcite crystals which block the capillary pores [95].

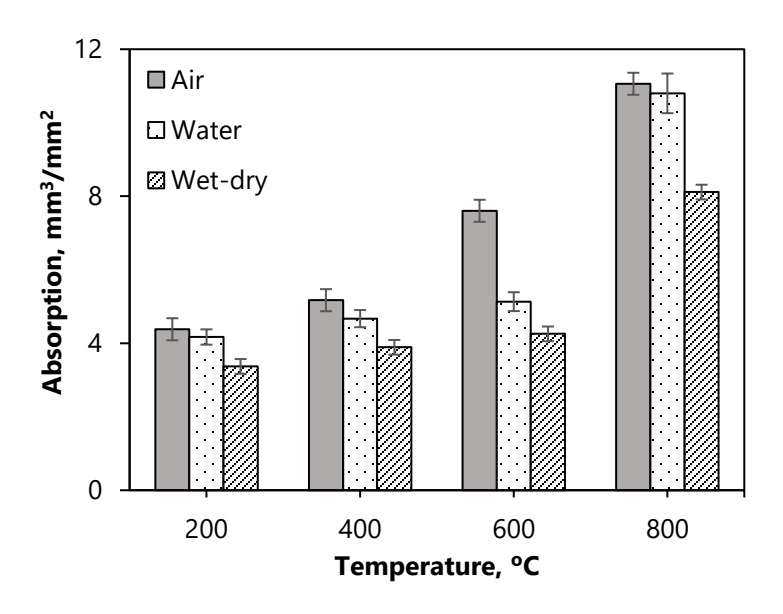
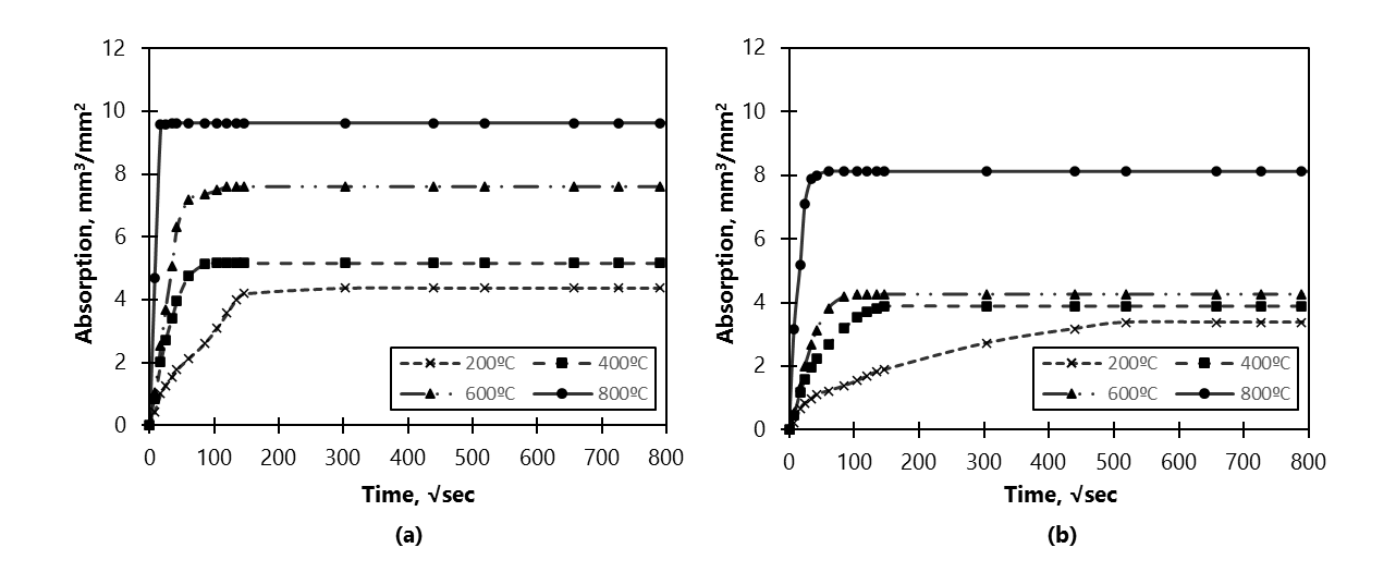


Fig. 5-6. Water absorption (mm<sup>3</sup>/mm<sup>2</sup>) for Air, Water, and Wet-dry post-fire curing schemes

To better understand the evolution of capillary pores, water absorption rates (mm³/mm²) were plotted versus time (√sec) for 6 days. As shown in **Fig.** 5-7, a comparison was carried out between specimens exposed to wet-dry cycles with identical specimens immersed in water. For exposure temperatures 200 °C to 800 °C, a significant reduction was observed on the rate at which the water ingresses into the AAS-CC matrix than AAS-WC. This can be ascribed to the more detected calcite precipitations under the effect of the enhanced ions diffusion due to the implemented wet-dry cycles [94].



**Fig. 5-7.** Differences in capillary water absorption rates between (a) Water self-healed specimens (b) Wet-dry self-healed specimens

### 5.4.6 XRD

XRD analysis was carried out on three separate sets of samples: AAS-AC, AAS-WC, and AAS-CC, as shown in **Fig.** 5-8. Self-healed specimens deteriorated under a temperature of 600 °C were specifically selected for the XRD testing, as they exhibited a complicit recovery as confirmed from compressive strength, tensile strength, permeability, and absorption tests. Consequently, post-fire curing under wet-dry cycles demonstrated multiple diffraction patterns reflecting either new crystal formation or alteration in existing phases. For instance, the main peak around 30° 2θ was attributed to calcium carbonate species CaCO<sub>3</sub>, extensively generated into the AAS-CC matrix because of its enhanced carbonation processes [65]. Highly diffracted intensity of wet-dry specimens confirmed its expanded crystallinity of CaCO<sub>3</sub> where induced cyclic nature was frequently promoting the matrix diffusion and precipitating more calcite crystals [60]. Furthermore, a new diffracted peak around 27° 2θ was also revealed. This crystalline pattern matched with a hydration product of N-

C-S-H (Na<sub>2</sub>O-CaO-SiO<sub>2</sub>-H<sub>2</sub>O). The initiation of this denser self-healing product with its lower Ca/Si ratios and finer particle size distribution was responsible for the enhanced mechanical and durability recovery of AAS-CC specimens [21].

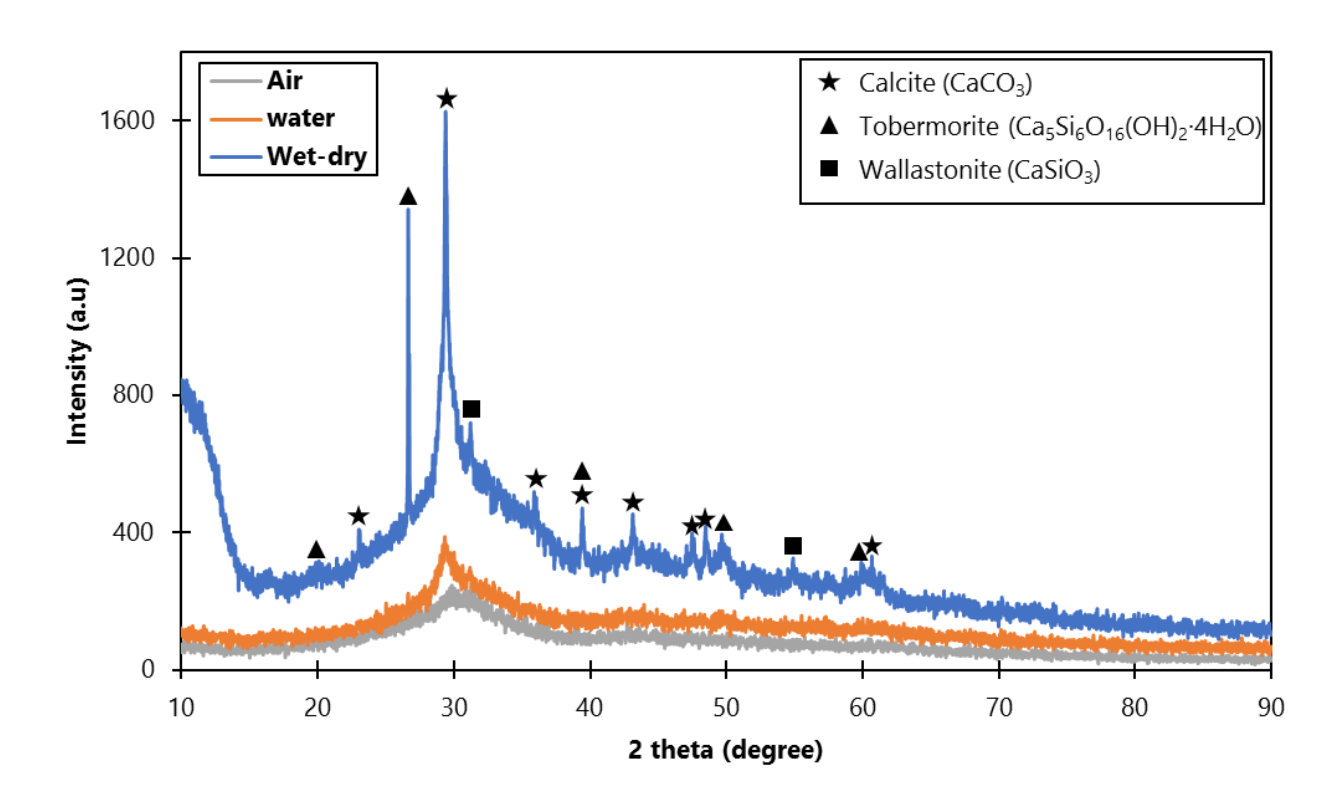


Fig. 5-8. XRD analysis for the fire-damaged 600 °C specimens, Air, Water, and Wet-dry schemes

### 5.4.7 Thermogravimetric analysis TGA

Thermogravimetric analysis (TGA) was performed to provide a quantitative characterization of AAS compositions upon exposure to different post-fire self-healing conditions (i.e. air, water, and wet-dry). According to the obtained results from XRD, identical powders were prepared to be analyzed under TGA. As shown in **Fig.** 5-9, TGA curves were plotted for the AAS-AC, AAS-WC, and AAS-CC, where the presence of C-A-S-H and hydrotalcite for all tested samples was confirmed at distinct percentages, in consistence with previous studies [76,77]. In general, the

weight loss in the range from 40°C to 100°C is ascribed mainly to the evaporable water, hence all measurements started from 100°C. Thereafter, up to 215°C, the weight loss is mostly due to the loss of bound water in C-A-S-H, and from 215°C to 400°C, is the result for the release of bound water from hydrotalcite [76]. While calcite decompositions were observed at temperatures 650 °C. However, at temperature 900 °C, microstructural decomposition of hydration product N-C-S-H was exhibited. As a result, wet-dry schemes showed an approximately 27% increasing in the calcite formation higher than other approaches (i.e. air and water). This can be attributed to the enhanced carbonation upon exposure to cyclic saturated and dehydrated phases [95]. Furthermore, identification of the new generated hydration product N-C-S-H was reflected by 18% weight loss of AAS-CC specimens. That was ascribed to the implementation of the curing temperature of 65 °C during the dry phase [21].

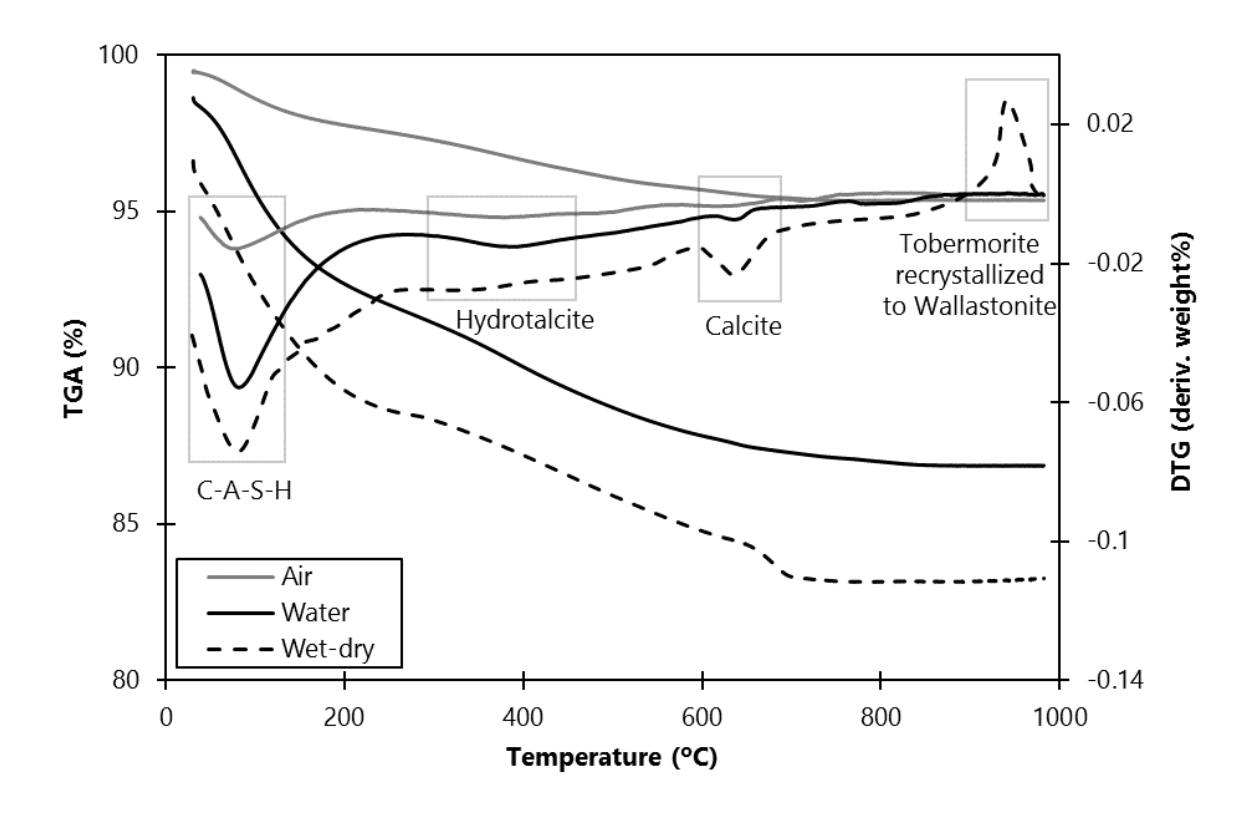


Fig. 5-9. TGA of the 600 °C fire-damaged specimens; AAS-AC, AAS-WC, and AAS-CC

#### 5.5 Discussion

Fig. 5-10 presents a schematic diagram for self-healing mechanisms revealed upon exposure to the studied post-fire wet-dry cycles. When fire-damaged AAS-CC specimens were initially subjected to the wet phase where the provided saturation condition promoted the diffusion, cations delivery was furtherly extended from high concentrated matrix to the lower concentrated cracks [60,65,99]. Additionally, a prolonged hydration of un-hydrated slag particles was triggered contributing to a microstructural densification through the reformation of main hydration product C-A-S-H [32]. During the subsequent dry phase where specimens were kept into an oven at temperature 65 °C, precipitations of calcium carbonate CaCO<sub>3</sub> crystals were expanded due to direct exposure to atmospheric carbon dioxide CO<sub>2</sub> [102]. Moreover, owing to heat implementation, a denser hydration product Na-substituted C-S-H with low Ca/Si ratios, and finer pore distributions, Na<sub>2</sub>O-CaO-SiO<sub>2</sub>-H<sub>2</sub>O (NCSH) was produced [75]. Therefore, the frequent wet-dry cycles had effectively induced multiple self-healing products, leading to a significant improvement either in mechanical properties or durability.

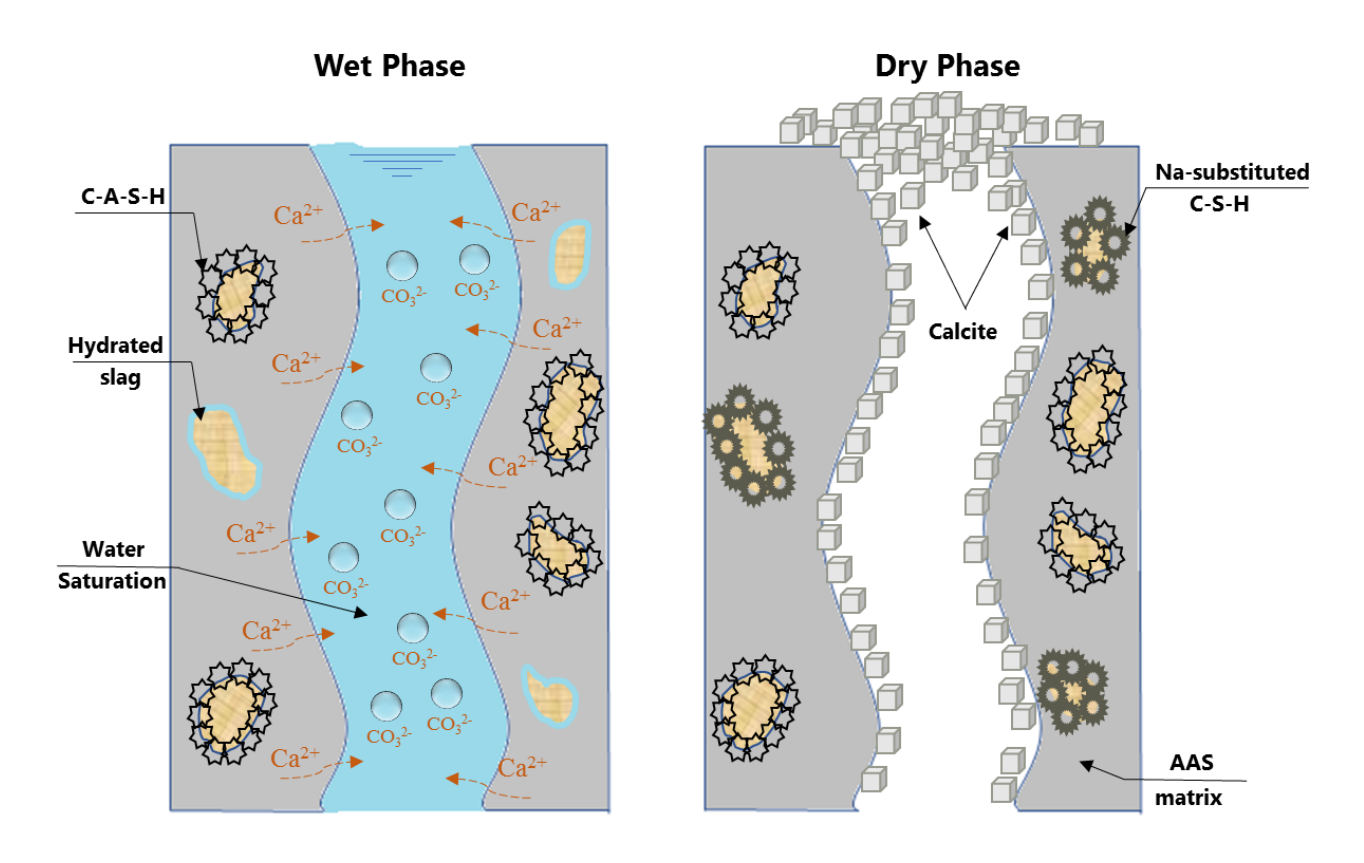


Fig. 5-10. Self-healing mechanism under the wet-dry cycles

#### **5.6 Conclusion**

The implementation of wet-dry cycles, as a post-fire self-healing approach of AAS, was investigated and compared with the air-cured and water-immersion-cured schemes. A comprehensive experimental program was carried out, where the following conclusion was drawn.

- 1- A significant enhancement in self-healing ability of alkali-activated slag materials subjected to post-fire wet-dry curing scheme compared to air and water cured alternatives.
- 2- Calcite precipitations CaCO<sub>3</sub> was revealed as the predominant self-healing product for wetdry self-healed specimens because of the enhanced carbonation due to its saturateddehydrated nature.

- 3- A newly formed hydration product was observed into specimens exposed to wet-dry cycles due to the implementation of the dry phase which supported the initiation of the Nasubstituted C-S-H
- 4- The obtained results advocate the implementation of AAS as a high resilient construction material that has the ability to be furtherly self-healed using different external self-healing schemes (i.e. wet-dry).
- 5- The environmental conditions reflected in the utilized wet-dry cycles in this study might be more effective than the theoretical and laboratory water immersion conditions.

## **Chapter 6: Microstructures and Healing Mechanism**

#### 6.1 Abstract

The self-healing property of construction materials, particularly in the context of alkali-activated materials (AAMs) that offering reduced CO<sub>2</sub> emissions and enhanced durability, represents a groundbreaking advancement in civil engineering and construction technology. This study explores the autogenous self-healing potential of alkali-activated slag (AAS) specifically following exposure to elevated temperatures up to 800 °C, a condition that poses significant challenges to the structural integrity and longevity of construction materials. Addressing these challenges, this research examines two post-fire curing methods: exposure to ambient air and immersion in sodium hydroxide (NaOH), to assess their effectiveness in promoting self-healing in AAS. Through a combination of visual inspection, ultrasonic pulse velocity, water sorptivity, rapid chloride permeability tests, scanning electron microscopy-energy dispersive X-ray, and X-ray diffraction, the mechanisms behind AAS's self-healing capabilities were dymistified. The selection of these methods is grounded in their ability to provide a comprehensive evaluation of crack healing, microstructural changes, and the durability of the treated materials. Our findings reveal that NaOH immersion significantly enhances self-healing, evidenced by reduced crack widths and improved material properties. The dominant healing product, calcium carbonate (CaCO<sub>3</sub>), precipitates through a combination of hydration reactions and carbonation processes, crucially contributing to the closure of microcracks and the restoration of the material's integrity. This process underscores the critical role of chemical reactions in AAS's self-healing mechanism, offering insights into its potential for enhancing the durability and resilience of construction materials. The broader significance of this research lies in its contribution to advancing sustainable construction practices by leveraging the self-healing properties of AAS to mitigate fire damage, thus extending the lifespan of concrete structures, and reducing maintenance costs.

#### 6.2 Introduction

In the pursuit of more sustainable construction practices, alkali-activated materials (AAMs) have emerged as a pivotal innovation. Distinct from ordinary Portland cement (OPC), AAMs are produced through the chemical activation of aluminosilicate precursors, such as blast furnace slag and fly ash, using alkaline solutions [17,103–107]. This process not only utilizes industrial by-products, thereby reducing landfill waste, but also significantly lowers CO<sub>2</sub> emissions associated with cement production [4,8,81,108,109]. The manufacturing of OPC is known to be energy-intensive, contributing to ~8% of global CO<sub>2</sub> emissions due to the calcination of limestone and the combustion of fossil fuels [110,111]. In contrast, the production of AAMs largely circumvents these energy-consuming processes, offering a greener alternative that aligns with the global agenda for carbon footprint reduction in the construction industry [112–114].

The chemical activation of aluminosilicate-rich materials in the production of AAMs leads to the formation of a three-dimensional network structure that significantly influences the material's mechanical and durability properties. The nature of the precursor materials plays a critical role in determining the composition and characteristics of this network [5]. Specifically, calcium-free and low-calcium precursors, such as fly ash, primarily result in the formation of zeolite-like gel (e.g., analcite (N-A-S-H), sodalite) [6]. These gels contribute to the material's mechanical strength and environmental resistance, although their performance can be sensitive to the specific conditions of the alkaline activation process. Conversely, calcium-rich precursors, such as blast furnace slag, lead to the predominance of calcium aluminum silicate hydrates (C-A-S-H) gel with a low Ca/Si

ratio [6,115]. Developing such high strength C-A-S-H endowed alkali-activated slag (AAS) with comparable mechanical and durability performances to OPC [18]. The presence of calcium in the precursor material facilitates the formation of this gel, which acts as the primary binding phase, contributing to the material's structural integrity and resistance to chemical attack. Several studies highlighted AAS's intrinsic resistance to physio-chemical deteriorations such as sulfate attacks and freeze-thaw cycles, among other severe exposure conditions [6,116,117].

Despite the high performance, AAS suffers from severe cracking and microstructural decomposition upon exposure to elevated temperatures [29]. Such damage reduces AAS load-carrying capacity and opens its microstructure for aggressive substance ingress and attack [118]. Thus, more comprehensive studies were conducted to understand AAS's chemical and morphological alterations upon exposure to elevated temperatures. Rovnaník *et al.* [29] studied the microstructural changes of AAS pastes after exposure to up to 1200 °C for 1h. From 20 °C to 575 °C, dehydration and partial decomposition of C-A-S-H were observed, reducing compressive strength. Between 600 and 800 °C, a complete decomposition of AAS microstructures was reported [119,120]. Above 800 °C, new phases start to crystallize (i.e., Akermanite), enhancing the mechanical properties [29]. This understanding of AAS's vulnerabilities at high temperatures underscores the need for innovative solutions to enhance the durability and longevity of concrete structures, paving the way for the exploration of self-healing technologies.

Generally, there are two types of self-healing: autonomous self-healing and autogenous self-healing. For the first one, unconventional engineered materials are embedded into the mixture during casting to plug cracks [30,121]. Hollow fibres, encapsulation, coatings, shape-memory materials, and bacteria are all different autonomic self-healing approaches used to enhance concrete's mechanical properties and durability [122–126]. For autogenous self-healing,

continuous hydration of the non-hydrated particles forms hydration products that heal cracks without manual interference [30,40]. Hence, autogenous self-healing is an inherent feature of cement-based binders, promoting damage recovery of concrete infrastructure [127]. For instance, the carbonation of surface-cracked concrete elements was reported to heal such cracks autogenously, partially and completely, by producing calcium carbonate CaCO<sub>3</sub> precipitations [128].

Edvardson et al. [129] investigated the process in details. They revealed that this calcite precipitation would have the appropriate conditions to be formed once the water access to the cracks where the calcium ions are available into the crack vicinity. These calcium ions would undergo into the chemical reactions and the calcite crystals would grow on the surface of the crack under the so-called "surface-controlled crystal growth". Then, under the consumption of calcium ions on the wall of the cracks, more calcium ions have to travel by means of diffusion from the inner matrix to the crack i.e., less rich as a source of Ca2+, under the so-called "diffusion-controlled crystal growth. Moreover, continuous hydration with time developes more hydration products which have a strength like that of the primary calcium silicate hydrate (C-S-H) gels and clearly superior to that of calcite precipitation products. This microstructure densification was clearly observed in the internal bulk cement past and on the crack face. Thus, it was emphasized that it highly contributes to the mechanical strength recovery [130]. The same was reported for the AAS composite [61,63]. Similar to OPC, further hydration, densifying AAS microstructures, and crystallization of CaCO<sub>3</sub> will have a healing effect. For example, Nguyễn et al. [33] investigated the morphology of self-healed AAS specimens. Results showed structural restoration through crack closure and mechanical recovery and identified CaCO<sub>3</sub>, C-(N)-A-S-H, and Na<sub>2</sub>CO<sub>3</sub> as the dominant self-healing products.

On the other hand, several studies showed that post-fire curing effectively boosts cement-based composite strength after exposure to elevated temperatures [131,132]. Previous work by Sarshar and Khoury [133] reported that the concrete exposed to 500 °C could recover 25 % of its post-fire compressive strength after curing at 100% relative humidity. Also, 72 h post-fire water curing for concrete specimens exposed to 400 °C, 500 °C, and 600 °C induced an increase in the residual strength with 20%, 35%, and 40% with respect to non-post-fire cured specimens, respectively [134]. Moreover, Poon *et al.* [93] revealed up to 85% and 93% recovery in the original strength for normal and high-strength concrete specimens exposed to 600 °C upon 28 days post-fire water curing, respectively. Furthermore, post-fire air curing was also identified as an effective recovery approach due to its high carbonation potential [135–137]. However, post-fire water-curing resulted in higher mechanical recovery and denser pores than post-fire air-curing for OPC concrete specimens [138]. This highlights cement-based material self-healing capability under post-fire curing by generating new healing products in the form of hydration components (e.g., C-S-H) and precipitations (e.g., calcite) to close cracks and overcome internal defects [139–141].

### 6.3 Research Significance

Previous research revealed that post-fire curing would improve the potential of autogenous self-healing in cementitious materials enhancing the crack closure and restoring the structural integrity after fire exposure. However, the effect of post-fire curing on AAS after exposure to elevated temperature is still not well addressed in the literature. Hence, this study will focus on providing a fundamental understanding of AAS self-healing performance, including microstructural investigation, to bridge the existing knowledge gap. Moreover, this research is advocating the high resilience of AAS under harsh conditions.

#### 6.4 Materials and methods

#### 6.4.1 Materials

A ground granulated blast furnace slag (GGBFS) with a specific gravity of 2.92 g/cm<sup>3</sup>, a Blaine fineness of 515 m<sup>2</sup>/kg, and an average particle size of 15 µm was used as the main precursor to produce the AAS paste and concrete specimens. The GGBFS was sourced from Lafarge, located in Canada. This material conforms to the ASTM C989 [97] ensuring its quality and consistency for the intended applications in this study. Its chemical composition is shown in **Table** 6-1. A mix of sodium hydroxide (NaOH) solution and sodium silicate (Na<sub>2</sub>SiO<sub>3</sub>) solution was used as the alkali activator. Sodium hydroxide pellets with 99.9% purity were dissolved in water, and then the solution was left for 24-h at room temperature to cool down. For this, a commercial sodium silicate solution (28.8% of SiO<sub>2</sub>, 9.01% of Na<sub>2</sub>O, 62.2% of H<sub>2</sub>O) was mixed with NaOH solution to produce the desired activator with silicate modulus (M<sub>S</sub> = SiO<sub>2</sub>/Na<sub>2</sub>O) of 1.25, and Na<sub>2</sub>O of 6 wt.% of the binder. Riverside sand with a fineness modulus of 2.70, a specific gravity of 2.61, and water absorption of 2.73% was used as fine aggregates (FA), meeting the ASTM C778 for standard sand [98]. It was provided by a local producer, ensuring the material's uniformity and suitability for use in concrete mixtures. The used coarse aggregate (CA) was crushed stone with 2.70 specific gravity, 1.3% water absorption, and a nominal maximum size of 9.5 mm, in accordance with the ASTM D692 for coarse aggregate in concrete [142].

Table 6-1 Chemical composition of the used GGBFS

Constituents	SiO <sub>2</sub>	Al <sub>2</sub> O <sub>3</sub>	CaO	MgO	K <sub>2</sub> O	Na <sub>2</sub> O	Fe <sub>2</sub> O <sub>3</sub>	SO <sub>3</sub>
Percentage %	36.1	10.4	37.1	13.3	0.40	0.42	0.67	1.61

## 6.4.2 Experimental Design

Fig. 6-1 presents a flow chart illustrating the entire experimental program followed in this study.

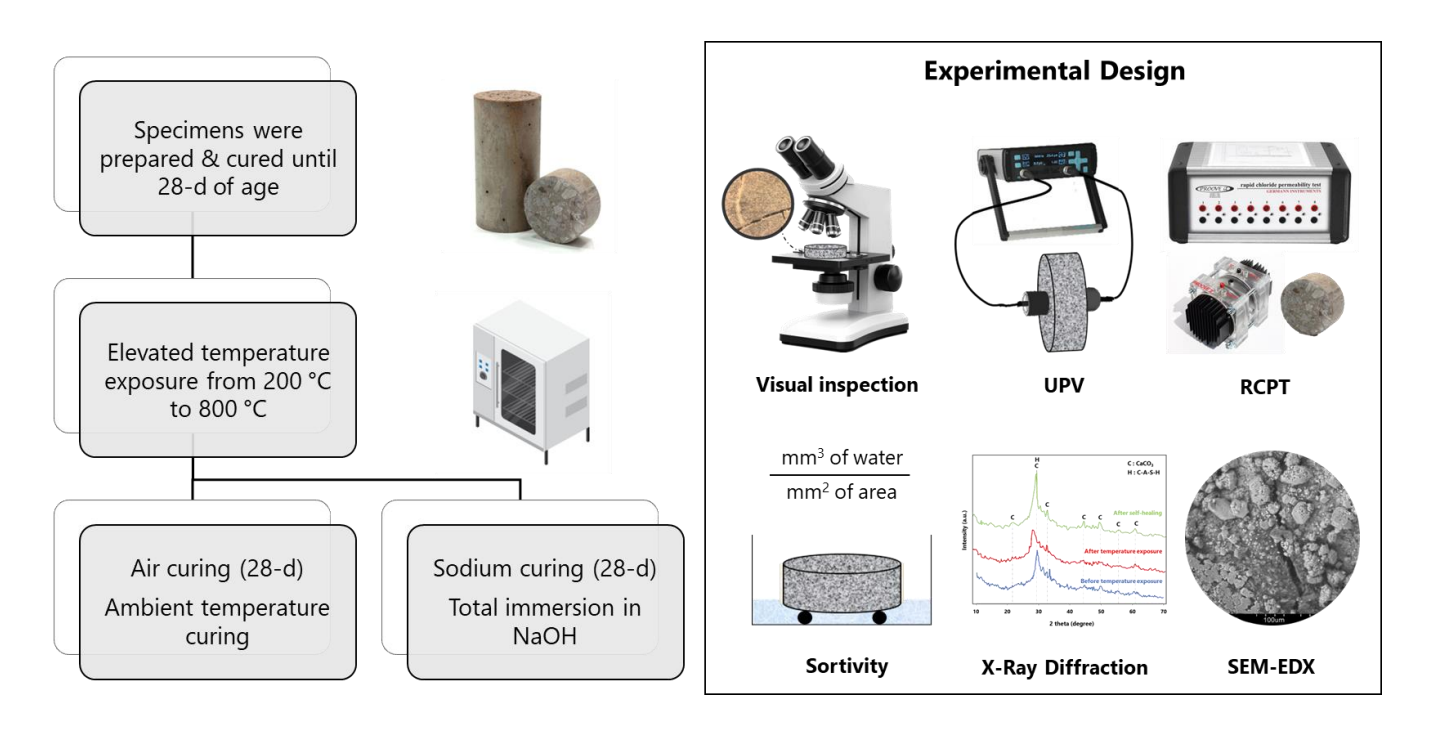


Fig. 6-1 Flow chart for the experimental program

# 6.4.3 Mixture proportioning

Based on a previous study from our laboratory [117], a concrete mixture with a binder content of 400 kg/m<sup>3</sup>, a water-to-binder (*w/b*) ratio of 0.44 (including water from the activator), and a FA-to-CA ratio of 1:1.75 was adopted (**Table** 6-2). Concrete mixtures were prepared and cast according to the ASTM C192 standard [143]. Following the mixing sequence reported by Abubakr and Soliman [144], dry aggregate and the binder were initially mixed for 1 min; then, the activator solution was added and mixed for 3 additional minutes. Cylindrical concrete specimens with a diameter of 100 mm and a height of 200 mm were cast and compacted on a vibrating table. After 24-h, all specimens were demolded and stored in sealed bags at the laboratory ambient

temperature  $23 \pm 1$  °C until the day of testing. For microstructure and mineralogical analyses, paste samples were prepared under identical conditions to those in concrete specimens (i.e., curing, temperatures exposure, healing scheme).

**Table 6-2** Mix proportioning of the studied AAS concrete

Samples	Ms	Dosage		Post-exposure					
Samples	1018	Na <sub>2</sub> O%	Binder	FA	CA	NaOH	Na <sub>2</sub> SiO <sub>3</sub>	Water*	curing scheme
NC-AAS	1.25	6%	400	656	1148	19	104	111	NaOH
AC-AAS	1.25	6%	400	656	1148	19	104	111	Air

<sup>\*</sup>The weight of water in the mix design includes the water into the activator solution.

#### **6.4.4 Elevated Temperature Exposure**

At 28 days of age, specimens were subjected to various elevated temperatures starting from 200 °C up to 800 °C. The selected temperature range was selected as they can represent the dehydration and major microstructural alterations. For instance, from 200°C to 600°C, dehydration and partial microstructural decomposition were exhibited, however, from 600°C to 800°C, a complete decomposition for the AAS hydration products was accomplished. There was no need to go beyond the 800 °C as there is a huge failure in the mechanical properties [29]. An electrical heating furnace was used, where the specimens were heated up at an increasing rate of 5–10 °C/min, according to the standard ASTM E831 [145], until reaching the targeted temperature, which was maintained for 1h, followed by naturally cooling down at ambient temperature inside the furnace [146]. To ensure that the specimen core reached the targeted temperature, the temperature at the center of a dummy specimen was monitored using a thermocouple type K. Specimen's temperature, along with the oven temperature, was continuously monitored and recorded using a data acquisition system.

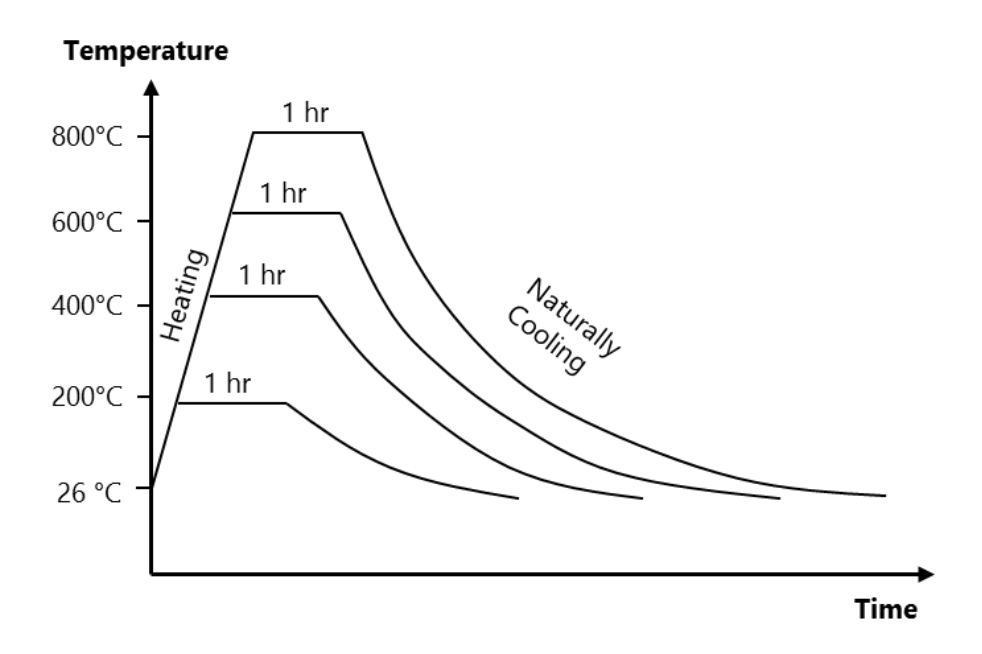


Fig. 6-2 Heat profile

# 6.4.5 Self-healing Study

After the elevated temperature exposure, specimens were divided into two groups depending on the following curing regime: air-cured samples (AC-AAS) and NaOH-cured specimens (NC-AAS). The latter were immersed in the conditioning solution (i.e., 2M NaOH) for 28 days. At the same time, AC-AAS specimens were kept at uncontrolled ambient temperature in the laboratory. NC-AAS scheme was applied to trigger the un-hydrated particles to react with the activator solution (dissolution + polycondensation). Moreover, improving the diffusion into the matrix could be supported under the applied saturation condition. It should be mentioned that the 2M NaOH conditioning solution was used to reduce alkali leaching from the specimens as its concentration was lower than the original existing. Thus, continued reaction from the remaining original activating solution was encouraged to enable the self-healing [35]. After 28-d of curing (56-d of age), both groups' specimens were tested to quantify the effect of the applied post-fire curing

schemes on the potential of autogenous self-healing. In order to quantify the autogenous self-healing, the damage was initially assessed relative to the reference specimens (i.e., not exposed to fire) to reveal the residual properties of AAS specimens after elevated temperature deteriorations using Eq. 8 [147]. Subsequently, following the implementation of post-fire self-healing schemes, the self-healing was evaluated based on the differences between the damages before and after the post-fire curing [148], as shown in Eq. 9. Furthermore, the recovery of the post-fire cured specimens was determined by comparing them to the reference specimens as described in Eq. 10 [93]. Error! Reference source not found. illustrates the self-healing quantification process f ollowed. The quantification methodology will rely on ultrasonic pulse velocity (UPV), sorptivity, and the rapid chloride permeability (RCPT) [31,149,150], to investigate whether the applied scheme would have the potential to produce self-healing products, densifying the AAS microstructures as well as promoting the crack closure.

Damage 
$$\% = \frac{After elevated temperature exposure - Reference}{Reference} \times 100$$
 (8)

$$Self - healing \% = \frac{After self healing - After elevated temperatures exposure}{Reference} \times 100$$
 (9)

Recovery 
$$\% = \frac{After self healing - Reference}{Reference} \times 100$$
 (10)

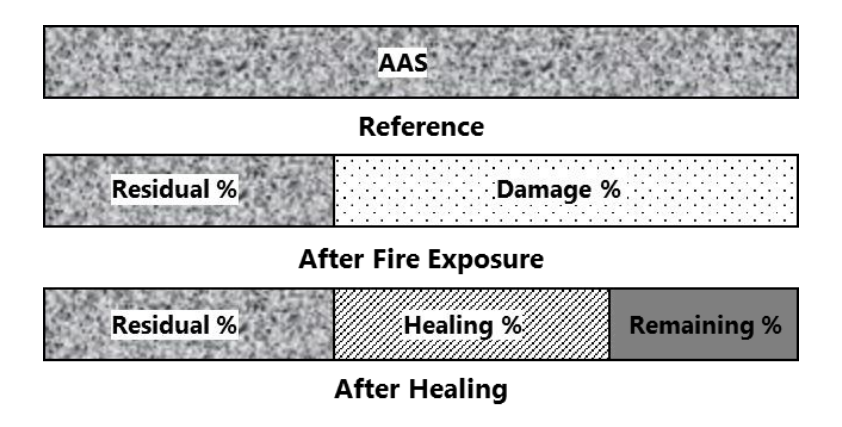


Fig. 6-3 Schematic diagram for the self-healing quantification process

# **6.4.6 Testing Methods**

To comprehensively evaluate the self-healing capabilities of AAS subjected to post-fire curing, a combination of methods was employed, each selected for its proven effectiveness in assessing specific aspects of material recovery and integrity restoration. Visual inspection offers a direct, initial assessment of surface crack sealing and closure, serving as a qualitative indicator of self-healing. It provides immediate, visible evidence of the healing process, which is essential for preliminary evaluation. Self-healing was monitored by examining the differences between the openings of the surface cracks for NC-AAS and AC-AAS specimens using a Motic 40x optical microscope [151]. The UPV testing was chosen for its ability to quantitatively measure changes in the material's density and homogeneity, which are indicative of internal crack healing. It enables the detection of variations in the velocity of ultrasonic pulses, reflecting improvements in the microstructural integrity due to self-healing. It was tested following the ASTM C597 [152] standard to determine variations in the density of microstructures and detect the alteration of internal defects (i.e., microcracks) before and after self-healing [149]. As the exposure temperature increases, dehydration and microstructural decomposition were progressively exacerbated [29].

Thus, crack propagations could subsequently heighten, decreasing the UPV velocities. However, after self-healing, the higher intensity of microstructures, due to further hydration and crystal formation, would have increased the UPV values [149,153]. Water sorptivity assesses the material's capacity to absorb water through capillary action, which decreases as self-healing products seal cracks and pores. A reduction in water sorptivity is a key indicator of effective self-healing, particularly in terms of enhanced durability against moisture ingress [31]. The test was performed according to the ASTM C1585 standard [154] on triplicate cylindrical specimens with a diameter of 100 mm and a thickness of 50 mm. The capillary absorption (I) and the sorptivity index  $(S_I)$ were calculated and considered to assess the rate at which water permeates. Given the significance of chloride ion resistance for the longevity of concrete structures, especially in aggressive environments, RCPT was employed according to the ASTM C1202 standard [155] to evaluate the impact of self-healing on improving the material's resistance to chloride ion penetration. It should be mentioned that there is a debate on the feasibility of RCPT results for AAS as the measured values are usually higher than the normal values due to the high level of ions, such as Na<sup>+</sup> and OH<sup>-</sup> , in the matrix due to the high alkalinity solutions [156–158]. Nevertheless, other researchers validated the potential of utilizing the RCPT with AAS for comparative analysis purposes [159]. A scanning electron microscope and energy dispersive x-ray tests (SEM-EDX) were performed for the microstructure analyses using Phenom ProX Scanning Electron Microscope with EDX capability. The X-ray diffraction (XRD) was performed using a Bruker D8 advance diffractometer (CuK $\alpha$  radiation, 1.5406 Å) with an im aging plate detector to collect data in a range of  $10^{\circ}-70^{\circ}$  20. Morphological and microstructural compositions of post-fire cured AAS specimens were examined to determine the formed healing products (e.g., hydration products, crystals, etc.) [69,70]. The XRD test was conducted to evaluate the self-healing potential by analyzing AAS specimens' crystalline structure and phase composition [160].

## 6.5 Results and discussion

## 6.5.1 Visual inspection

Surface cracks were examined for both NC-AAS and AC-AAS specimens using the optical microscope. High white precipitations filling the crack surface of the NC-AAS specimens were observed, as illustrated in **Fig.** 6-4. These CaCO<sub>3</sub> crystals in the form of calcite precipitations were intensively formed close to the cracks' openings. This can be ascribed to the absorption of atmospheric CO<sub>2</sub> into the NaOH aqueous solution [161], where Na<sup>+</sup> and OH<sup>-</sup> are almost entirely ionized in pure water because NaOH is very strongly alkaline. Subsequently, CO<sub>2</sub> reacts with OH<sup>-</sup> generating HCO<sub>3</sub><sup>-</sup> and CO<sub>3</sub><sup>2-</sup>, as shown in **Eq. 11** and **Eq. 12** [162]. This CO<sub>3</sub><sup>2-</sup> will react with the calcium ions Ca<sup>2+</sup> present in the AAS matrix, forming CaCO<sub>3</sub> [74]. On the contrary, for the AC-AAS specimens, no precipitations or healing products were detected in the cracks.

$$CO_2(aq) + OH^-(aq) \rightleftharpoons HCO_3^-(aq) \tag{11}$$

$$HCO_3^-(aq) + OH^-(aq) \rightleftharpoons H_2O + CO_3^{2-}(aq)$$
 (12)

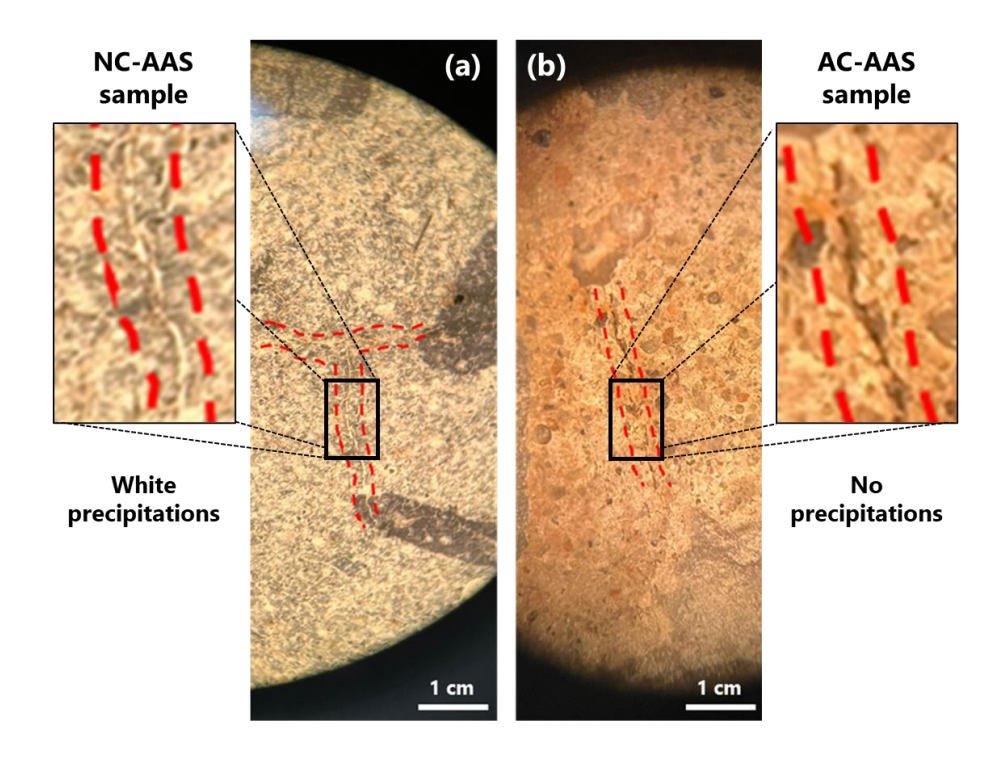


Fig. 6-4 Cracks observations for a) NC-AAS sample b) AC-AAS sample after 600 °C

Furthermore, AAS crack's closure was revealed to be related to its initial width. Cracks with widths lower than 50  $\mu$ m were completely closed by the calcite precipitations. Surface crack widths ranging from 50  $\mu$ m to 150  $\mu$ m were partially closed. Moreover, crack widths greater than 150  $\mu$ m showed the lowest healing ability, as shown in **Fig.** 6-5. Those observations are in agreement with the previous values reported in the literature [31,32]. It was emphasized that the lower the crack width, the more sufficient the formed self-healing products. For instance, when the initial crack width is 50  $\mu$ m, the diffused ions which later undergo into the chemical reaction to form the calcite precipitations would be enough to close the cracks. However, the intensity of self-healing products would not be enough to close the higher crack widths.

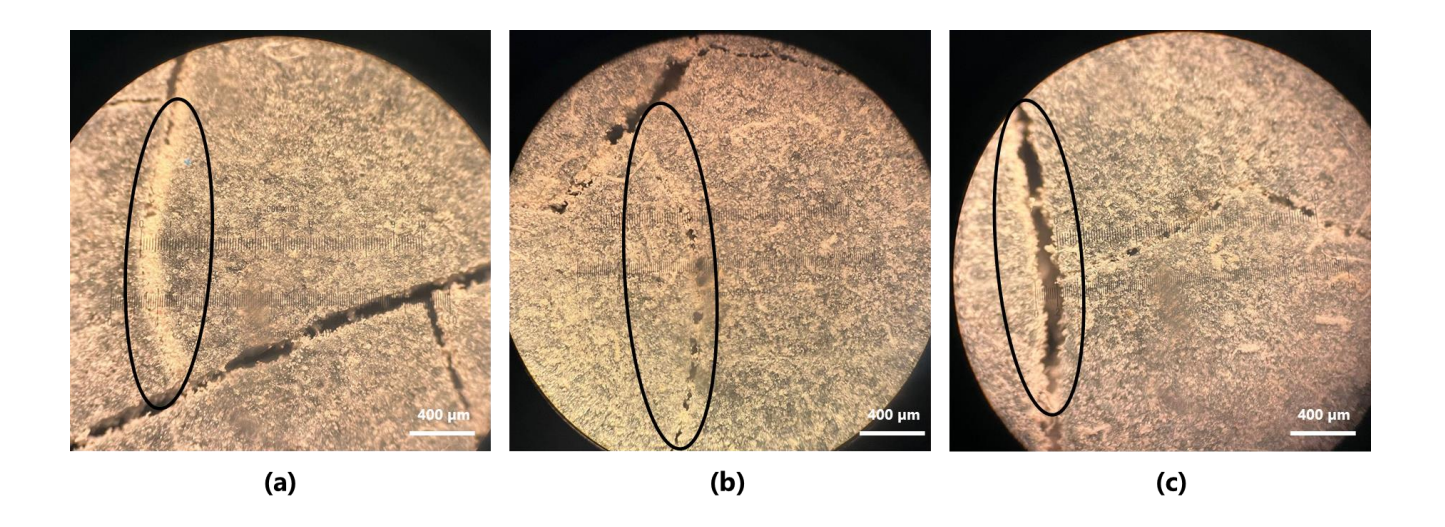
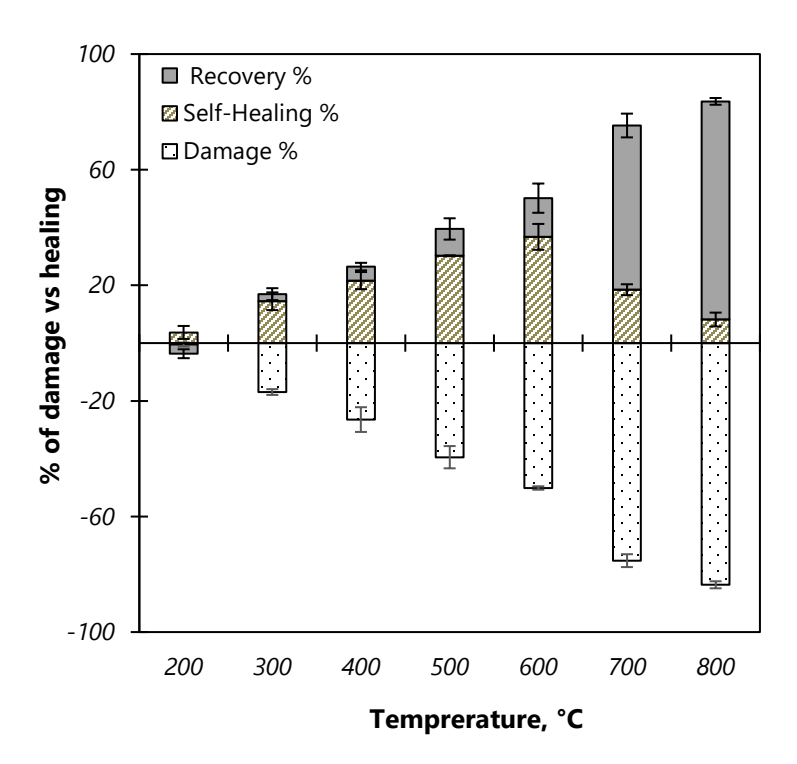


Fig. 6-5 Cracks observations for a) cracks less than 50 μm, b) cracks in range of 50–150 μm, c) cracks more than 150 μm

## 6.5.2 Quantification of self-healing using the UPV method

The percentages of damage, self-healing, and recovery at temperatures (200–800 °C) were evaluated using UPV as described previously (i.e., **Eqs. 1–3**). As shown in **Fig.** 6-6, damage and self-healing percentages exhibited relatively increasing trends as the exposure temperature increased. For instance, as the exposure temperatures increased from 200 °C to 600 °C, the percentage of damage increased from 0% to 54.7%. This can be attributed to the dehydration and partial decomposition of AAS microstructures [29], which escalate the crack propagation and decrease UPV velocities[149]. Similarly, self-healing percentage increased from 3.7% at 200 °C to 38.4% at 600 °C. This can be ascribed to amplification of permeability and pores interconnectivity with the severity of damage [99]. This significantly eases the penetration of the NaOH aqueous solution into the matrix. Thus, more un-hydrated slag particles would be reachable, leading to more microstructural densification and the formation of more hydration products [163]. Moreover, ion diffusion into the permeable matrix will be easier, encouraging more free cations to go from the

high concentrations' matrix to the lower concentrations' cracks [41,42,158]. Accordingly, more crystals and healing products would be formed, filling up the cracks (e.g., CaCO<sub>3</sub>) [164]. Those synergetic mechanisms significantly improve UPV velocities due to the densification of the microstructure [153]. These results agree with previous findings pointing to permeability and interconnected pores as key factors in controlling the extent of autogenous self-healing [99,164].



**Fig. 6-6** Comparative analysis between percentage of damage and self-healing percentage at different exposure temperatures.

Conversely, for specimens exposed to 800 °C, the complete decomposition of microstructures resulted in wider cracks [29], diminishing the self-healing effect and achieving a percentage of damage above 80%, as shown in **Fig.** 6-6. Moreover, at the exposure temperature of 800°C, amorphous phases start to crystalize where Akermanite was revealed as the dominant crystal phase. Thus, the extremely low intensity of the amorphous phases after exposure to 800°C significantly

affects the extent of self-healing [29]. Although the percentage of self-healing increased with the severer percentage of damage (up to 600 °C), the AAS full recovery is reversely proportional with this increased damage percentage (**Fig.** 6-6). This is attributed to the reduction in self-healing effectiveness as a recovering technique as the percentage of damage increased. In other words, the increasing rate of damage is much higher than the ability of self-healing to restore the integrity and bridge the cracks within 28-d of treatment. This result complies with previous research [35].

# **6.5.3 Water Sorptivity**

Fig. 6-7 shows the results of capillary water absorption of NC-AAS and AC-AAS specimens at different exposure temperatures from 200 °C to 800 °C. The capillary absorption rates (mm³/mm²) were plotted versus time (√sec) for 6 days. NC-AAS specimens exhibited a very low capillary water absorption compared to the AC-AAS specimens. For instance, the capillary water absorption was 2.99 mm³/mm² and 1.59 mm³/mm² at exposure temperature 200 °C, and 8.77 mm³/mm² and 6.86 mm³/mm² at exposure temperature 800 °C for AC-ASS and NC-ASS, respectively. This can be attributed to the microstructural densification as well as the formation of self-healing crystals in the NC-AAS compared to AC-AAS, highlighting the activation effect of the 2M NaOH conditioning solution. Therefore, the formed self-healing products impeded the water ingression into the matrix due to reduced cracks' widths [31].

Furthermore, the water sorptivity index for both NC-AAS and AC-AAS specimens were depicted in accordance with the exposure temperatures from 200 °C to 800 °C. Water sorptivity index can be estimated using the initial absorption (for the first 6 hrs.). However, as shown in **Fig.** 6-8, owing to the rapid initial absorption rate of the AC-AAS specimens induced due to the high intensity of cracks, the sorptivity index was evaluated for the first 1-h [165], for both group specimens. Also,

the high instant absorption of the NC-AAS and AC-AAS specimens exposed to 800 °C exposure made it difficult to evaluate their sorptivity index. As shown in **Fig.** 6-8, distinct reductions in water sorptivity index were revealed in NC-AAS specimens rather than AC-AAS specimens. For example, the water sorptivity index decreased from  $1.58 \times 10^{-2}$  and  $9.88 \times 10^{-2}$  mm/sec in the AC-AAS to  $0.44 \times 10^{-2}$  and  $3.70 \times 10^{-2}$  mm/sec in the NC-AAS for exposure temperature 200 °C and 700 °C, respectively. Moreover, sorptivity index reductions for exposure temperatures 300 °C, 400 °C, 500 °C, and 600 °C, were listed as shown in **Table** 6-3. The microstructural densification and surface crystals which were intensively observed in the NC-AAS specimens would impede the capillary water absorption and subsequently reduce the water sorptivity. These results were in accordance with the research [31].

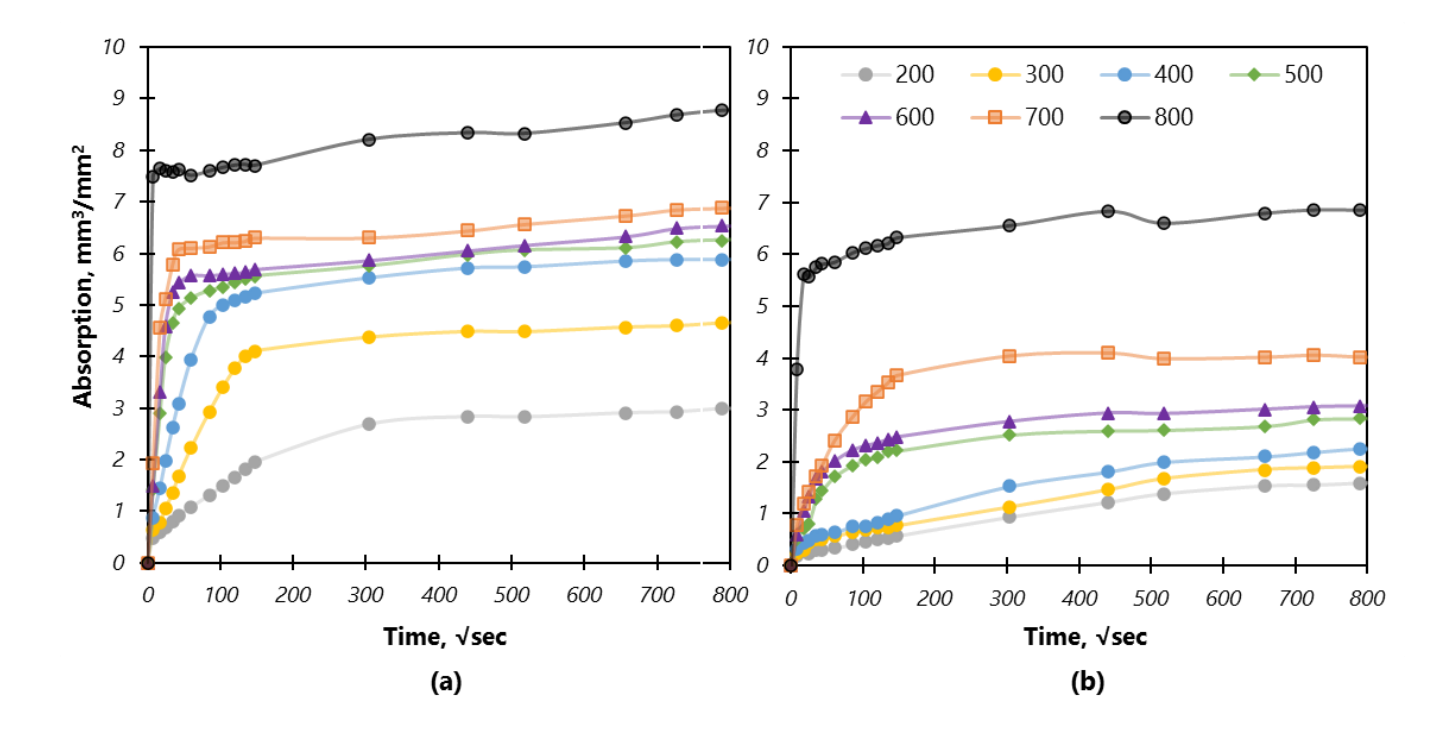
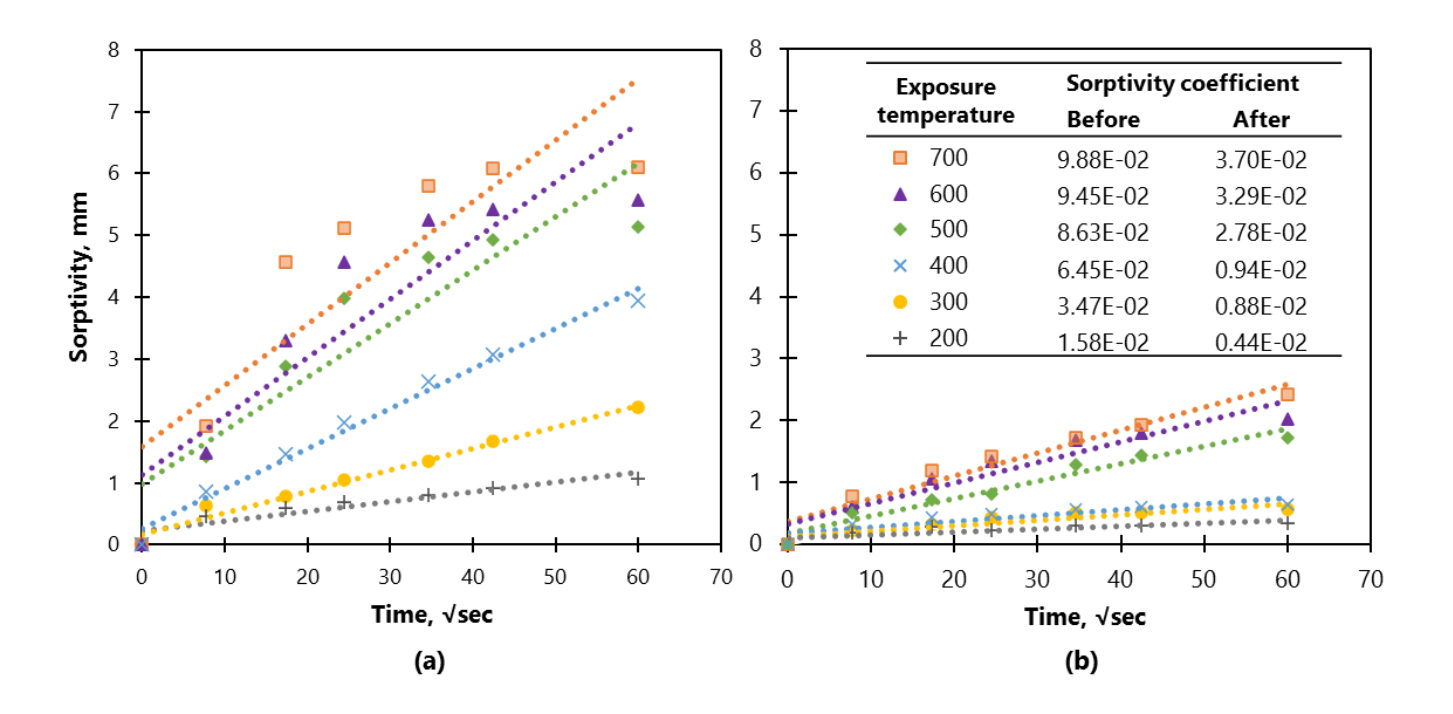


Fig. 6-7 Capillary absorption after elevated temperatures exposure for (a) AC-AAS specimens (b)



**Fig. 6-8** Water sorptivity (mm/√sec) after elevated temperature exposure for (a) AC-AAS specimens (b) NC-AAS specimens.

Table 6-3 Sorptivity coefficient

Exposure temperature	200°C	300°C	400°C	500°C	600°C	700°C	
Sorptivity	Before	1.58	3.47	6.45	8.63	9.45	9.88
coefficient(mm/√sec)×10 <sup>-2</sup>	After	0.44	0.88	0.94	2.78	3.29	3.70

Relying on the water absorption results, the correlation between the percentage of self-healing (Eq.

2) and the exposure temperatures was identified as illustrated in Fig. 6-9. As exposure temperatures increased from 200 °C to 600 °C, the percentage of self-healing subsequently increased. Surprisingly, their recovery percentages exceeded the initial damage percentages, exhibiting lower absorption than the reference specimens (i.e., not exposed to fire). This can be attributed to the severe damage induced into the matrix due to the increased exposure temperatures. This damage

facilitated the diffusion of more Ca<sup>2+</sup> to the surface of these fire-damaged specimens. This consequently improved the formation of more calcite precipitations (i.e., CaCO<sub>3</sub>), limiting the surface capillary pores due to the robust surface sealing effects [31]. Although the results of capillary water absorption and water sorptivity index showed that the self-healing percentage is directly proportional to the increased exposure temperatures; however, the total recovery (**Eq. 3**) has a reversely proportional correlation with the exposure temperatures (similar to UPV results) (**Fig.** 6-9). This highlighted the competition between two compensating mechanisms: recovery due to self-healing and weakening due to damage induced by the elevated temperatures.

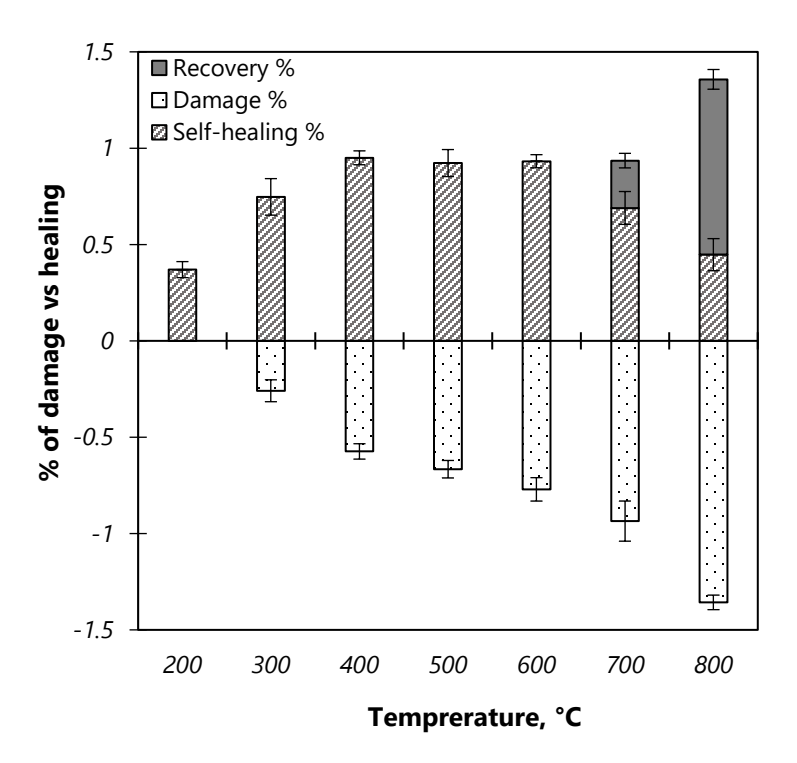


Fig. 6-9 Percentage of self-healing versus the remaining percentage to achieve the full recovery.

Interestingly, the self-healing percentage obtained from the water absorption test was higher than that from the UPV test. **Fig.** 6-10 illustrates the anticipated reasons advocating the mechanism of autogenous self-healing. Specimens submerged into the conditioning solution experienced a dual

effect: calcium ions would diffuse from the matrix to the crack, forming calcite precipitations and further hydration of the unreacted slag. However, as the carbonization reaction is faster than the hydration reaction [166], calcite precipitation will impede the penetrability of the solution into the matrix [31]. Also, Ismail *et al.* [41,42] studied the effect of the formed self-healing products on the matrix diffusion, where they revealed that diffusion start to occur at a slower rate due to the formed self-healing products when the crack widths were 80-100 µm. Moreover, no diffusion was exhibited when the crack width was less than 30 µm. This impeded diffusion will affect the delivery of cations to initiate the further hydration reaction. Thus, calcite precipitation was the dominant self-healing product rather than the microstructures.

The CaCO<sub>3</sub> tends to become concentrated at the crack mouths to obstruct the diffusion of ions into the deeper regions of the cracks. This is one of the primary factors causing the lack of a dense matrix and reducing the mechanical recovery. The chemical reaction between calcium ions Ca<sup>2+</sup> (leakage from C-A-S-H) and carbonate ions CO<sub>3</sub><sup>2-</sup>, produced CaCO<sub>3</sub> in the form of calcite that precipitates at the crack mouth [31].

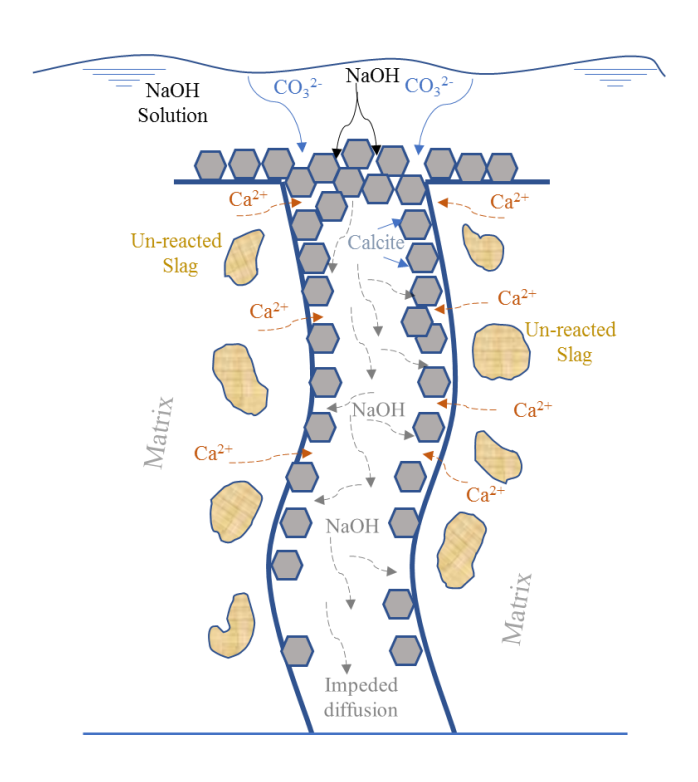
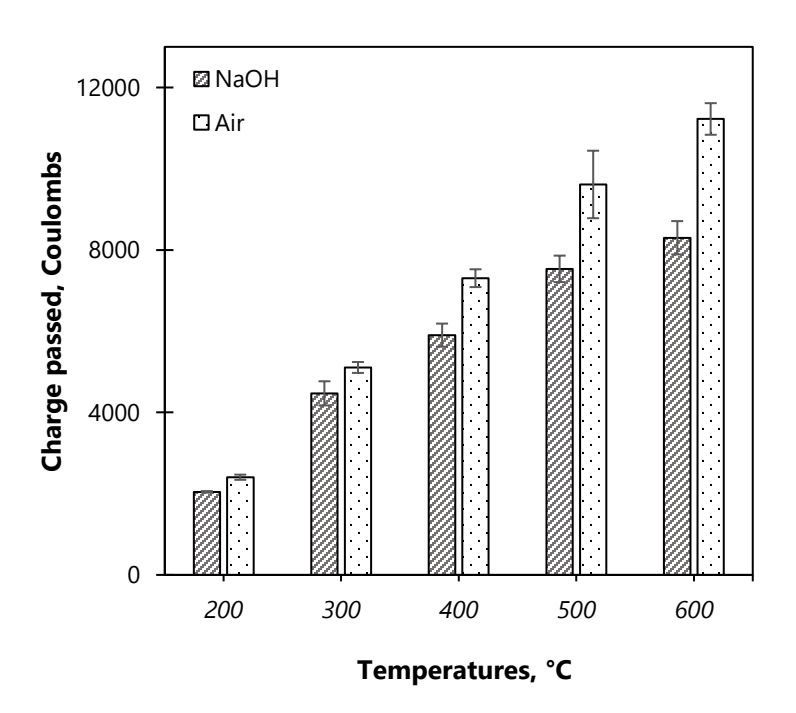


Fig. 6-10 Autogenous self-healing mechanism for AAS

# **6.5.4 RCPT Analyzes**

As shown in **Fig.** 6-11, the total charge passed into NC-AAS and AC-AAS specimens has notably increased (i.e., chloride ions penetration resistance has declined) when the exposure temperatures increased from 200 °C to 600 °C. This can be attributed to the high connectivity of the pore structure, owing to the higher intensity of cracks induced by the exposure to elevated temperatures [167]. The higher the connected pores, the higher the chloride ion migration [168–171]. This observed increase in chloride ion migration, associated with higher exposure temperatures, might compromise the long-term durability of AAS by accelerating corrosion processes and potentially affecting structural integrity [172]. It should be mentioned that specimens exposed to 700 °C and 800 °C have exceeded the limits of the RCPT device. The post-fire treatment for AAS samples by 2M NaOH resulted in more hydration formation, filling pores and healing cracks. This explains the

low RCPT results exhibited by the NC-AAS compared to AC-AAS. For instance, the total charges passed in the NC-AAS specimens were 15% and 28% lower than that of the AC-AAS specimens for exposure temperatures 200 °C and 600 °C, respectively. This revealed the NC-AAS high resistance to the chloride ions penetration due to the less penetrability of its pores' structure and densification of its microstructural as well as crystallization of self-healing products. This would promote the concept that applying the 2M NaOH conditioning solution for the AAS after elevated temperatures exposure will improve the self-healing potential.



**Fig. 6-11** The total charge passed for NC-AAS and AC-AAS specimens at different exposure temperatures (200 °C-600 °C).

One interesting point is that the healing effect of post-fire treatment varied according to the exposed temperature. As indicated in **Eq. 1**, the percentage of damage was estimated using the variances in RCPT values of the AAS specimens (before/after) exposure to elevated temperatures. Similarly,

the percentage of self-healing was assessed using the difference in RCPT values (before/after) post-fire curing, as shown in **Eq. 2**. As more chloride ions migrated into the specimens upon the increase of the exposure temperature, the percentage of damage increased. Whereas the increasing self-healing percentages due to the higher impedance of chloride ions migration prevailed at temperatures 200 °C to 600 °C. For example, NC-AAS specimens exhibited a self-healing percentage of 18% and 146% at temperatures 200 °C and 600 °C, respectively (**Fig.** 6-12). This can be attributed to the exacerbated crack propagation which was more intensively generated when the exposure temperature increased from 200 °C to 600 °C, due to the gradually increased dehydration and microstructural decomposition [29]. It was emphasized that pore connectivity is a key factor that control the extent of self-healing. Thus, the more the existing damage, the more pores connectivity, the more the potential of ions diffusion. These ions can undergo into the chemical reaction to form more self-healing products [99].

This indicated that the self-healing percentage was directly proportional to the exposure temperatures. Moreover, self-healing results based on RCPT values followed the same trend as UPV and sorptivity tests. However, due to the aforementioned RCPT limitation, its self-healing percentage was notably higher than that in UPV and sorptivity tests.

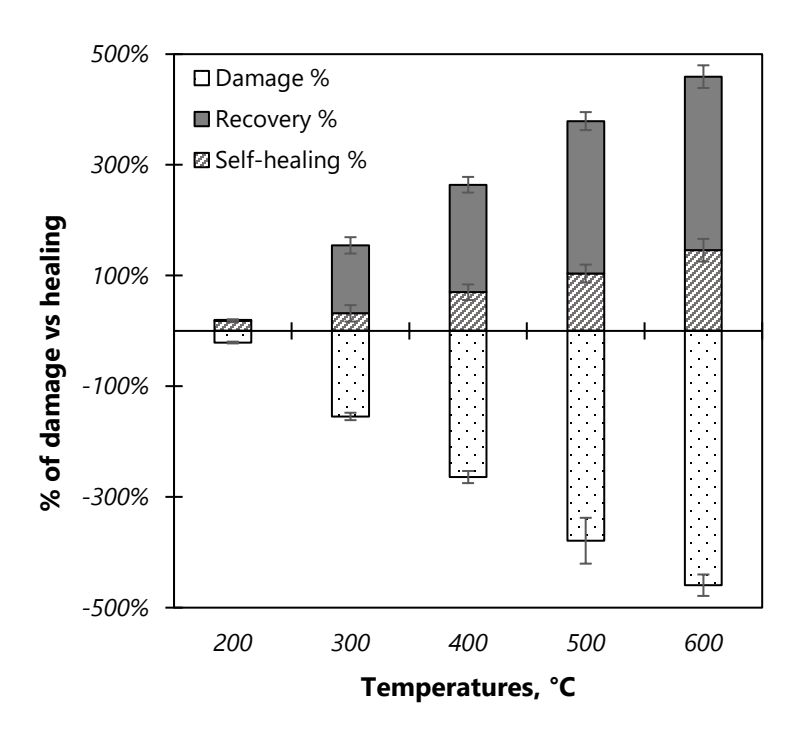


Fig. 6-12 Percentage of damage and self-healing according to RCPT.

# **6.5.5 SEM-EDX**

The 400 °C and 600 °C NC-AAS specimens were selected for microstructural analyses (SEM-EDX), as they showed high intensity of surface self-healing products according to the conducted optical microscope analysis. **Fig.** 6-13 depicts a typical image of self-healing products formed within surface cracks. The self-healing product had crystals of various shapes such as trigonal, cubical, and rectangular. The EDX analysis indicated that the healing product was primarily composed of calcium, along with some carbon and oxygen, confirming the formation of CaCO<sub>3</sub> as a healing product.

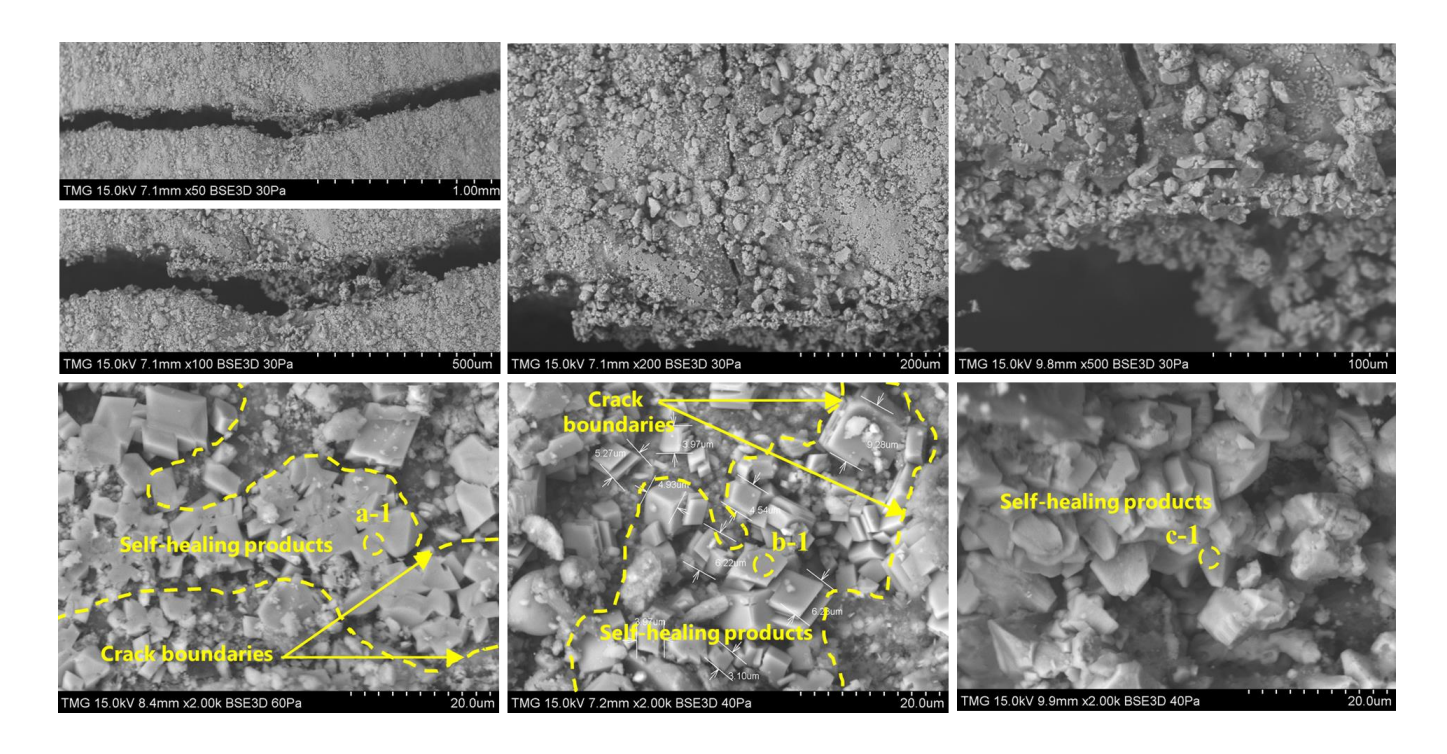


Fig. 6-13 SEM observation on cracks after self-healing treatment of AAS

**Table 6-4.** The chemical composition of the healing material

Position	Ratio	C	0	Na	Mg	Al	Si	Ca
a-1	Atomic	18.8	62.3	0.43	0.31	0.14	0.37	17.7
b-1	Atomic	16.9	61.6	0.45	0.11	0.11	0.53	20.3
c-1	Atomic	20.7	65.5	0.68	0.27	0.12	0.35	12.4

6.5.6 XRD analysis

Three separate sets of samples were examined: the reference, the 600 °C fire-damaged, and the 600 °C NC-AAS. The 600 °C NC-AAS specimen was selected as it has exhibited significant recovery in UPV, sorptivity, and RCPT tests. The XRD patterns obtained from these distinct sample sets were compared to understand any variations in crystallographic phases. The identification of new crystal phases, alterations in existing phases, or the restoration of initial phases in the self-healed samples could indicate the activation of the applied self-healing scheme within the AAS materials.

As illustrated in **Fig.** 6-14, For reference specimens (i.e., before the exposure), the main peak around 30° 2θ is attributed to the hydration product C-A-S-H and carbonate species due to the alkalis' carbonation in the AAS matrix [29]. Then, after being exposed to elevated temperatures (i.e., 600 °C), the main peak decreased due to the decomposition of the microstructure C-A-S-H and calcite decomposition which started at a temperature of 400°C [29]. However, after reactivation by 2M NaOH, further hydration altered the phase composition of the product significantly as the intensity of the main diffraction peak increased. This peak might be attributed to the superimposition of the diffuse peaks of the C-A-S-H gel and the strongest diffraction peak of the CaCO<sub>3</sub> crystal [65]. These self-healing products would enhance the mechanical behavior of the AAS through the formation of C-A-S-H, and its durability by sealing the surface cracks due to calcite precipitations.

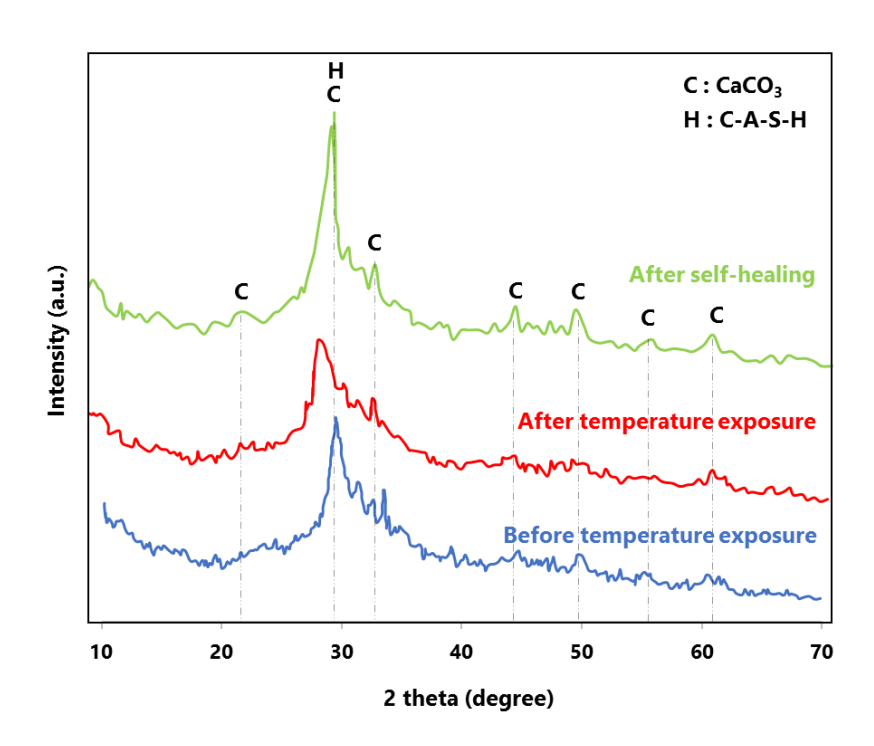


Fig. 6-14 XRD analysis

## 6.6 Conclusion and Recommendations

The potential of post-fire autogenous healing of AAS has been investigated. Self-healing quantification and microstructural morphology alteration of AAS have also been addressed. The conditioning scheme using NaOH (2M in molarity) solution was the triggering mechanism utilized for self-healing purposes. After elevated temperature exposure and applying the post-fire healing scheme, the following conclusion could be drawn as:

- AAS has the self-healing ability after elevated temperature exposure using the activation solution (i.e., NaOH).
- The self-healing extent has been demonstrated to be governed by the initial damage level. As
  the degree of initial damage increases, the subsequent self-healing would also increase due
  to the intensive formation and densification of healing products.

- The followed NC-AAS self-healing scheme was significantly revealed to improve the closure of crack openings. This can be ascribed to the intensive formation of the dominant self-healing product, i.e., CaCO<sub>3</sub>, which is characterized by its effective contribution to the recovery of durability.
- Although the dominant healing material was CaCO<sub>3</sub> in the form of calcite precipitation, the
  hydration product was C-A-S-H in accordance with the rehydration reaction, and some
  amount of Na<sub>2</sub>CO<sub>3</sub> might also be detected.
- This calcite precipitation sheds light on the underlying mechanisms of self-healing, providing a basis for optimizing healing processes and designing more durable AAS structures. This finding prompts further investigations into factors influencing calcite formation, alternative healing mechanisms, and supplementary materials to enhance self-healing efficacy. Moreover, it offers practical benefits by guiding strategies to extend the lifespan of AAS infrastructure, potentially reducing maintenance costs and environmental impact while improving structural resilience.

Despite those interesting findings, some limitations were identified:

- This study was conducted using a combination of sodium hydroxide and sodium silicate solutions; however, other types of activators might exhibit different self-healing mechanisms.
- This study was conducted by applying two different post-fire curing schemes i.e., sodium hydroxide solution and ambient air; however, implementation of other post-fire conditioning schemes might influence the self-healing process.

 This study was performed by exposing the specimens to the described elevated temperatures procedures; however, other fire exposure schemes might induce different damage in the AAS specimens.

Based on those before-mentioned conclusions, the following recommendations can be drawn:

- Tailoring the composition of AAS by adjusting the types and proportions of precursors, activators, and supplementary cementitious materials can enhance self-healing properties.
   Incorporating additives like nanomaterials, fibers, or crystalline admixtures could promote crack-bridging or nucleation sites for the formation of healing products.
- Adopting optimized post-curing conditions, such as maintaining moderate temperatures and
  relative humidity levels, can promote continuous hydration and improve the formation of
  secondary reaction products within damaged areas, aiding in self-healing.
- Introducing encapsulated healing agents within the AAS matrix, like microcapsules filled with healing agents or vascular networks containing healing agents, could facilitate autonomous repair by releasing healing agents when cracks appear.
- Conducting comprehensive long-term durability studies under different environmental conditions, exposure scenarios, and loading conditions will provide insights into the effectiveness and limitations of self-healing mechanisms in AAMs.

Chapter 7: Incorporation of Crystalline admixture to boost

autogenous self-healing of fire-damaged alkali-activated slag

Abstract

The durability of alkali-activated slag (AAS) binders has garnered significant attention due to their

sustainable and environmentally friendly properties. However, exposure to elevated temperatures

during fires can severely compromise the structural integrity of AAS-based materials. In this study,

the potential of crystalline admixtures (CA) to enhance the autogenous self-healing capacity of fire

damaged AAS was investigated. A series of AAS specimens, with and without CA, were exposed

to varying temperatures from 200 °C up to 800 °C. The self-healing efficiency was evaluated

through set of tests, compressive strength, tensile strength, water absorption, and permeability, with

a focus on autogenous self-healing mechanisms. Results showed that the incorporation of CA into

AAS significantly improved the self-healing performance post-fire exposure, particularly at higher

temperature of 600 °C. The CA facilitated enhanced formation of secondary hydration products

and crystalline structures within the cracks, which contributed to the reduction of permeability and

mechanical strength recovery. The study highlights the potential of CA as an effective solution to

mitigate fire-induced damage in AAS, providing a pathway toward more resilient and sustainable

construction materials.

**Keywords:** Alkali-activated slag; Elevated temperatures exposure; Autogenous self-healing.

119

#### 7.1 Introduction

The construction industry has long relied on Portland cement as a primary binder material [173]. However, the increasing focus on sustainability, environmental impact, and carbon footprint reduction has led to the exploration of alternative binders [4,8,81,108,109]. Alkali-activated materials (AAMs), specifically AAS, have gained considerable attention as a promising substitute for ordinary Portland cement (OPC) due to their lower carbon dioxide (CO<sub>2</sub>) emissions, utilization of industrial by-products, and superior mechanical and durability properties [17,103–107]. AAS binders are formed by activating ground granulated blast furnace slag (GGBFS) with high alkalinity activators, which induces a chemical reaction called geopolymerization that creates a hardened binder gel of three-dimensional network structure [5]. This environmentally friendly alternative offers significant advantages, such as high compressive strength, chemical resistance, and durability under aggressive environmental conditions [6,116,117].

However, one of the key challenges faced by AAS binders is their vulnerability to extreme conditions, particularly elevated temperatures caused by fire. Thus, more comprehensive studies were conducted to understand AAS's chemical and morphological alterations upon exposure to various elevated temperatures. Although AAS exhibited a superior performance under fire incidents than OPC, which undergoes calcium silicate hydrate (C-S-H) dehydration and recrystallization when exposed to high temperatures, AAS experiences unique degradation processes due to its low calcium/silica (Ca/Si) ratio and high alumina-silicate content [174]. Rovnaník *et al.* [29] studied the microstructural changes of AAS pastes after exposure to up to 1200 °C for 1h. From 20 °C to 575 °C, dehydration, and partial decomposition of calcium aluminum silicate hydrate (C-A-S-H) were observed, reducing compressive strength. Between 600 °C and 800 °C, a complete decomposition of AAS microstructures was reported [119,120]. Above

800 °C, new phases start to crystallize (i.e., Akermanite), enhancing the mechanical properties [29]. Microcracking, loss of structural integrity, and significant reduction in mechanical properties underscore the need for innovative solutions to enhance the durability and longevity of AAS concrete structures, paving the way for the exploration of self-healing technologies.

Autogenous self-healing, which refers to a material's ability to heal cracks without external intervention, has been an area of active research [90,91]. In alkali-activated slag materials, this selfhealing process is triggered when water comes into contact with the unreacted slag particles, leading to the reformation of binding phases such as C-A-S-H gels [62]. Also, the precipitating of calcite CaCO<sub>3</sub> crystals produced by a calcination process of calcium ions Ca<sup>2+</sup> existing into the AAS matrix [63]. These mechanisms not only close cracks but also help restore some of the degraded mechanical strength [92,175]. Furthermore, depending on the concept of self-healing, post-fire treatment becomes crucial for mitigating the damage effects caused by the extreme exposure to elevated temperatures [93]. AAS has a capability of self-healing in response to the fireinduced deteriorations. It was revealed that, upon exposure to a post-fire self-healing scheme (i.e. sodium hydroxide solution), AAS demonstrated an approximately 40% recovery in permeability, where calcium carbonate crystalline phases were detected as the predominant self-healing product. Moreover, microstructural densification was observed following the formation of the hydration product C-A-S-H [89]. This enhancement was exhibited at temperatures up to 400 °C, while limited improvement was recorded at higher temperatures 600 °C and 800 °C, displaying a potential gap in the production of more resilient AAS materials.

One potential solution is the incorporation of crystalline admixtures (CA) into AAS binders. Crystalline admixtures have been extensively used in OPC-based concrete for their ability to promote self-healing by forming insoluble crystals within cracks and voids [176]. These crystals

are typically produced when the admixture reacts with free water and certain ions, such as calcium and aluminum, to form secondary hydration products that seal cracks and reduce permeability [177]. In the context of AAS, the integration of CA offers a promising pathway for enhancing autogenous self-healing. By stimulating the formation of crystalline phases in AAS, CA can fill cracks, mitigate damage, and restore some of the lost mechanical and durability properties [74]. In this study, the incorporation of crystalline admixtures into alkali-activated slag was explored to investigate the potential of improving its autogenous self-healing capacity, especially after exposure to fire. A comprehensive investigation is conducted to assess the influence of CA on the mechanical performance, crack healing, and permeability reduction of fire-damaged AAS. It was hypothesized that the addition of CA leads to the formation of new crystalline phases, promoting crack closure and improving the long-term durability of AAS in the aftermath of fire damage. The outcomes of this research aim to provide a deeper understanding of the self-healing mechanisms in AAS and to contribute to the development of more resilient, sustainable, and durable construction materials for use in fire-prone environments.

#### 7.2 Materials and methods

#### 7.2.1 Materials

A ground granulated blast furnace slag (GGBFS) with a specific gravity of 2.92 g/cm<sup>3</sup>, a Blaine fineness of 515 m<sup>2</sup>/kg, and an average particle size of 15 μm was used as the main precursor to produce the AAS specimens. The GGBFS was sourced from Lafarge, located in Canada. This material conforms to the ASTM C989 [97] ensuring its quality and consistency for the intended applications in this study. Its chemical composition is shown in **Table** 7-1. A mix of sodium hydroxide (NaOH) solution and sodium silicate (Na<sub>2</sub>SiO<sub>3</sub>) solution was used as the alkali activator.

Sodium hydroxide pellets with 99.9% purity were dissolved in water, and then the solution was left for 24-h at room temperature to cool down. For this, a commercial sodium silicate solution (28.8% of SiO<sub>2</sub>, 9.01% of Na<sub>2</sub>O, 62.2% of H<sub>2</sub>O) was mixed with NaOH solution to produce the desired activator with silicate modulus (M<sub>S</sub> = SiO<sub>2</sub>/Na<sub>2</sub>O) of 1.25, and Na<sub>2</sub>O of 6 *wt*.% of the binder. Riverside sand with a fineness modulus of 2.70, a specific gravity of 2.61, and water absorption of 2.73% was used as fine aggregates (FA), meeting the ASTM C778 for standard sand [98]. It was provided by a local producer, ensuring the material's uniformity and suitability for use in concrete mixtures.

**Table 7-1:** Chemical composition of the used GGBFS

Constituents	SiO <sub>2</sub>	Al <sub>2</sub> O <sub>3</sub>	CaO	MgO	K <sub>2</sub> O	Na <sub>2</sub> O	Fe <sub>2</sub> O <sub>3</sub>	SO <sub>3</sub>
Percentage %	36.1	10.4	37.1	13.3	0.40	0.42	0.67	1.61

# 7.2.2 Mixture proportioning

For the mixtures proportioning along with the applied post-fire self-healing schemes, **Table** 7-2 was presented where a water-to-binder (w/b) ratio of 0.44 (including water from the activator) was selected and remained constant for the three studied mixtures. Crystalline admixture was implemented as 5 wt.% replacement of the binder [74]. GGBFS was dry mixed with fine aggregate for 1 min; then, the activator solution was added and mixed for 3 additional minutes, subsequently, CA agent was added and mixed for one more minute. Cube specimens with a dimension of  $50\times50\times50$  mm, dog bones samples, and cylinders  $100\times200$ mm were cast and sealed using plastic sheets [28]. After 24-h, all specimens were demolded and stored in sealed bags at the laboratory ambient temperature ( $23 \pm 1$  °C) until the cracking day (i.e. crack initiation using elevated temperatures).

**Table 7-2.** Mix proportioning and the applied post-fire self-healing scheme

Camples	Ma	Dosage		Cor	Post-exposure curing				
Samples	Ms	Na <sub>2</sub> O%	Binder	Sand	NaOH	Na <sub>2</sub> SiO <sub>3</sub>	Water*	CA	scheme
Control	1.25	6%	400	1148	19	104	111	0	Air
AAS	1.25	6%	400	1148	19	104	111	0	Water
AAS-CA	1.25	6%	380	1148	19	104	111	20	Water

# 7.2.3 Elevated Temperature Exposure

At 28 days of age, specimens were subjected to various elevated temperatures starting from 200 °C up to 800 °C. The selected temperature range was selected as they can represent the dehydration and major microstructural alterations. For instance, from 200 °C to 600 °C, dehydration and partial microstructural decomposition were exhibited, however, from 600 °C to 800 °C, a complete decomposition for the AAS hydration products was accomplished. There was no need to go beyond the 800 °C as there is a huge failure in the mechanical properties [29]. An electrical heating furnace was used, where the specimens were heated up at an increasing rate of 5–10 °C/min, according to the standard ASTM E831 [145], until reaching the targeted temperature, which was maintained for 1h, followed by naturally cooling down at ambient temperature inside the furnace [146]. To ensure that the specimen core reached the targeted temperature, the temperature at the center of a dummy specimen was monitored using a thermocouple type K. Specimen's temperature, along with the oven temperature, was continuously monitored and recorded using a data acquisition system.

# 7.2.4 Self-healing Study

After the elevated temperature exposure, specimens of each mixture were subjected to the self-healing scheme indicated in **Table** 7-2. For 28 days, control specimens were kept at uncontrolled

ambient temperature ( $23 \pm 1$  °C) in the lab, while AAS and AAS-CA specimens were immersed in the conditioning scheme (i.e. water). This scheme was applied to trigger un-hydrated particles to react with the existing activator ions by improving the diffusion into the matrix through inducing saturation condition. Furthermore, for AAS-CA, amorphous phases of this implemented additives were targeted to undergo into crystallization reactions to produce further self-healing products. Then, all groups' specimens were tested to quantify the efficiency of self-healing.

# 7.2.5 Testing Methods

To comprehensively evaluate the self-healing capabilities of AAS subjected to post-fire curing, a combination of methods was employed, each selected for its proven effectiveness in assessing specific aspects of material recovery and integrity restoration. Visual inspection offers a direct, initial assessment of the response of crystalline admixture under elevated temperatures exposure. It provides immediate, visible evidence of the additives structural stability, which is essential for preliminary evaluation. Cube samples  $50 \times 50 \times 50$  mm were cast to determine compressive strength of AAS mortars according to ASTM C109/109 M standards. Moreover, dog-bone shaped briquettes with dimensions 75 mm in length, 25 mm in thickness, and 625 mm<sup>2</sup> cross-section area at the mid-length were cast, to evaluate the direct tensile strength according to AASHTO T132. Water sorptivity assesses the material's capacity to absorb water through capillary action, which decreases as self-healing products seal cracks and pores. A reduction in water sorptivity is a key indicator of effective self-healing, particularly in terms of enhanced durability against moisture ingress [31]. The test was performed according to the ASTM C1585 standard [154] on triplicate cylindrical specimens with a diameter of 100 mm and a thickness of 50 mm. The capillary absorption (I) and the sorptivity index  $(S_I)$  were calculated and considered to assess the rate at which water permeates. Water penetration through the self-healed specimens of each mixture was measured using The RILEM Test Method II.4 (Measurement of Water Absorption under Low Pressure) by calculating the water permeability coefficient, k (cm/s) according to Eq. 1.

$$K = \frac{a \times L}{A \times t} \ln \frac{h1}{h2}$$
 Eq.1

A scanning electron microscope and energy dispersive x-ray tests (SEM-EDX) were performed for the microstructure analyses using Phenom ProX Scanning Electron Microscope with EDX capability.

#### 7.3 Results and discussion

## 7.3.1 Visual inspection

The thermal and structural stability of the crystalline admixture was assessed by subjecting the material to elevated temperatures of 200°C, 400°C, 600°C, and 800°C, as shown in Fig. 7-1. One of the key visual indicators of thermal degradation or transformation in materials is a change in color, which can signify alterations in chemical composition or crystalline structure. Interestingly, in this study, no visible change in color was observed even at 800°C, indicating that the crystalline admixture maintained its thermal stability throughout the temperature range tested. The absence of color change suggests that the admixture possesses robust thermal resistance, which is crucial for applications involving high-temperature exposure, such as post-fire environments. This stability indicates that the crystalline structure of the admixture remains intact at temperatures as high as 800°C, thereby retaining its functionality and integrity. Such thermal stability is vital for ensuring the admixture's contribution to the autogenous self-healing of AAS remains effective even after exposure to high temperatures, such as during a fire event. Additionally, the stability at elevated temperatures implies that the admixture does not undergo significant physicochemical

transformations that could affect its reactivity or compatibility with the AAS matrix. This finding supports the suitability of the crystalline admixture for use in enhancing the post-fire self-healing properties of AAS, as it can endure severe thermal conditions without compromising its structural or functional performance.

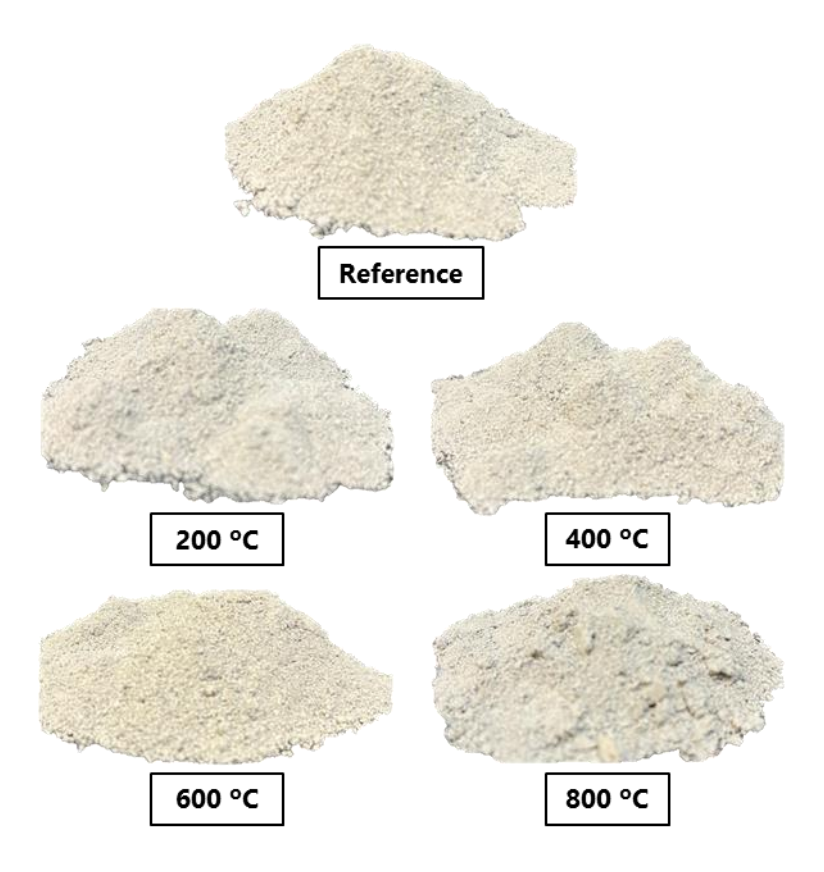


Fig. 7-1. Thermal and structural stability of the crystalline admixture

Upon visual inspection of the post-fire self-healed AAS specimens, distinct formations of self-healing products were observed, as shown in **Fig.** 7-2. These formations included pin-like crystals, transparent pin-like crystals, and white rod-like crystals, which suggest the emergence of different crystalline phases as part of the self-healing process. The varied morphology of these crystals may be indicative of the crystalline admixture's role in promoting the formation of specific mineral phases that contribute to the healing mechanisms. The pin-like and rod-like structures observed are

consistent with crystal growth patterns that can arise from the recrystallization of components within the slag matrix. The presence of transparent pin-like crystals might suggest the formation of a hydrated phase, while the white rod-like crystals could indicate a more solid, mineralized phase. The admixture's ability to maintain its structural stability even at high temperatures, as demonstrated earlier, likely supports the development of these crystalline structures, aiding in the closure of cracks and voids formed during the fire event.

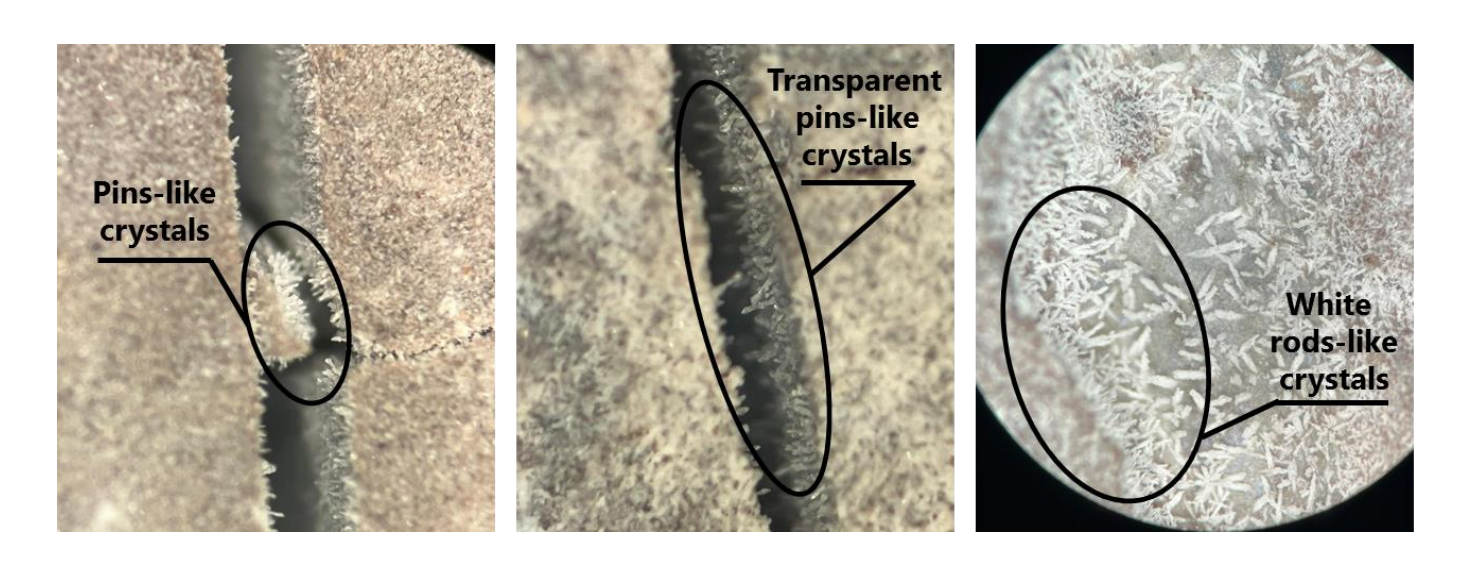
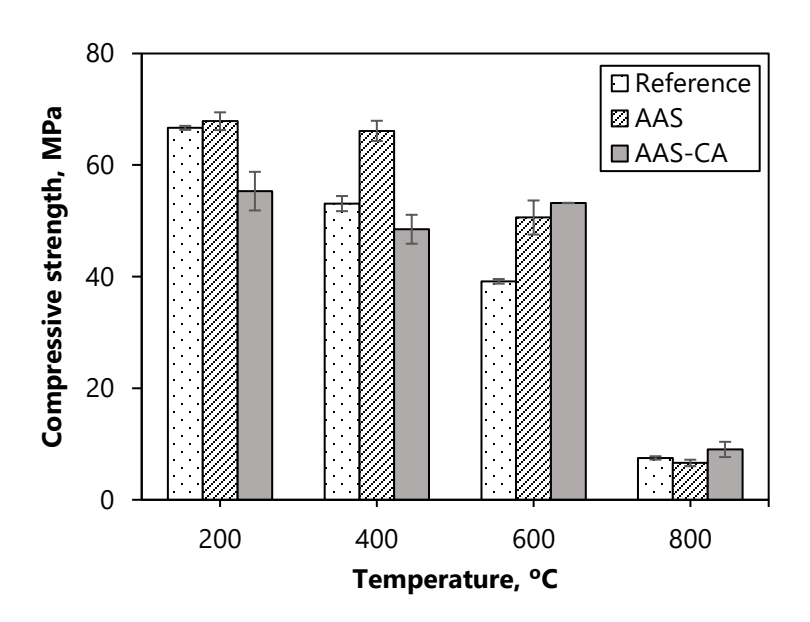


Fig. 7-2. Different crystal formations upon implementation of crystalline admixture

## 7.3.2 Compressive strength

The compressive strength results indicate distinct behaviors for the reference, AAS, and AAS-CA samples. The reference sample showed a typical reduction in strength with increasing temperatures, dropping from 66 MPa at 200°C to 7.5 MPa at 800°C. The AAS sample retained higher strength, remaining relatively stable between 200°C (67 MPa) and 400°C (66 MPa), and decreasing modestly to 50 MPa at 600°C, before a sharp drop to 8 MPa at 800°C. In contrast, the sample with crystalline admixture exhibited a unique trend, starting with lower strengths at 200°C (55 MPa)

and 400°C (48 MPa), but significantly improving to 53 MPa at 600°C and slightly higher retention at 800°C (9 MPa). These results suggest that while water curing improves strength retention at lower temperatures, the crystalline admixture enhances thermal resistance and self-healing capacity at higher temperatures, particularly at 600°C, as shown in **Fig.** 7-3.



**Fig. 7-3.** Compressive strength of the control, post-fire water cured (AAS), and specimens with crystalline admixtures (AAS-CA)

## 7.3.3 Tensile strength

As shown in **Fig.** 7-4, tensile strength results revealed distinct trends for the reference, post-fire water-cured, and post-fire water-cured with crystalline admixture AAS samples at elevated temperatures. The reference sample showed a steady decline in tensile strength as the temperature increased, decreasing from 1.40 MPa at 200°C to 0.15 MPa at 800°C. This indicates that the reference AAS material is highly susceptible to tensile strength loss under thermal exposure. In contrast, the post-fire water-cured sample demonstrated an improvement in tensile strength up to 400°C, reaching 3.14 MPa before decreasing to 2.05 MPa at 600°C and 0.14 MPa at 800°C. This

suggests that water curing enhances tensile properties at lower to moderate temperatures but is still vulnerable to significant degradation beyond 600°C. The post-fire water-cured sample with a crystalline admixture exhibited the best performance across all temperatures. Starting at 3.61 MPa at 200°C, the tensile strength increased to 4.07 MPa at 400°C and 4.40 MPa at 600°C, showing continuous improvement even at elevated temperatures. At 800°C, although the strength decreased to 0.45 MPa, it still retained significantly more tensile strength compared to the reference and water-cured samples. This trend highlights the potential of the crystalline admixture to enhance tensile resistance under thermal stress, especially in higher temperature ranges.

The results indicate that post-fire treatments, particularly the addition of a crystalline admixture, significantly enhance the tensile performance of AAS. Water curing alone improves tensile strength at lower temperatures but is insufficient for high-temperature resistance. On the other hand, the crystalline admixture consistently outperformed the other samples, particularly at 600°C, where it reached the highest tensile strength (4.40 MPa), and showed better retention at 800°C. These findings underscore the importance of crystalline admixtures in enhancing the tensile resilience of AAS, making it more suitable for applications involving high thermal exposure. The ability of the crystalline admixture to improve performance at both moderate and high temperatures suggests that it could play a critical role in extending the service life and structural integrity of AAS materials in fire-prone or high-temperature environments.

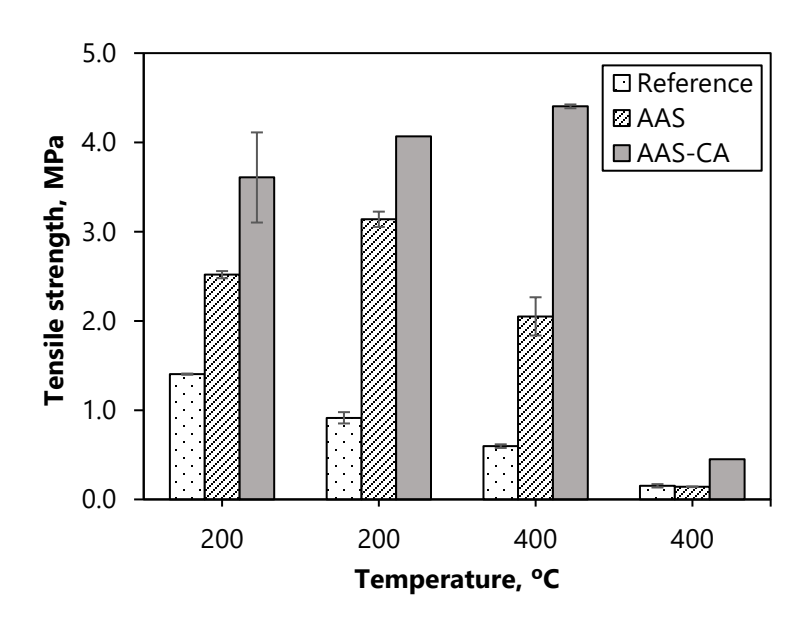


**Fig. 7-4.** Tensile strength of the control, post-fire water cured (AAS), and specimens with crystalline admixtures (AAS-CA)

## 7.3.4 Water Sorptivity

Fig. 7-5 plots the <u>capillary water</u> absorption test results of specimens from the three mixtures reference, AAS, AAS-CA. The sorptivity coefficient was fitted using linear regression. AAS-CA had minimum water absorption (Fig. 7-5(c)), which is likely due to incorporation of CA, a synthetic <u>cementitious material</u> containing reactive <u>silica</u> and crystalline catalysts, used as a concrete permeability reducer [178]. These compounds was able to produce pore-blocking precipitates, which decrease water absorption [179]. A slightly lower water absorption compared to that of the control was observed for AAS. As shown in Fig. 7-5 (b), water absorption increased more rapidly in cracked specimens. The sorptivity index of the cracked AAS specimen, for instance, was 0.03396 mm/√sec (Fig. 7-6 (a)). In contrast, it was 0.0573 mm/√sec for the cracked specimen AAS-CA, likely because the crack acted as a capillary pipe for water absorption and restoration [180]. It can be observed that the sorptivity coefficient in specimens from the two

mixtures after water curing decreased markedly, especially for the AAS-CA specimens, indicating the more significant self-healing in AAS-CA specimens. To quantitatively determine the self-healing efficiency, the sorptivity coefficient reduction ratio, was calculated for each specimen at cracking and after healing. Results indicate that cracked specimens incorporating CA achieved a much higher reduction in the sorptivity coefficient compared to that of specimens from the other two mixes.

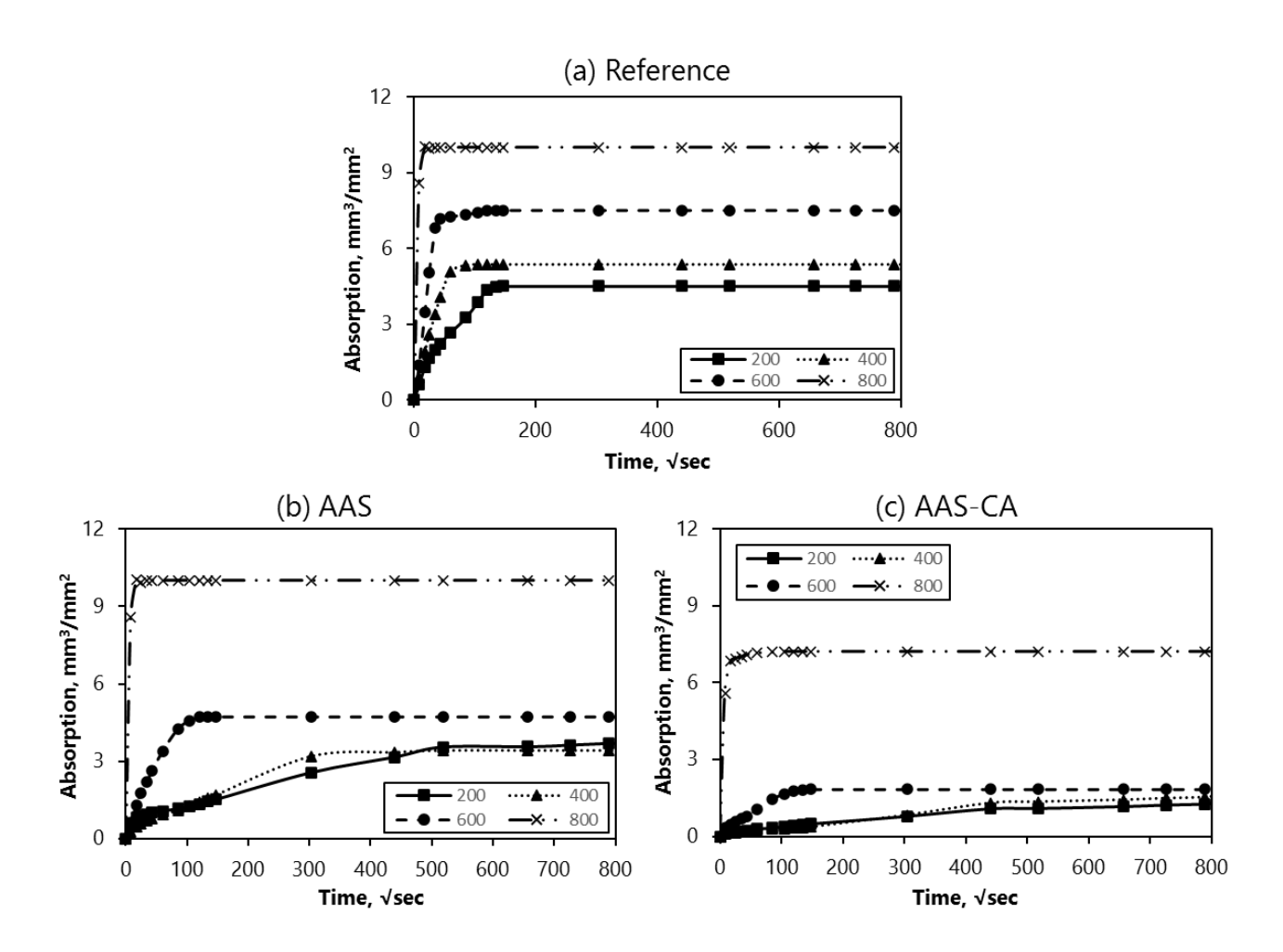


Fig. 7-5. Absorption of (a) control (b) AAS without crystalline admixture (c) AAS with CA

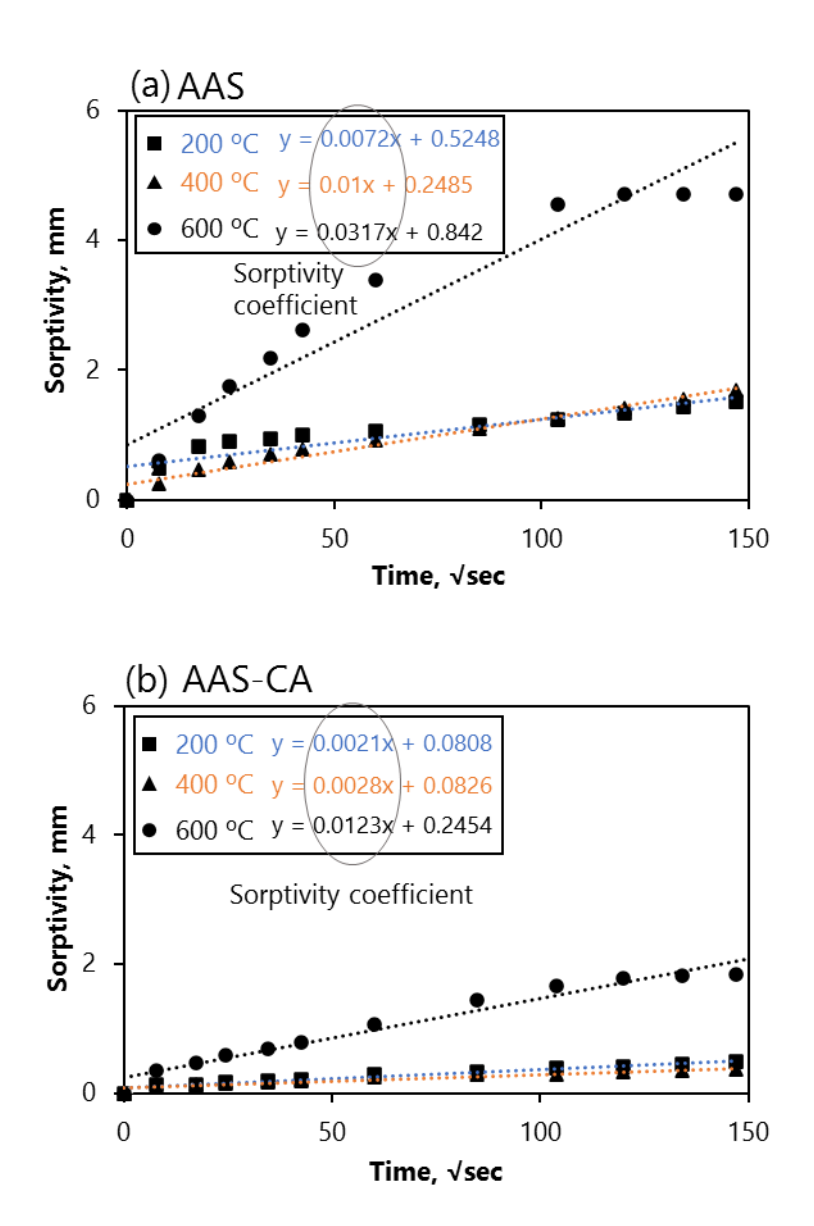


Fig. 7-6. Sorptivity of (a) AAS without crystalline admixture (b) AAS with CA

### 7.3.5 Permeability

The permeability coefficient results provide insight into the ability of the AAS samples to resist fluid ingress after exposure to elevated temperatures. The reference sample exhibited a significant increase in permeability as the temperature increased, starting at 14.7 at 200°C, remaining

relatively stable at 14.2 at 400°C, and then rising sharply to 63.1 at 600°C and 1195 at 800°C. This dramatic rise at higher temperatures indicates that the reference AAS material suffers from severe degradation of its microstructure when exposed to temperatures above 400°C, leading to increased permeability and reduced durability. The post-fire water-cured AAS sample followed a similar trend, with the permeability coefficient slightly lower than the reference sample at 200°C (14) and 400°C (13.1). However, the permeability increased significantly at 600°C (80.3) and 800°C (1195), mirroring the reference sample's behavior. This suggests that while water curing provides some minor improvements in permeability at lower temperatures, it is insufficient to prevent substantial permeability increases at higher temperatures, particularly beyond 600°C. In contrast, the post-fire water-cured sample with a crystalline admixture displayed a markedly different trend, with much lower permeability across all temperature ranges. Starting at 11.2 at 200°C, the permeability dropped to 5 at 400°C and 6.1 at 600°C, indicating that the crystalline admixture plays a significant role in maintaining a denser and more impermeable matrix under thermal stress. Even at 800°C, where the permeability coefficient rose to 1195 in all samples due to extensive thermal damage, the crystalline admixture demonstrated superior performance at lower temperatures, suggesting that it significantly enhances resistance to permeability up to 600°C.

Crystalline admixture showed a remarkable ability to maintain low permeability, even as temperatures increased. The substantial drop in permeability from 11.2 at 200°C to 5 at 400°C, followed by a slight increase to 6.1 at 600°C, indicates that the admixture effectively enhances the microstructure's resistance to cracking and porosity development under thermal conditions. This is likely due to the formation of crystalline phases that improve the density and cohesion of the material, reducing permeability even under elevated thermal stress. The crystalline admixture's performance at 600°C, where permeability remained much lower than in the other samples,

demonstrates its potential for enhancing the durability and long-term performance of AAS in hightemperature environments.

The permeability results indicate that high temperatures significantly degrade the microstructure of AAS, leading to increased permeability. The reference and water-cured samples showed similar trends, with both experiencing substantial permeability increases at 600°C and 800°C. While water curing provides some benefits at lower temperatures, it is ineffective in preventing severe permeability rise at higher temperatures. In contrast, the crystalline admixture provided a significant reduction in permeability, particularly at 400°C and 600°C, suggesting that it effectively improves the thermal stability and impermeability of the AAS matrix. This makes it a valuable addition for applications where long-term exposure to elevated temperatures is expected, as it enhances the material's ability to resist fluid penetration and maintain structural integrity under thermal stress. The consistent performance of the crystalline admixture up to 600°C highlights its potential as a crucial factor in improving the fire resistance and durability of AAS materials in severe environments.

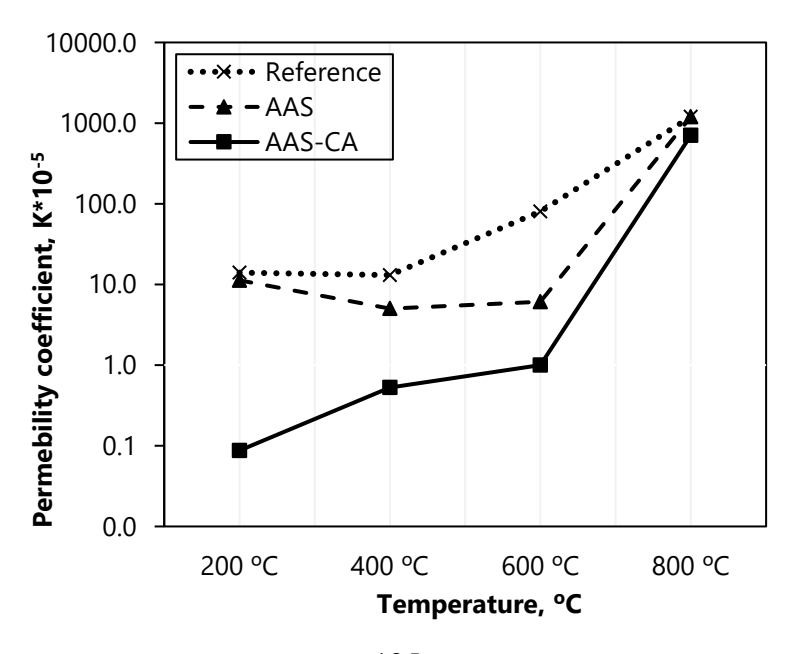
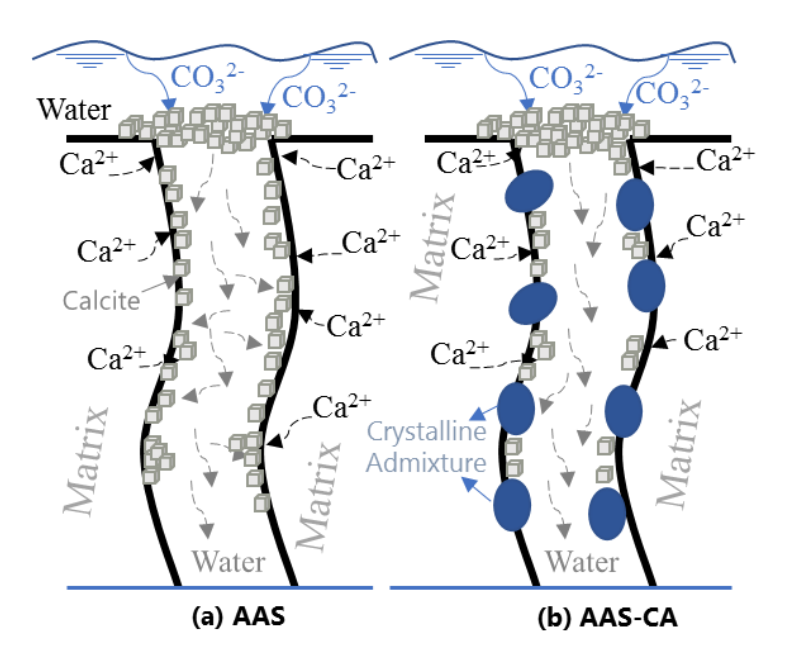


Fig. 7-7. Permeability coefficient for control, AAS without CA, and AAS with CA

#### 7.4 Discussion

This study explored the effects of post-fire treatments, specifically water curing and the addition of a crystalline admixture, on the performance of alkali-activated slag (AAS) subjected to elevated temperatures. The results indicated that while water curing provides some benefits in stabilizing the material's properties at lower temperatures, it falls short in preventing significant degradation at higher temperatures. In contrast, the crystalline admixture demonstrated its effectiveness in enhancing the thermal stability and overall durability of AAS. The presence of this admixture not only improved the material's performance under thermal stress but also contributed to better microstructural integrity. This is evidenced by the material's ability to maintain mechanical strength and reduce permeability, which is critical for mitigating fluid ingress and long-term deterioration, especially in high-temperature environments. The crystalline admixture appears to play a crucial role in reinforcing the AAS matrix, likely through the formation of crystalline phases that enhance cohesion and density. This enhancement in microstructure is particularly important in applications where exposure to elevated temperatures is anticipated, such as in construction materials subjected to fire or high thermal loads. Overall, the findings suggest that incorporating a crystalline admixture is a highly effective strategy for improving the resilience of AAS materials. By enhancing thermal resistance and structural integrity, the crystalline admixture can significantly extend the service life and durability of AAS in demanding conditions, making it a valuable addition for applications requiring enhanced performance in high-temperature environments.



**Fig. 7-8.** Schemetic diagram for self-healing (a) without crystalline admixture (b) using crystalline admixture

### 7.5 Conclusion and Recommendations

- Water curing improved both compressive and tensile strength of alkali-activated slag (AAS) at lower temperatures (200°C and 400°C), but was insufficient to prevent significant degradation at higher temperatures (600°C and 800°C).
- The crystalline admixture enhanced the compressive strength of AAS at higher temperatures, particularly at 600°C, where it outperformed both the reference and water-cured samples.
- In terms of tensile strength, the crystalline admixture showed continuous improvement up to 600°C and retained more strength at 800°C compared to the other samples, indicating its superior resistance to thermal stress.
- Permeability tests revealed a significant reduction in permeability for the crystalline admixture-treated samples, especially at 400°C and 600°C, indicating that it helps maintain a denser, less porous microstructure even under high-temperature exposure.

- Water curing alone had a minimal effect on permeability and could not prevent the sharp increase in permeability at temperatures beyond 400°C, highlighting its limited effectiveness in enhancing long-term thermal resistance.
- Overall, the crystalline admixture demonstrated significant improvements in thermal stability, strength retention, and resistance to permeability, making it a valuable addition for AAS applications exposed to high temperatures or fire.
- The findings suggest that incorporating a crystalline admixture can significantly enhance the durability, thermal resistance, and longevity of AAS materials in fire-prone or high-temperature environments.

# **Chapter 8: Conclusion, Recommendations, and Future Work**

#### 8.1 Introduction

This final chapter provides a comprehensive synthesis of the key findings from the experimental investigations carried out in this research on the post-fire self-healing performance of alkaliactivated slag (AAS) materials. The study systematically explored the effects of activator dosage, post-fire curing schemes (including water immersion, wet-dry cycles, and alkaline activation), and the incorporation of crystalline admixtures. In addition to summarizing the principal outcomes, this chapter critically reflects on the contributions made, discusses the practical implications, identifies the limitations, and outlines recommendations for future work.

### 8.2 Summary of Major Findings

### 8.2.1 Effect of Activator Dosage and Post-Fire Water Curing

The activator dosage implemented to initiate the geopolymerization reaction in AAS was revealed as a key factor controlling the extent of post-fire self-healing. The following conclusions were drawn:

- Water post-fire curing significantly enhanced the self-healing abilities of AAS through the formation of secondary hydration products and calcium carbonate precipitations.
- Specimen WCAAS-1.5-8 exhibited the highest self-healing percentages due to its higher ionic concentration, promoting the formation of extensive healing products.
- Specimen WCAAS-1-4 showed pronounced calcite precipitation, attributed to higher calcium ion diffusion.
- Although WCAAS-1.5-8 and WCAAS-1-4 demonstrated considerable self-healing through distinct mechanisms, WCAAS-1.25-6 achieved the best overall self-healing performance, balancing both hydration and carbonation healing pathways.

## 8.2.2 Post-Fire Wet-Dry Curing Scheme

The wet-dry curing scheme, compared against water immersion and air curing, provided the following insights:

- Wet-dry cycles significantly improved the self-healing ability of AAS specimens after fire exposure.
- Calcite precipitation (CaCO<sub>3</sub>) was the predominant healing product, driven by the saturated-dehydrated nature of the wet-dry environment, which enhanced carbonation.
- New hydration products, including Na-substituted C-S-H, were formed due to the drying phase, further contributing to crack closure.
- Wet-dry cycles proved more effective than traditional water immersion in promoting self-healing, suggesting the superiority of environmentally realistic curing conditions.

## 8.2.3 Post-Fire Healing Using Alkaline Solution (NaOH)

Using a NaOH (2M) solution as a post-fire healing medium revealed additional self-healing potential:

- AAS materials demonstrated considerable self-healing capacity after high-temperature exposure when conditioned with NaOH solution.
- Higher initial damage levels were associated with increased self-healing due to intensified formation of healing products.
- Crack closure was significantly enhanced by the formation of calcium carbonate, with secondary products including C-A-S-H and minor amounts of Na<sub>2</sub>CO<sub>3</sub>.
- These findings shed light on the mechanisms governing self-healing and emphasize the role of carbonation and rehydration in restoring AAS durability after fire damage.

# 8.2.4 Incorporation of Crystalline Admixture for Post-Fire Healing

The final part of the study investigated the impact of crystalline admixture incorporation:

- Water curing improved the compressive and tensile strength recovery of AAS at moderate temperatures (200°C–400°C); however, its effect diminished at higher temperatures (600°C–800°C).
- The crystalline admixture significantly enhanced strength retention, particularly at 600°C, and demonstrated superior tensile performance up to 800°C.
- Permeability testing revealed a marked reduction in permeability in crystalline admixturetreated samples at elevated temperatures, maintaining a denser microstructure.
- Overall, the crystalline admixture proved to be a highly effective additive for improving post-fire durability, thermal resistance, and long-term structural performance of AAS materials.

#### **8.3 Critical Reflections and Contributions**

This research offers several important contributions:

- It advances the understanding of post-fire autogenous healing mechanisms in alkaliactivated materials, particularly under various environmental conditioning regimes.
- It provides the first comprehensive comparison of water immersion, wet-dry, and alkaline solution post-fire healing strategies for AAS.
- It demonstrates the significant benefits of crystalline admixtures in enhancing thermal resilience and post-fire durability of AAS-based systems.
- It highlights the pivotal role of carbonation and secondary hydration in the self-healing process of thermally damaged geopolymeric materials.

These contributions are critical for developing more resilient and sustainable materials for fireexposed structures.

### **8.4 Practical Implications**

The findings have practical relevance for material design, construction practices, and post-fire rehabilitation:

- Optimized activator compositions and curing strategies can enhance the self-healing performance of AAS-based structures after fire incidents.
- Crystalline admixtures offer a viable method to significantly improve AAS performance in high-temperature or fire-prone applications.
- Wet-dry cycles provide an environmentally friendly post-fire healing approach, compatible with real-world exposure conditions.
- Incorporating self-healing mechanisms in material design can reduce long-term maintenance costs and enhance infrastructure resilience.

## 8.5 Limitations of the Study

While the study generated significant findings, some limitations should be acknowledged:

- The experimental program was conducted at laboratory scale; extrapolation to real structures requires further validation.
- Only a specific combination of slag, activator, and admixtures was examined; results may vary with different materials.
- Fire exposure was simulated using controlled laboratory heating; real fire conditions could produce more complex damage patterns.
- The study primarily focused on mechanical and microstructural assessments; broader durability performance under cyclic or combined loading remains unexplored.

#### 8.6 Recommendations for Future Research

Building upon this work, the following future research directions are recommended:

- Full-Scale Testing: Evaluate the self-healing behavior of AAS-based structural elements (e.g., slabs, beams) under realistic fire and post-fire conditions.
- **Diverse Material Systems:** Investigate alternative activator systems, precursor materials, and admixture types to broaden the understanding of self-healing mechanisms.

- Environmental and Mechanical Loading: Explore the effect of simultaneous environmental exposure (freeze-thaw, chloride ingress) and mechanical stresses on the healing efficacy.
- Advanced Healing Agents: Develop and test novel healing agents such as microcapsules, vascular networks, or bio-based systems embedded within the AAS matrix.
- **Mechanistic Modelling:** Create predictive models linking damage severity, healing kinetics, and mechanical recovery to facilitate design integration.
- **Life Cycle Assessment:** Conduct sustainability analyses to quantify the long-term environmental and economic benefits of self-healing AAS structures.

#### 8.7 Final Remarks

This research reaffirms the promising potential of alkali-activated slag as a sustainable, durable construction material capable of self-healing after fire exposure. By integrating advanced curing methods and innovative additives such as crystalline admixtures, AAS systems can be engineered to achieve enhanced resilience, reduced maintenance demands, and longer service lives. These advancements contribute directly to the overarching goals of sustainable construction and disaster-resilient infrastructure development.

## References

- [1] T. Xie, Togay Ozbakkaloglu, Behavior of low-calcium fly and bottom ash-based geopolymer concrete cured at ambient temperature, Ceramics International 41 (2015) 5945–5958. https://doi.org/10.1016/j.ceramint.2015.01.031.
- [2] Z. Zhang, J.L. Provis, A. Reid, H. Wang, Geopolymer foam concrete: An emerging material for sustainable construction, Construction and Building Materials 56 (2014) 113–127. https://doi.org/10.1016/j.conbuildmat.2014.01.081.
- [3] B.C. McLellan, R.P. Williams, J. Lay, A. van Riessen, G.D. Corder, Costs and carbon emissions for geopolymer pastes in comparison to ordinary portland cement, Journal of Cleaner Production 19 (2011) 1080–1090. https://doi.org/10.1016/j.jclepro.2011.02.010.
- [4] P. Duxson, J.L. Provis, G.C. Lukey, J.S.J. van Deventer, The role of inorganic polymer technology in the development of 'green concrete,' Cement and Concrete Research 37 (2007) 1590–1597. https://doi.org/10.1016/j.cemconres.2007.08.018.
- [5] Q. Fu, M. Bu, Z. Zhang, W. Xu, Q. Yuan, D. Niu, Hydration Characteristics and

- Microstructure of Alkali-Activated Slag Concrete: A Review, Engineering 20 (2023) 162–179. https://doi.org/10.1016/j.eng.2021.07.026.
- [6] A. Wang, Y. Zheng, Z. Zhang, K. Liu, Y. Li, L. Shi, D. Sun, The Durability of Alkali-Activated Materials in Comparison with Ordinary Portland Cements and Concretes: A Review, Engineering 6 (2020) 695–706. https://doi.org/10.1016/j.eng.2019.08.019.
- [7] T. Alomayri, A. Adesina, S. Das, Influence of amorphous raw rice husk ash as precursor and curing condition on the performance of alkali activated concrete, Case Studies in Construction Materials 15 (2021) e00777. https://doi.org/10.1016/j.cscm.2021.e00777.
- [8] V.D. Glukhovsky, Ancient, modern and future concretes, in: Kiev, Ukraine, 1994: pp. 1–8.
- [9] V.D. Glukhovsky, G.S. Rostovskaja, G.V. Rumyna, High strength slag-alkaline cements, in: 1980: pp. 164–168.
- [10] S. Zhang, K. Gong, J. Lu, Novel modification method for inorganic geopolymer by using water soluble organic polymers, Materials Letters 58 (2004) 1292–1296. https://doi.org/10.1016/j.matlet.2003.07.051.
- [11] J.G.S. van Jaarsveld, J.S.J. van Deventer, The effect of metal contaminants on the formation and properties of waste-based geopolymers, Cement and Concrete Research 29 (1999) 1189–1200. https://doi.org/10.1016/S0008-8846(99)00032-0.
- [12] H. Xu, J.S.J. Van Deventer, The geopolymerisation of alumino-silicate minerals, International Journal of Mineral Processing 59 (2000) 247–266. https://doi.org/10.1016/S0301-7516(99)00074-5.
- [13] J.S.J. van Deventer, J.L. Provis, P. Duxson, G.C. Lukey, Reaction mechanisms in the geopolymeric conversion of inorganic waste to useful products, Journal of Hazardous Materials 139 (2007) 506–513. https://doi.org/10.1016/j.jhazmat.2006.02.044.
- [14] J. He, Y. Jie, J. Zhang, Y. Yu, G. Zhang, Synthesis and characterization of red mud and rice husk ash-based geopolymer composites, Cement and Concrete Composites 37 (2013) 108–118. https://doi.org/10.1016/j.cemconcomp.2012.11.010.
- [15] H.Y. Zhang, V. Kodur, S.L. Qi, B. Wu, Characterizing the bond strength of geopolymers at ambient and elevated temperatures, Cement and Concrete Composites 58 (2015) 40–49. https://doi.org/10.1016/j.cemconcomp.2015.01.006.
- [16] H.S. Gökçe, M. Tuyan, M.L. Nehdi, Alkali-activated and geopolymer materials developed using innovative manufacturing techniques: A critical review, Construction and Building Materials 303 (2021) 124483. https://doi.org/10.1016/j.conbuildmat.2021.124483.
- [17] D. Kanaan, A. el M. Safhi, A.R. Suleiman, A.M. Soliman, Fresh, Hardened, and Microstructural Properties of Ambient Cured One-Part Alkali-Activated Self-Consolidating Concrete, Sustainability 15 (2023) 2451. https://doi.org/10.3390/su15032451.
- [18] Y. Ding, J.-G. Dai, C.-J. Shi, Mechanical properties of alkali-activated concrete: A state-of-the-art review, Construction and Building Materials 127 (2016) 68–79. https://doi.org/10.1016/j.conbuildmat.2016.09.121.
- [19] X.C. Pu, C.C. Gan, S.D. Wang, C. %J C.I. of A. Yang, C. Engineering, Summary reports of research on alkali-activated slag cement and concrete, 1 (1988).
- [20] S.A. Bernal, R. Mejía de Gutiérrez, A.L. Pedraza, J.L. Provis, E.D. Rodriguez, S. Delvasto, Effect of binder content on the performance of alkali-activated slag concretes, Cement and Concrete Research 41 (2011) 1–8. https://doi.org/10.1016/j.cemconres.2010.08.017.
- [21] T. Bakharev, J.G. Sanjayan, Y.-B. Cheng, Effect of elevated temperature curing on properties of alkali-activated slag concrete, Cement and Concrete Research 29 (1999) 1619–1625.

- https://doi.org/10.1016/S0008-8846(99)00143-X.
- [22] M. Ben Haha, G. Le Saout, F. Winnefeld, B. Lothenbach, Influence of activator type on hydration kinetics, hydrate assemblage and microstructural development of alkali activated blast-furnace slags, Cement and Concrete Research 41 (2011) 301–310. https://doi.org/10.1016/j.cemconres.2010.11.016.
- [23] T. Bakharev, Geopolymeric materials prepared using Class F fly ash and elevated temperature curing, Cement and Concrete Research 35 (2005) 1224–1232. https://doi.org/10.1016/j.cemconres.2004.06.031.
- [24] W. Jiang, D.M. Roy, Hydrothermal processing of new fly ash cement, American Ceramic Society Bulletin; (United States) 71:4 (1992). https://www.osti.gov/biblio/6916819 (accessed October 5, 2024).
- [25] T.-H. Ueng, S.-J. Lyu, H.-W. Chu, H.-H. Lee, T.-T. Wang, Adhesion at interface of geopolymer and cement mortar under compression: An experimental study, Construction and Building Materials 35 (2012) 204–210. https://doi.org/10.1016/j.conbuildmat.2012.03.008.
- [26] P. Duan, C. Yan, W. Luo, A novel waterproof, fast setting and high early strength repair material derived from metakaolin geopolymer, Construction and Building Materials 124 (2016) 69–73. https://doi.org/10.1016/j.conbuildmat.2016.07.058.
- [27] M.H. Al-Majidi, A.P. Lampropoulos, A.B. Cundy, O.T. Tsioulou, S. Al-Rekabi, A novel corrosion resistant repair technique for existing reinforced concrete (RC) elements using polyvinyl alcohol fibre reinforced geopolymer concrete (PVAFRGC), Construction and Building Materials 164 (2018) 603–619. https://doi.org/10.1016/j.conbuildmat.2017.12.213.
- [28] R.J. Thomas, S. Peethamparan, Alkali-activated concrete: Engineering properties and stress–strain behavior, Construction and Building Materials 93 (2015) 49–56. https://doi.org/10.1016/j.conbuildmat.2015.04.039.
- [29] P. Rovnaník, P. Bayer, P. %J C. Rovnaníková, Building Materials, Characterization of alkali activated slag paste after exposure to high temperatures, 47 (2013) 1479–1487.
- [30] S. Luhar, I. Luhar, F.U.A. Shaikh, Review on Performance Evaluation of Autonomous Healing of Geopolymer Composites, Infrastructures 6 (2021) 94. https://doi.org/10.3390/infrastructures6070094.
- [31] A.R. Suleiman, M. %J C. Nehdi, Concrete Research, Effect of environmental exposure on autogenous self-healing of cracked cement-based materials, 111 (2018) 197–208.
- [32] H.H. Nguyễn, J.-I. Choi, K.-I. Song, J.-K. Song, J. Huh, B.Y. Lee, Self-healing properties of cement-based and alkali-activated slag-based fiber-reinforced composites, Construction and Building Materials 165 (2018) 801–811. https://doi.org/10.1016/j.conbuildmat.2018.01.023.
- [33] H.H. Nguyễn, J.-I. Choi, H.-K. Kim, B.Y. %J C. Lee, Building Materials, Effects of the type of activator on the self-healing ability of fiber-reinforced alkali-activated slag-based composites at an early age, 224 (2019) 980–994.
- [34] M. Shariati, A. Shariati, N.T. Trung, P. Shoaei, F. Ameri, N. Bahrami, S.N. Zamanabadi, Alkali-activated slag (AAS) paste: Correlation between durability and microstructural characteristics, Construction and Building Materials 267 (2021) 120886. https://doi.org/10.1016/j.conbuildmat.2020.120886.
- [35] J.H. Ross, M. Genedy, M.C.G. Juenger, E. van Oort, Permeability recovery by self-healing of class F fly ash-based geopolymers, CEMENT 10 (2022) 100048. https://doi.org/10.1016/j.cement.2022.100048.
- [36] H.-W. Reinhardt, M. %J C. Jooss, concrete research, Permeability and self-healing of cracked

- concrete as a function of temperature and crack width, 33 (2003) 981–985.
- [37] H.-W. Reinhardt, M. Jooss, Permeability and self-healing of cracked concrete as a function of temperature and crack width, Cement and Concrete Research 33 (2003) 981–985. https://doi.org/10.1016/S0008-8846(02)01099-2.
- [38] M.K. Ali, A.I. Abu-Tair, J.M. Kinuthia, R. Babecki, Self-healing and strength development of geopolymer concrete made with Waste by products, Civil and Environmental Engineering (2015).
- [39] H. Ulugöl, M.F. Günal, İ.Ö. Yaman, G. Yıldırım, M. Şahmaran, Effects of self-healing on the microstructure, transport, and electrical properties of 100% construction- and demolition-waste-based geopolymer composites, Cement and Concrete Composites 121 (2021) 104081. https://doi.org/10.1016/j.cemconcomp.2021.104081.
- [40] M. Rajczakowska, K. Habermehl-Cwirzen, H. Hedlund, A. Cwirzen, Autogenous Self-Healing: A Better Solution for Concrete, Journal of Materials in Civil Engineering 31 (2019) 03119001. https://doi.org/10.1061/(ASCE)MT.1943-5533.0002764.
- [41] M. Ismail, A. Toumi, R. François, R. %J C. Gagné, Concrete Research, Effect of crack opening on the local diffusion of chloride in inert materials, 34 (2004) 711–716.
- [42] M. Ismail, A. Toumi, R. François, R. %J C. Gagné, concrete research, Effect of crack opening on the local diffusion of chloride in cracked mortar samples, 38 (2008) 1106–1111.
- [43] C. De Nardi, A. Cecchi, L. Ferrara, A. Benedetti, D. Cristofori, Effect of age and level of damage on the autogenous healing of lime mortars, Composites Part B: Engineering 124 (2017) 144–157. https://doi.org/10.1016/j.compositesb.2017.05.041.
- [44] S. Fan, M. %J S. materials Li, structures, X-ray computed microtomography of three-dimensional microcracks and self-healing in engineered cementitious composites, 24 (2014) 015021.
- [45] S. Kramar, A. Šajna, V. Ducman, Assessment of alkali activated mortars based on different precursors with regard to their suitability for concrete repair, Construction and Building Materials 124 (2016) 937–944. https://doi.org/10.1016/j.conbuildmat.2016.08.018.
- [46] S. Kumar, R. Kumar, S. %J J. of materials science Mehrotra, Influence of granulated blast furnace slag on the reaction, structure and properties of fly ash based geopolymer, 45 (2010) 607–615.
- [47] P.S. Deb, P. Nath, P.K. Sarker, The effects of ground granulated blast-furnace slag blending with fly ash and activator content on the workability and strength properties of geopolymer concrete cured at ambient temperature, Materials & Design (1980-2015) 62 (2014) 32–39. https://doi.org/10.1016/j.matdes.2014.05.001.
- [48] A.M. Fernandez-Jimenez, A. Palomo, C. %J A.M.J. Lopez-Hombrados, Engineering properties of alkali-activated fly ash concrete, 103 (2006) 106.
- [49] P. Nath, P.K. Sarker, Effect of GGBFS on setting, workability and early strength properties of fly ash geopolymer concrete cured in ambient condition, Construction and Building Materials 66 (2014) 163–171. https://doi.org/10.1016/j.conbuildmat.2014.05.080.
- [50] A. Hawa, D. Tonnayopas, W. Prachasaree, P. Taneerananon, Development and Performance Evaluation of Very High Early Strength Geopolymer for Rapid Road Repair, Advances in Materials Science and Engineering 2013 (2013) 764180. https://doi.org/10.1155/2013/764180.
- [51] P. Awoyera, A. Adesina, A critical review on application of alkali activated slag as a sustainable composite binder, Case Studies in Construction Materials 11 (2019) e00268.

- https://doi.org/10.1016/j.cscm.2019.e00268.
- [52] S. Deng, P. Ren, Y. Jiang, X. Shao, T.-C. Ling, Use of CO2-active BOFS binder in the production of artificial aggregates with waste concrete powder, Resources, Conservation and Recycling 182 (2022) 106332. https://doi.org/10.1016/j.resconrec.2022.106332.
- [53] B. Tayebani, A. Said, A. Memari, Less carbon producing sustainable concrete from environmental and performance perspectives: A review, Construction and Building Materials 404 (2023) 133234. https://doi.org/10.1016/j.conbuildmat.2023.133234.
- [54] I. Lecomte, C. Henrist, M. Liégeois, F. Maseri, A. Rulmont, R. Cloots, (Micro)-structural comparison between geopolymers, alkali-activated slag cement and Portland cement, Journal of the European Ceramic Society 26 (2006) 3789–3797. https://doi.org/10.1016/j.jeurceramsoc.2005.12.021.
- [55] J.L. Provis, A. Palomo, C. Shi, Advances in understanding alkali-activated materials, Cement and Concrete Research 78 (2015) 110–125. https://doi.org/10.1016/j.cemconres.2015.04.013.
- [56] F.G. Collins, J.G. Sanjayan, Workability and mechanical properties of alkali activated slag concrete, Cement and Concrete Research 29 (1999) 455–458. https://doi.org/10.1016/S0008-8846(98)00236-1.
- [57] Z. Li, B. Delsaute, T. Lu, A. Kostiuchenko, S. Staquet, G. Ye, A comparative study on the mechanical properties, autogenous shrinkage and cracking proneness of alkali-activated concrete and ordinary Portland cement concrete, Construction and Building Materials 292 (2021) 123418. https://doi.org/10.1016/j.conbuildmat.2021.123418.
- [58] Y. Ding, J.-G. Dai, C.-J. Shi, Fracture properties of alkali-activated slag and ordinary Portland cement concrete and mortar, Construction and Building Materials 165 (2018) 310–320. https://doi.org/10.1016/j.conbuildmat.2017.12.202.
- [59] P. Chen, Z. Shi, S. Cao, P. Liu, X. Rong, L. Wang, Mechanical properties of alkali-activated slag lightweight aggregate concrete, Journal of Cleaner Production 359 (2022) 132136. https://doi.org/10.1016/j.jclepro.2022.132136.
- [60] H.T. Türker, M. Balçikanli, İ.H. Durmuş, E. Özbay, M. Erdemir, Microstructural alteration of alkali activated slag mortars depend on exposed high temperature level, Construction and Building Materials 104 (2016) 169–180. https://doi.org/10.1016/j.conbuildmat.2015.12.070.
- [61] N. Hammad, A. Elnemr, I.G. Shaaban, State-of-the-Art Report: The Self-Healing Capability of Alkali-Activated Slag (AAS) Concrete, Materials 16 (2023) 4394. https://doi.org/10.3390/ma16124394.
- [62] L.V. Zhang, M.L. Nehdi, A.R. Suleiman, M.M. Allaf, M. Gan, A. Marani, M. %J C.P.B.E. Tuyan, Crack self-healing in bio-green concrete, 227 (2021) 109397.
- [63] L.V. Zhang, A.R. Suleiman, M. %J J. of M. in C.E. Nehdi, Crack self-healing in NaOH-activated slag-based composites incorporating calcium hydroxide, 33 (2021) 04021012.
- [64] S. Aydın, B. Baradan, Effect of activator type and content on properties of alkali-activated slag mortars, Composites Part B: Engineering 57 (2014) 166–172. https://doi.org/10.1016/j.compositesb.2013.10.001.
- [65] J. Yang, Z. Sun, N. De Belie, D. Snoeck, Self-healing ability of cracks in alkali-activated slag systems incorporating superabsorbent polymers, Cement and Concrete Research 170 (2023) 107183. https://doi.org/10.1016/j.cemconres.2023.107183.
- [66] K. Gao, K.-L. Lin, D. Wang, C.-L. Hwang, H.-S. Shiu, Y.-M. Chang, T.-W. Cheng, Effects SiO2/Na2O molar ratio on mechanical properties and the microstructure of nano-SiO2 metakaolin-based geopolymers, Construction and Building Materials 53 (2014) 503–510.

- https://doi.org/10.1016/j.conbuildmat.2013.12.003.
- [67] A.E. Abubakr, A.M. Soliman, S.H. Diab, Effect of activator nature on the impact behaviour of Alkali-Activated slag mortar, Construction and Building Materials 257 (2020) 119531. https://doi.org/10.1016/j.conbuildmat.2020.119531.
- [68] A. Soliman, A.E. Abubakr, S.H. Diab, Effect of Activator Concentrations on the Postfire Impact Behavior of Alkali-Activated Slag Concrete, Journal of Materials in Civil Engineering 35 (2023) 04023166. https://doi.org/10.1061/JMCEE7.MTENG-14605.
- [69] S. Jacobsen, J. Marchand, H. Hornain, Sem observations of the microstructure of frost deteriorated and self-healed concretes, Cement and Concrete Research 25 (1995) 1781–1790. https://doi.org/10.1016/0008-8846(95)00174-3.
- [70] M.W. Keller, N.R. Sottos, Mechanical Properties of Microcapsules Used in a Self-Healing Polymer, Exp Mech 46 (2006) 725–733. https://doi.org/10.1007/s11340-006-9659-3.
- [71] B.S. Gebregziabiher, R.J. Thomas, S. Peethamparan, Temperature and activator effect on early-age reaction kinetics of alkali-activated slag binders, Construction and Building Materials 113 (2016) 783–793. https://doi.org/10.1016/j.conbuildmat.2016.03.098.
- [72] E. L'Hôpital, B. Lothenbach, K. Scrivener, D.A. Kulik, Alkali uptake in calcium alumina silicate hydrate (C-A-S-H), Cement and Concrete Research 85 (2016) 122–136. https://doi.org/10.1016/j.cemconres.2016.03.009.
- [73] U. De Filippis, E. Prud'homme, S. Meille, Relation between activator ratio, hydration products and mechanical properties of alkali-activated slag, Construction and Building Materials 266 (2021) 120940. https://doi.org/10.1016/j.conbuildmat.2020.120940.
- [74] L.V. Zhang, A.R. Suleiman, M.L. Nehdi, Self-healing in fiber-reinforced alkali-activated slag composites incorporating different additives, Construction and Building Materials 262 (2020) 120059. https://doi.org/10.1016/j.conbuildmat.2020.120059.
- [75] S. Aydın, B. Baradan, Mechanical and microstructural properties of heat cured alkaliactivated slag mortars, Materials & Design 35 (2012) 374–383. https://doi.org/10.1016/j.matdes.2011.10.005.
- [76] Y. Zuo, M. Nedeljković, G. Ye, Coupled thermodynamic modelling and experimental study of sodium hydroxide activated slag, Construction and Building Materials 188 (2018) 262–279. https://doi.org/10.1016/j.conbuildmat.2018.08.087.
- [77] J.L. Provis, S.A. Bernal, Geopolymers and Related Alkali-Activated Materials, Annual Review of Materials Research 44 (2014) 299–327. https://doi.org/10.1146/annurev-matsci-070813-113515.
- [78] J.I. Escalante-García, A.F. Fuentes, A. Gorokhovsky, P.E. Fraire-Luna, G. Mendoza-Suarez, Hydration Products and Reactivity of Blast-Furnace Slag Activated by Various Alkalis, Journal of the American Ceramic Society 86 (2003) 2148–2153. https://doi.org/10.1111/j.1151-2916.2003.tb03623.x.
- [79] M. Amran, G. Murali, N.H.A. Khalid, R. Fediuk, T. Ozbakkaloglu, Y.H. Lee, S. Haruna, Y.Y. Lee, Slag uses in making an ecofriendly and sustainable concrete: A review, Construction and Building Materials 272 (2021) 121942. https://doi.org/10.1016/j.conbuildmat.2020.121942.
- [80] I. Amer, M. Kohail, M.S. El-Feky, A. Rashad, M.A. Khalaf, A review on alkali-activated slag concrete, Ain Shams Engineering Journal 12 (2021) 1475–1499. https://doi.org/10.1016/j.asej.2020.12.003.
- [81] J. %J C.I. Davidovits, Ancient and modern concretes: What is the real difference?, 9 (1987) 23–28.

- [82] J. Davidovits, Geopolymers: Inorganic polymeric new materials, Journal of Thermal Analysis and Calorimetry 37 (2005) 1633–1656. https://doi.org/10.1007/bf01912193.
- [83] N.A. Farhan, M.N. Sheikh, M.N.S. Hadi, Investigation of engineering properties of normal and high strength fly ash based geopolymer and alkali-activated slag concrete compared to ordinary Portland cement concrete, Construction and Building Materials 196 (2019) 26–42. https://doi.org/10.1016/j.conbuildmat.2018.11.083.
- [84] C. Shi, Corrosion resistance of alkali-activated slag cement, Advances in Cement Research 15 (2003) 77–81. https://doi.org/10.1680/adcr.2003.15.2.77.
- [85] M.M. Komljenović, Z. Baščarević, N. Marjanović, V. Nikolić, Decalcification resistance of alkali-activated slag, Journal of Hazardous Materials 233–234 (2012) 112–121. https://doi.org/10.1016/j.jhazmat.2012.06.063.
- [86] N.K. Lee, H.K. Lee, Influence of the slag content on the chloride and sulfuric acid resistances of alkali-activated fly ash/slag paste, Cement and Concrete Composites 72 (2016) 168–179. https://doi.org/10.1016/j.cemconcomp.2016.06.004.
- [87] E. Altan, S.T. Erdoğan, Alkali activation of a slag at ambient and elevated temperatures, Cement and Concrete Composites 34 (2012) 131–139. https://doi.org/10.1016/j.cemconcomp.2011.08.003.
- [88] G.A. Khoury, Effect of fire on concrete and concrete structures, Progress in Structural Engineering and Materials 2 (2000) 429–447. https://doi.org/10.1002/pse.51.
- [89] A. Khaled, A. el Mahdi Safhi, A.M. Soliman, Post-fire curing and autogenous self-healing in alkali-activated slag: Microstructures and healing mechanisms, Construction and Building Materials 428 (2024) 136334. https://doi.org/10.1016/j.conbuildmat.2024.136334.
- [90] V.C. Li, E.-H. Yang, Self Healing in Concrete Materials, in: S. van der Zwaag (Ed.), Self Healing Materials: An Alternative Approach to 20 Centuries of Materials Science, Springer Netherlands, Dordrecht, 2007: pp. 161–193. https://doi.org/10.1007/978-1-4020-6250-6\_8.
- [91] H. Huang, G. Ye, C. Qian, E. Schlangen, Self-healing in cementitious materials: Materials, methods and service conditions, Materials & Design 92 (2016) 499–511. https://doi.org/10.1016/j.matdes.2015.12.091.
- [92] L.V. Zhang, A.R. Suleiman, M.M. Allaf, A. Marani, M. Tuyan, M.L. %J C. Nehdi, Building Materials, Crack self-healing in alkali-activated slag composites incorporating immobilized bacteria, 326 (2022) 126842.
- [93] C.-S. Poon, S. Azhar, M. Anson, Y.-L. Wong, Strength and durability recovery of fire-damaged concrete after post-fire-curing, Cement and Concrete Research 31 (2001) 1307–1318. https://doi.org/10.1016/S0008-8846(01)00582-8.
- [94] Y. Yang, M.D. Lepech, E.-H. Yang, V.C. Li, Autogenous healing of engineered cementitious composites under wet–dry cycles, Cement and Concrete Research 39 (2009) 382–390. https://doi.org/10.1016/j.cemconres.2009.01.013.
- [95] H. Liu, H. Huang, X. Wu, H. Peng, Z. Li, J. Hu, Q. Yu, Effects of external multi-ions and wet-dry cycles in a marine environment on autogenous self-healing of cracks in cement paste, Cement and Concrete Research 120 (2019) 198–206. https://doi.org/10.1016/j.cemconres.2019.03.014.
- [96] J.H. Yu, W. Chen, M.X. Yu, Y.E. Hua, The microstructure of self-healed PVA ECC under wet and dry cycles, Mat. Res. 13 (2010) 225–231. https://doi.org/10.1590/S1516-14392010000200017.
- [97] Standard Specification for Slag Cement for Use in Concrete and Mortars, (n.d.).

- https://www.astm.org/c0989 c0989m-18a.html (accessed March 24, 2024).
- [98] Standard Specification for Standard Sand, (n.d.). https://www.astm.org/c0778-21.html (accessed March 24, 2024).
- [99] M. Rajczakowska, L. Nilsson, K. Habermehl-Cwirzen, H. Hedlund, A. %J M. Cwirzen, Does a High Amount of Unhydrated Portland Cement Ensure an Effective Autogenous Self-Healing of Mortar?, 12 (2019) 3298.
- [100] M.T. Marvila, A.R. Garcez de Azevedo, J.A. Tostes Linhares Júnior, C.M. Fontes Vieira, Activated alkali cement based on blast furnace slag: effect of curing type and concentration of Na20, Journal of Materials Research and Technology 23 (2023) 4551–4565. https://doi.org/10.1016/j.jmrt.2023.02.088.
- [101] W. Zhong, W. Yao, Influence of damage degree on self-healing of concrete, Construction and Building Materials 22 (2008) 1137–1142. https://doi.org/10.1016/j.conbuildmat.2007.02.006.
- [102] M.G. Page, H. Cölfen, Improved Control of CaCO3 Precipitation by Direct Carbon Dioxide Diffusion: Application in Mesocrystal Assembly, Crystal Growth & Design 6 (2006) 1915–1920. https://doi.org/10.1021/cg060152r.
- [103] C. Zhang, H. Khorshidi, E. Najafi, M. Ghasemi, Fresh, mechanical and microstructural properties of alkali-activated composites incorporating nanomaterials: A comprehensive review, Journal of Cleaner Production 384 (2023) 135390. https://doi.org/10.1016/j.jclepro.2022.135390.
- [104] B. Pang, H. Zheng, Z. Jin, D. Hou, Y. Zhang, X. Song, Y. Sun, Z. Liu, W. She, L. Yang, M. Li, Inner superhydrophobic materials based on waste fly ash: Microstructural morphology of microetching effects, Composites Part B: Engineering 268 (2024) 111089. https://doi.org/10.1016/j.compositesb.2023.111089.
- [105] G. Moutaoukil, S. Alehyen, I. Sobrados, A.E.M. Safhi, Effects of Elevated Temperature and Activation Solution Content on Microstructural and Mechanical Properties of Fly Ashbased Geopolymer, KSCE J Civ Eng 27 (2023) 2372–2384. https://doi.org/10.1007/s12205-023-1102-0.
- [106] H. El Fadili, M. Ben Ali, A. el M. Safhi, M. El Mahi, A. Aziz, E.M. Lotfi, Effects of encapsulating cellulose acetate microfibers on the mechanical, thermal and environmental properties of geopolymers: A new solution to mitigate the cigarettes pollution, Journal of Building Engineering 72 (2023) 106627. https://doi.org/10.1016/j.jobe.2023.106627.
- [107] D. Kanaan, A.M. Soliman, A.E.M. Safhi, External Sulfate Attack of Ambient-Cured One-Part Alkali-Activated Self-Consolidating Concrete, Sustainability 15 (2023) 4127. https://doi.org/10.3390/su15054127.
- [108] B.C. McLellan, R.P. Williams, J. Lay, A. Van Riessen, G.D. %J J. of cleaner production Corder, Costs and carbon emissions for geopolymer pastes in comparison to ordinary portland cement, 19 (2011) 1080–1090.
- [109] Z. Zhang, J.L. Provis, A. Reid, H. %J C. Wang, Building Materials, Geopolymer foam concrete: An emerging material for sustainable construction, 56 (2014) 113–127.
- [110] J.L. Provis, J.S. Van Deventer, Alkali activated materials: state-of-the-art report, RILEM TC 224-AAM, Springer Science & Business Media, 2013.
- [111] A. Khaled, A. Soliman, Concrete Repair with Alkali Activated Materials: A Review, in: Springer, 2022: pp. 257–264.
- [112] M. Shariati, H. Kamyab, M. Habibi, S. Ahmadi, M. Naghipour, F. Gorjinezhad, S.

- Mohammadirad, A. Aminian, Sulfuric acid resistance of concrete containing coal waste as a partial substitute for fine and coarse aggregates, Fuel 348 (2023) 128311. https://doi.org/10.1016/j.fuel.2023.128311.
- [113] A. Arjomandi, R. Mousavi, M. Tayebi, M. Nematzadeh, A. Gholampour, A. Aminian, O. Gencel, The effect of sulfuric acid attack on mechanical properties of steel fiber-reinforced concrete containing waste nylon aggregates: Experiments and RSM-based optimization, Journal of Building Engineering 64 (2023) 105500. https://doi.org/10.1016/j.jobe.2022.105500.
- [114] B. Bai, J. Chen, F. Bai, Q. Nie, X. Jia, Corrosion effect of acid/alkali on cementitious red mud-fly ash materials containing heavy metal residues, Environmental Technology & Innovation 33 (2024) 103485. https://doi.org/10.1016/j.eti.2023.103485.
- [115] C. Shi, D. Roy, P. Krivenko, Alkali-activated cements and concretes, CRC press, 2003.
- [116] J. Zhang, C. Shi, Z. Zhang, Z. %J C. Ou, Building Materials, Durability of alkali-activated materials in aggressive environments: A review on recent studies, 152 (2017) 598–613.
- [117] A. Soliman, A.E. Abubakr, S. %J J. of M. in C.E. Diab, Effect of Activator Concentrations on the Postfire Impact Behavior of Alkali-Activated Slag Concrete, 35 (2023) 04023166.
- [118] H. Wang, H. Lyu, T. Liu, Y. Li, K.H. %J C. Tan, Building Materials, Effect of post-fire curing on compressive strength of ultra-high performance concrete and mortar, 346 (2022) 128447.
- [119] A.M. Rashad, G.M. %J C. Essa, Concrete Composites, Effect of ceramic waste powder on alkali-activated slag pastes cured in hot weather after exposure to elevated temperature, 111 (2020) 103617.
- [120] R. Cai, H. %J C. Ye, Concrete Research, Clinkerless ultra-high strength concrete based on alkali-activated slag at high temperatures, 145 (2021) 106465.
- [121] P. Minnebo, G. Thierens, G. De Valck, K. Van Tittelboom, N. De Belie, D. Van Hemelrijck, E. %J M. Tsangouri, A novel design of autonomously healed concrete: Towards a vascular healing network, 10 (2017) 49.
- [122] X. Luo, P.T. Mather, Shape Memory Assisted Self-Healing Coating, ACS Macro Lett. 2 (2013) 152–156. https://doi.org/10.1021/mz400017x.
- [123] J.W. Pang, I.P. %J C.S. Bond, Technology, A hollow fibre reinforced polymer composite encompassing self-healing and enhanced damage visibility, 65 (2005) 1791–1799.
- [124] W. Li, Z. Jiang, Z. %J C. Yang, Concrete Composites, Acoustic characterization of damage and healing of microencapsulation-based self-healing cement matrices, 84 (2017) 48–61.
- [125] U.U. Jadhav, M. Lahoti, Z. Chen, J. Qiu, B. Cao, E.-H. Yang, Viability of bacterial spores and crack healing in bacteria-containing geopolymer, Construction and Building Materials 169 (2018) 716–723. https://doi.org/10.1016/j.conbuildmat.2018.03.039.
- [126] Y. Chen, C. Xia, Z. Shepard, N. Smith, N. Rice, A.M. Peterson, A. Sakulich, Self-Healing Coatings for Steel-Reinforced Concrete, ACS Sustainable Chem. Eng. 5 (2017) 3955–3962. https://doi.org/10.1021/acssuschemeng.6b03142.
- [127] L. Ferrara, T. Van Mullem, M.C. Alonso, P. Antonaci, R.P. Borg, E. Cuenca, A. Jefferson, P.-L. Ng, A. Peled, M. Roig-Flores, M. Sanchez, C. Schroefl, P. Serna, D. Snoeck, J.M. Tulliani, N. De Belie, Experimental characterization of the self-healing capacity of cement based materials and its effects on the material performance: A state of the art report by COST Action SARCOS WG2, Construction and Building Materials 167 (2018) 115–142. https://doi.org/10.1016/j.conbuildmat.2018.01.143.

- [128] R. Gagné, M. Argouges, A study of the natural self-healing of mortars using air-flow measurements, Mater Struct 45 (2012) 1625–1638. https://doi.org/10.1617/s11527-012-9861-y.
- [129] C. Edvardsen, Water permeability and autogenous healing of cracks in concrete, in: Innovation in Concrete Structures: Design and Construction, Thomas Telford Publishing, 1999: pp. 473–487. https://doi.org/10.1680/iicsdac.28241.0047.
- [130] K. Van Tittelboom, N. De Belie, Self-Healing in Cementitious Materials—A Review, Materials 6 (2013) 2182–2217. https://doi.org/10.3390/ma6062182.
- [131] L. Li, L. Shi, Q. Wang, Y. Liu, J. Dong, H. Zhang, G. %J C. Zhang, Building Materials, A review on the recovery of fire-damaged concrete with post-fire-curing, 237 (2020) 117564.
- [132] L. Li, P. Jia, J. Dong, L. Shi, G. Zhang, Q. Wang, Effects of cement dosage and cooling regimes on the compressive strength of concrete after post-fire-curing from 800 °C, Construction and Building Materials 142 (2017) 208–220. https://doi.org/10.1016/j.conbuildmat.2017.03.053.
- [133] R. Sarshar, G.A. Khoury, Material and environmental factors influencing the compressive strength of unsealed cement paste and concrete at high temperatures, Magazine of Concrete Research 45 (1993) 51–61. https://doi.org/10.1680/macr.1993.45.162.51.
- [134] Y. Lin, C. Hsiao, H. Yang, Y.-F. Lin, The effect of post-fire-curing on strength-velocity relationship for nondestructive assessment of fire-damaged concrete strength, Fire Safety Journal 46 (2011) 178–185. https://doi.org/10.1016/j.firesaf.2011.01.006.
- [135] Q. Li, G. Yuan, Q. Shu, Effects of heating/cooling on recovery of strength and carbonation resistance of fire-damaged concrete, Magazine of Concrete Research 66 (2014) 925–936. https://doi.org/10.1680/macr.14.00029.
- [136] M. Henry, M. Suzuki, Y. Kato, Behavior of Fire-Damaged Mortar under Variable Recuring Conditions: ACI Materials Journal, ACI Materials Journal 108 (2011) 281–289. https://doi.org/10.14359/51682493.
- [137] D.N. Crook, M.J. Murray, Regain of strength after firing of concrete, Magazine of Concrete Research 22 (1970) 149–154. https://doi.org/10.1680/macr.1970.22.72.149.
- [138] A.H. Akca, N. Özyurt, Deterioration and recovery of FRC after high temperature exposure, Cement and Concrete Composites 93 (2018) 260–273. https://doi.org/10.1016/j.cemconcomp.2018.07.020.
- [139] W. Zhang, Q. Zheng, A. Ashour, B. Han, Self-healing cement concrete composites for resilient infrastructures: A review, Composites Part B: Engineering 189 (2020) 107892. https://doi.org/10.1016/j.compositesb.2020.107892.
- [140] N. De Belie, E. Gruyaert, A. Al-Tabbaa, P. Antonaci, C. Baera, D. Bajare, A. Darquennes, R. Davies, L. Ferrara, T. Jefferson, C. Litina, B. Miljevic, A. Otlewska, J. Ranogajec, M. Roig-Flores, K. Paine, P. Lukowski, P. Serna, J.-M. Tulliani, S. Vucetic, J. Wang, H.M. Jonkers, A Review of Self-Healing Concrete for Damage Management of Structures, Advanced Materials Interfaces 5 (2018) 1800074. https://doi.org/10.1002/admi.201800074.
- [141] A. Talaiekhozani, M.Z.A. Majid, A Review of Self-healing Concrete Research Development, (2014). https://papers.ssrn.com/abstract=3725735 (accessed March 23, 2024).
- [142] Standard Specification for Coarse Aggregate for Bituminous Paving Mixtures, (n.d.). https://www.astm.org/d0692-00r04.html (accessed March 24, 2024).
- [143] Standard Practice for Making and Curing Concrete Test Specimens in the Laboratory, (n.d.). https://www.astm.org/c0192 c0192m-14.html (accessed March 24, 2024).

- [144] A. Abubakr, A. %J M. Soliman, Impact Behaviour of Steel-Fibre-Reinforced Alkali-Activated Slag Concrete Exposed to Elevated Temperatures, 16 (2023) 4096.
- [145] Standard Test Method for Linear Thermal Expansion of Solid Materials by Thermomechanical Analysis, (n.d.). https://www.astm.org/e0831-19.html (accessed March 24, 2024).
- [146] K. Behfarnia, M. Shahbaz, The effect of elevated temperature on the residual tensile strength and physical properties of the alkali-activated slag concrete, Journal of Building Engineering 20 (2018) 442–454. https://doi.org/10.1016/j.jobe.2018.08.015.
- [147] W. Zhong, W. %J C. Yao, building materials, Influence of damage degree on self-healing of concrete, 22 (2008) 1137–1142.
- [148] C. De Nardi, A. Cecchi, L. Ferrara, A. Benedetti, D. %J C.P.B.E. Cristofori, Effect of age and level of damage on the autogenous healing of lime mortars, 124 (2017) 144–157.
- [149] L. Ferrara, V. Krelani, F. Moretti, M.R. Flores, P.S. %J C. Ros, Concrete Composites, Effects of autogenous healing on the recovery of mechanical performance of High Performance Fibre Reinforced Cementitious Composites (HPFRCCs): Part 1, 83 (2017) 76–100.
- [150] C.F. Hollmann, L. Zucchetti, D.C.C.D. Molin, A.B. Masuero, Self-Healing Efficiency of Concretes through Permeability to Chlorides: ACI Materials Journal, ACI Materials Journal 120 (2023) 79–88. https://doi.org/10.14359/51738892.
- [151] V. Wiktor, H.M. Jonkers, Quantification of crack-healing in novel bacteria-based self-healing concrete, Cement and Concrete Composites 33 (2011) 763–770. https://doi.org/10.1016/j.cemconcomp.2011.03.012.
- [152] Standard Test Method for Ultrasonic Pulse Velocity Through Concrete, (n.d.). https://www.astm.org/c0597-22.html (accessed March 24, 2024).
- [153] L. Ferrara, V. Krelani, F. Moretti, Autogenous healing on the recovery of mechanical performance of High Performance Fibre Reinforced Cementitious Composites (HPFRCCs): Part 2 Correlation between healing of mechanical performance and crack sealing, Cement and Concrete Composites 73 (2016) 299–315. https://doi.org/10.1016/j.cemconcomp.2016.08.003.
- [154] Standard Test Method for Measurement of Rate of Absorption of Water by Hydraulic-Cement Concretes, (n.d.). https://www.astm.org/c1585-20.html (accessed March 24, 2024).
- [155] Standard Test Method for Electrical Indication of Concrete's Ability to Resist Chloride Ion Penetration, (n.d.). https://www.astm.org/c1202-22.html (accessed March 24, 2024).
- [156] M. %J C. Chi, Building Materials, Effects of dosage of alkali-activated solution and curing conditions on the properties and durability of alkali-activated slag concrete, 35 (2012) 240–245.
- [157] A. Gruskovnjak, B. Lothenbach, L. Holzer, R. Figi, F. %J A. in cement research Winnefeld, Hydration of alkali-activated slag: comparison with ordinary Portland cement, 18 (2006) 119–128.
- [158] R.R. Lloyd, J.L. Provis, J.S.J. van Deventer, Pore solution composition and alkali diffusion in inorganic polymer cement, Cement and Concrete Research 40 (2010) 1386–1392. https://doi.org/10.1016/j.cemconres.2010.04.008.
- [159] A. Amani, A.M. Ramezanianpour, M. Palassi, Investigation on the sustainable use of electric arc furnace slag aggregates in eco-friendly alkali-activated low fineness slag concrete as a green construction composite, Journal of Cleaner Production 307 (2021) 127257.

- https://doi.org/10.1016/j.jclepro.2021.127257.
- [160] M. Bayati, L.A. %J J. of B.E. Saadabadi, Efficiency of bacteria based self-healing method in alkali-activated slag (AAS) mortars, 42 (2021) 102492.
- [161] D. Darmana, R.L.B. Henket, N.G. Deen, J.A.M. Kuipers, Detailed modelling of hydrodynamics, mass transfer and chemical reactions in a bubble column using a discrete bubble model: Chemisorption of <math><msub is="true"><mrow is="true"><mi is="true">CO</mi></mrow><mrow is="true"><mn is="true">2</mn></mrow></msub></math> into NaOH solution, numerical experimental study, Chemical Engineering Science 62 (2007)2556-2575. https://doi.org/10.1016/j.ces.2007.01.065.
- [162] M. Yoo, S.-J. Han, J.-H. %J J. of environmental management Wee, Carbon dioxide capture capacity of sodium hydroxide aqueous solution, 114 (2013) 512–519.
- [163] M.K. Akhtar, M. Kanwal, R.A. Khushnood, M.B.E. %J J. of B.E. Khan, Assessment of mechanical attributes and microstructural densification of self-healing recycled coarse aggregate concrete using various bacterial immobilizers, 69 (2023) 106229.
- [164] M. Rajczakowska, K. Habermehl-Cwirzen, H. Hedlund, A. Cwirzen, Self-Healing Potential of Geopolymer Concrete, Proceedings 34 (2019) 6. https://doi.org/10.3390/proceedings2019034006.
- [165] B.B. Sabir, S. Wild, M. O'Farrell, A water sorptivity test for martar and concrete, Mat. Struct. 31 (1998) 568–574. https://doi.org/10.1007/BF02481540.
- [166] M.A. Peter, A. Muntean, S.A. Meier, M. Böhm, Competition of several carbonation reactions in concrete: A parametric study, Cement and Concrete Research 38 (2008) 1385–1393. https://doi.org/10.1016/j.cemconres.2008.09.003.
- [167] R. Manjunath, M.C. Narasimhan, K.M. Umesha, Studies on high performance alkali activated slag concrete mixes subjected to aggressive environments and sustained elevated temperatures, Construction and Building Materials 229 (2019) 116887. https://doi.org/10.1016/j.conbuildmat.2019.116887.
- [168] S. Misra, A. Yamamoto, T. Tsutsumi, K. %J S.P. Motohashi, Application of rapid chloride permeability test to quality control of concrete, 145 (1994) 487–502.
- [169] M. Sahmaran, G. Yildirim, T.K. Erdem, Self-healing capability of cementitious composites incorporating different supplementary cementitious materials, Cement and Concrete Composites 35 (2013) 89–101. https://doi.org/10.1016/j.cemconcomp.2012.08.013.
- [170] C. %J C. Shi, concrete research, Effect of mixing proportions of concrete on its electrical conductivity and the rapid chloride permeability test (ASTM C1202 or ASSHTO T277) results, 34 (2004) 537–545.
- [171] R.J. Thomas, E. Ariyachandra, D. Lezama, S. %J C. Peethamparan, Building Materials, Comparison of chloride permeability methods for Alkali-Activated concrete, 165 (2018) 104–111.
- [172] J.J. Jacobs, J.L. Gilbert, R.M. Urban, Current Concepts Review Corrosion of Metal Orthopaedic Implants\*, JBJS 80 (1998) 268. https://journals.lww.com/jbjsjournal/citation/1998/02000/current\_concepts\_review\_\_\_corrosion\_of\_metal.15.aspx (accessed March 24, 2024).
- [173] G.C. Bye, Portland Cement: Composition, Production and Properties, Thomas Telford, 1999.
- [174] W. Wang, T. Noguchi, I. Maruyama, Mechanism understanding of alkali-silica reaction in

- alkali-activated materials system, Cement and Concrete Research 156 (2022) 106768. https://doi.org/10.1016/j.cemconres.2022.106768.
- [175] L.V. Zhang, A.R. Suleiman, M. %J C. Nehdi, Building Materials, Self-healing in fiber-reinforced alkali-activated slag composites incorporating different additives, 262 (2020) 120059.
- [176] B. Park, Y.C. Choi, Self-healing capability of cementitious materials with crystalline admixtures and super absorbent polymers (SAPs), Construction and Building Materials 189 (2018) 1054–1066. https://doi.org/10.1016/j.conbuildmat.2018.09.061.
- [177] C. Zhang, R. Lu, Y. Li, X. Guan, Effect of crystalline admixtures on mechanical, self-healing and transport properties of engineered cementitious composite, Cement and Concrete Composites 124 (2021) 104256. https://doi.org/10.1016/j.cemconcomp.2021.104256.
- [178] K. Sisomphon, O. Copuroglu, E.A.B. Koenders, Self-healing of surface cracks in mortars with expansive additive and crystalline additive, Cement and Concrete Composites 34 (2012) 566–574. https://doi.org/10.1016/j.cemconcomp.2012.01.005.
- [179] M. Roig-Flores, F. Pirritano, P. Serna, L. Ferrara, Effect of crystalline admixtures on the self-healing capability of early-age concrete studied by means of permeability and crack closing tests, Construction and Building Materials 114 (2016) 447–457. https://doi.org/10.1016/j.conbuildmat.2016.03.196.
- [180] B. Park, Y.C. Choi, Quantitative evaluation of crack self-healing in cement-based materials by absorption test, Construction and Building Materials 184 (2018) 1–10. https://doi.org/10.1016/j.conbuildmat.2018.06.206.